DEVELOPMENT OF PT/CNT CATALYST AND TRANSPORT-KINETIC CHARACTERIZATION OF PEMFC CATALYST LAYER

by

Andrea VanBruinessen

A thesis submitted to the Department of Chemical Engineering

In conformity with the requirements for

the degree of Master of Science (Engineering)

Queen's University

Kingston, Ontario, Canada

(January, 2009)

Abstract

The electrochemical performance of a polymer electrolyte membrane fuel cell is known to be dominated by the cathode processes comprising the various reaction and transport steps in the overall oxygen electro-reduction to water occurring in the catalyst layer (CL). This thesis is concerned with one such transport process – oxygen transport in ionomer phase of the CL – and the synthesis/characterization of platinum catalyst on an alternative support – carbon nanotubes (CNT). Specifically, the objectives of the thesis are: (i) exploration of methods for determining the effective permeability of oxygen in the ionomer phase of the carbon-ionomer composite representing the PEMFC catalyst layer (ii) synthesis of Pt/CNT catalysts and characterization thereof.

An electrochemical method for determination of oxygen permeability in Nafion and Nafion-carbon composite films was explored. Since the method is suitable for *dense* films, mathematical model for data analysis had to be modified to allow treatment of porous films. Applying the modified model to the porous Nafion film, the oxygen permeation in the Nafion phase was found to agree with the literature data for oxygen permeation in Nafion membranes. However, no relationship between the effective permeability and ionomer content was found.

Two methods for synthesis of Pt/CNT catalysts were studied – the precipitation method and the colloidal/ethylene glycol method. Functionalization of CNTs was found to be critical to obtaining any significant amount of Pt deposition on CNT. The precipitation method did not yield reproducible results. Pt/CNT catalysts of desired properties were synthesized via the colloidal/EG method. It was found that a high pH of 8.5 to 10.5 resulted in smallest Pt particle size. The Pt particles size was determined to range 2-4 nm. The synthesized Pt/CNT catalysts were also tested in a fuel cell environment. Steady-state polarization curves in humidified H_2/Air system were obtained that demonstrated performance comparable to commercial electrodes in that cell

potential of greater than 0.6 V at current density of 800 mA/cm^2 electrode area and a limiting current density of 1200 mA/cm^2 electrode area were observed.

Acknowledgements

I would like to thank Dr. Kunal Karan for granting me the opportunity to work on such an interesting and challenging project and for his excellent supervision and guidance. I am grateful to have had an opportunity to gain from his large span of knowledge.

I would also like to thank Dr. Dzmitry Malevich and Dr. Madhu Saha for their help in experimental procedures and for the informative lessons which they have shared with me. I would like to thank my office mates at both FCRC and Dupuis for making my work experience more enjoyable and for their support in both academic and non-academic matters.

I would like to thank NSERC for their financial support which makes it possible to carry-out many exciting and stimulating projects.

Finally, I would like to thank my family and friends without whose support this research would have been possible.

Symbols

Symbol	Description	Units
PEMFC	Polymer Electrolyte Membrane Fuel Cell	-
GDL	Gas Diffusion Layer	-
CL	Catalyst Layer	-
CNT	Carbon Nanotubes	-
MWCNT	Muti-walled Carbon Nanotubes	-
RDE	Rotating Disk Electrode	-
EG	Ethylene Glycol	-
XRD	X-Ray Diffraction	-
SEM	Scanning Electron Microscopy	-
TEM	Tunneling Electron Microscopy	-
XPS	X-Ray Photoelectron Spectroscopy	-
v_r, v_y, v_ϕ	Velocity component in the r, y and ϕ directions respectively	m/s
ω	Angular velocity of RDE	RPM^{-1}
U_o	Limiting velocity of species o	m/s
C_o	Concentration of species o in the bulk solution	mol/m^3
C_o^*	Concentration of species o in the film	mol/m^3
ν	Viscosity of species o	m^2/s
ρ	Density	kg/m^3
P	Pressure	Pa
D_o	Diffusion coefficient of species o in bulk solution	m^2/s
D_s	Diffusion coefficient of species o in the film	m^2/s
D_n	Diffusion coefficient of species o in Nafion®	m^2/s
D_p	Diffusion coefficient of species o in pores	m^2/s

n	Number of electrons taking place in reaction	mol of e^-/mol oxygen
δ	Film thickness	m
A	Electrode area	m^2
A_p	Area of pores coating electrode	m^2
A_n	Area of Nafion® coating electrode	m^2
F	Faradays constant	As/mol of e^-
i	Total current	A
i_{lc}	Limiting current	A
i_l	Current associated with Levich flux	A
i_s	Current associated with reactant diffusion through film	A
κ	Partition coefficient	$(mol/m^3)_{film}/(mol/m^3)_{bulk}$
ε_n	Volume fraction Nafion®	m^3 Nafion®/m^3
ε_p	Porosity (volume fraction pores)	m^3 pores/m^3
ε_c	Volume fraction carbon	m^3 carbon/m^3
V_f	Total film volume	m^3
$V_{solution}$	Volume of solution deposited on electrode	m^3
V_{pores}	Volume of pores in film	m^3
V_{carbon}	Volume of carbon in solution	m^3
V_{nafion}	Volume of Nafion® in solution	m^3
R	Volume ratio of carbon to nafion	m^3 carbon/m^3 Nafion®

Table of Contents

List of Figures

List of Tables

Chapter 1

Introduction

1.1 General Introduction

Globally, the demand for energy is expected to continually increase as the standard of living in developing countries embraces those in the developed nations. Now, a significant proportion of the global energy needs are for the transportation sector. The number of vehicles in developing countries such as India and China are projected to grow to 31% of the total global light-vehicle market by 2014 [1]. The energy requirement for vehicles is almost entirely fulfilled by petroleum derived fuels such that the hydrocarbon fuel is combusted in an internal combustion engine (ICE) to convert chemical energy into mechanical work. Whereas the ICE technology is robust, its fuel-to-work conversion efficiency is low. More importantly, there is a two level impact of tailpipe emissions from an ICE. On a local level, the unburnt hydrocarbons, soot and nitrous oxides result in urban pollution. On a global level, the carbon emissions contribute to the global warming effect.

Thus, the world today is faced with the challenge of a significant increase in energy demand for vehicle transportation and, concurrently, an increasing pressure to minimize pollution/carbon emissions. As such, the automotive companies worldwide have active research and development programs for electrical power based vehicles, which certainly minimizes if not eliminates the urban pollution problem. The hybrid electric vehicles are already available [2] while a number of companies have demonstrated *concept* cars that are driven by hydrogen-fueled fuel cells. Although the problem of finding a carbon-free source of hydrogen is an important technological challenge, the H_2-fueled fuel cells convert chemical energy more efficiently into electrical energy with the only *local* by-products being heat and water. Thus, fuel cells can address the problem of

local pollution and, if the hydrogen can be derived from renewable sources and/or via processes wherein carbon is sequestered, the global warming effect can also be reduced.

Now, there are a number of different types of fuel cells varying in the range of power output, operating temperature, type of fuel utilized, and the characteristics of the system response dynamics. The polymer electrolyte membrane fuel cells (PEMFCs) fueled by hydrogen are considered to be most suitable for automotive applications owing to their fast dynamics and high power densities. PEMFCs have also been successfully employed in space vehicles (shuttles) over the past three decades [3]. Although the technological viability of fuel cells has been demonstrated, its adoption for terrestrial automotive applications demands that its cost must be significantly reduced while concurrently increasing its lifetime without compromising the electrochemical performance.

To develop strategies for cost reduction, it is important to understand the key contributors to the cost of a PEMFC stack. Further, it is important to understand that any new design or material changes to be implemented does not adversely affect the electrochemical performance. The latter is a net effect of several coupled reaction-transport processes. To provide appropriate context of the research undertaken in this thesis, in the following sections, a general introduction to fuel cells is given followed by description of PEMFC operation, its key components and factors affecting its electrochemical performance. Next, the importance of the catalyst layer with respect to its contribution to high cost and its role in overall cell performance is presented.

1.2 Fuel Cells

Fuel cells are electrochemical devices that convert chemical energy directly into electrical energy.

The overall reaction of a fuel and an oxidant in a fuel cell is effected indirectly via two half-cell electrochemical reactions that occur at the two electrodes separated by an electrolyte which is able to carry an ion between the electrodes while the electrons are conducted through an external circuit. There are a number of different types of fuel cells and one classification is based on the type of the electrolyte employed as presented below:

- Polymer Electrolyte Membrane Fuel Cells (PEMFCs)
- Direct Methanol Fuel Cells (DMFCs)
- Alkaline Fuel Cells (AFCs)
- Molten Carbonate Fuel Cells (MCFCs)
- Phosphoric Acid Fuel Cells (PAFCs)
- Solid Oxide Fuel Cells (SOFCs)

1.2.1 PEMFC Operation, Components and Performance

Basic Operation

The basic operation of a PEMFC is shown schematically in Figure 1. Hydrogen is split at the anode into protons and electrons as per the following half-cell reaction:

$$2H_{2(g)} \leftrightarrow 4H^{+}_{aq} + 4e^{-}_{pt} \quad \textbf{(1-1)}$$

The protons pass through the electrolyte to the cathode while the electrons are forced through an external circuit where they can do useful work. At the cathode, the electrons and protons recombine with the oxygen according to the following reaction:

$$O_{2(g)} + 4H^{+}_{aq} + 4e^{-}_{pt} \leftrightarrow 2H_2O_{aq} \quad \textbf{(1-2)}$$

Thus, the following overall reaction occurs in the PEMFC

$$2H_{2(g)} + O_{2(g)} \leftrightarrow 2H_2O_{(aq)} \quad \textbf{(1-3)}$$

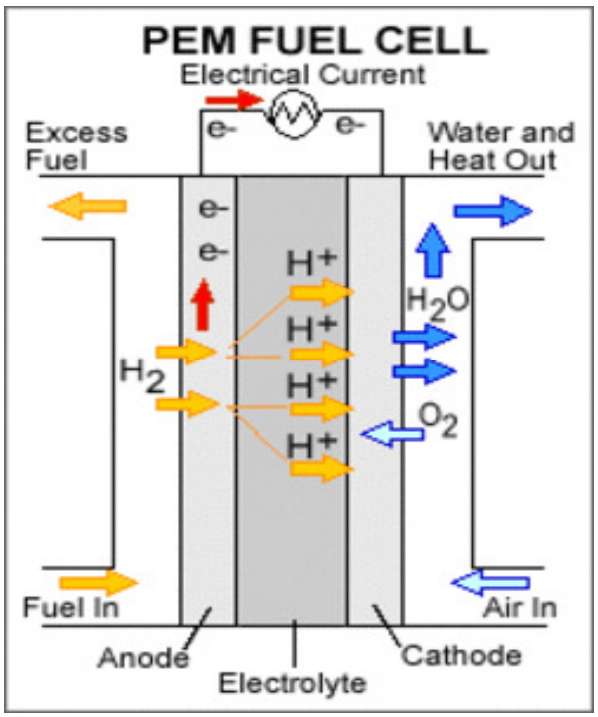

Figure 1: Simplified representation of PEMFC operation [5]

PEMFCs are aimed for operation in the range of 25 to 80 ^{0}C [4] and accordingly they are classified as a low temperature fuel cell.

Components of a practical PEMFC

The key components of a fuel cell are obviously a cathode, an anode and an electrolyte. In addition to these components, a practical fuel cell requires several other sub-components as shown in Figure 2. A description of the key components of a PEMFC and their functionality is discussed here. The most commonly employed electrolyte for PEMFCs is a DuPont product - Nafion®, which is a semi-permeable perfluorosulfonic ionomer (PFSI). The mechanism of proton transport in Nafion® is still a topic of debate but it is well established that sufficient level of hydration is essential for proton transport. The electrochemical reactions in the anode and the cathode are effected on the electro-catalyst platinum which is supported on carbon. The anode and

cathode layers are also porous to allow for reactant transport as well contain certain amount of ionomer to allow for the transport of proton generated/consumed in the electrochemical reactions. The electrons generated/consumed in the anode/cathode catalyst layer are conducted through the adjacent porous transport layer or PTL (usually referred to as gas diffusion layer or GDL) which is typically a porous carbon paper or fabric. The combined unit of PTL, catalyst layers, and the membrane is commonly referred to as the membrane electrode assembly. The PTL is placed between the catalyst layer and the bipolar plate and this porous material also helps to distribute the reactant gases from the flow-channel to the catalyst layer. The bipolar plate, in addition, to conducting electrons to the adjacent cell also convectively transports the reactants hydrogen and oxygen. For this purpose, the bipolar plates have flow-channels machined in them.

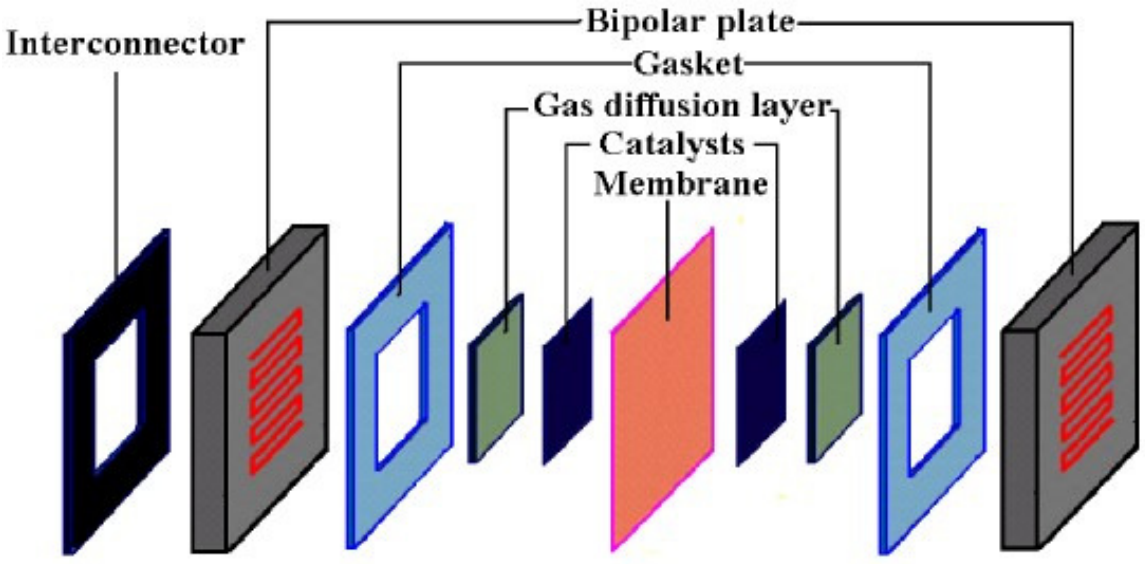

Figure 2 : Schematic Representation of a Single PEMFC Structure [5]

The typical dimensions of the cell components vary from the 10-30 micron thin catalyst layers to 1 mm (1000 micron) thick bipolar plates. The polymer electrolyte membrane and the GDLs have thicknesses ranging 50-100 microns and 200-300 microns, respectively. The channel lengths can

be in meters. Thus, the various physico-electro-chemical processes occur over different length scales. Moreover, the reaction-transport processes in a PEMFC are highly coupled and the sub-component design as well as the constituent material properties influences the overall PEMFC performance.

PEMFC Electrochemical Performance

The electrochemical performance of fuel cells is typically characterized in terms of the voltage-current relationship, also known as the polarization curve. An example of this plot of cell voltage vs. current density can be found below in Figure 3. It is important to emphasize that the polarization curve of a fuel cell is a *net* or *global* effect of numerous transport (electron and ion conduction, chemical species diffusion/convection, mass convection) and electrochemical reaction (oxygen reduction reaction and hydrogen evolution reaction). It is not possible to extract an in-depth understanding of the fuel cell performance from the polarization curve. However, it allows for the first level of assessment of fuel cell performance and, is especially a useful tool for comparison of performance of two different cells.

The polarization curve has several distinct regions which relate to the dominance of three different key effects present in the fuel cell. In an ideal or reversible fuel cell the potential is independent of the current drawn. However, this is not the case in practice due to irreversibilities present in the cell. The difference between the actual voltage and the reversible voltage is called the overpotential and can be the result of several resistances described below [6]:

- *Activation losses*: These losses are related to the electrochemical kinetics of the half-cell reactions and their effects are more dominant at lower current densities. The origin of the losses is in the requirement to alter the electrical potential different at the electrode-electrolyte

interface from its equilibrium level to drive the electrochemical reactions. In polymer electrolyte membrane fuel cells (PEMFCs) the activation losses are typically due to *slow oxygen reduction reaction* (ORR) kinetics at the cathode.

- *Ohmic losses*: The ohmic losses arise due to the resistances of electron transport in the electrodes (gas diffusion layer and the catalyst layer) and the bipolar plates as well as the transport of ions in the electrolyte. The ohmic losses (potential difference) have linear relationship to the current density. These losses increase steadily with an increase in current density. Thus, as a result of the linear profile of the polarization curve in the intermediate current densities, it is commonly stated that ohmic losses dominate in this current density range.

- *Mass Transport losses:* The mass transport losses arise from the fact that the reactant cannot be supplied to the catalytic sites at sufficient rate resulting in reactant concentration at catalyst sites being significantly lower than the bulk or supplied reactant concentration. The low concentration translates into the requirement of higher activation overpotential to compensate for the lowering of reaction rate due to reduced concentration.

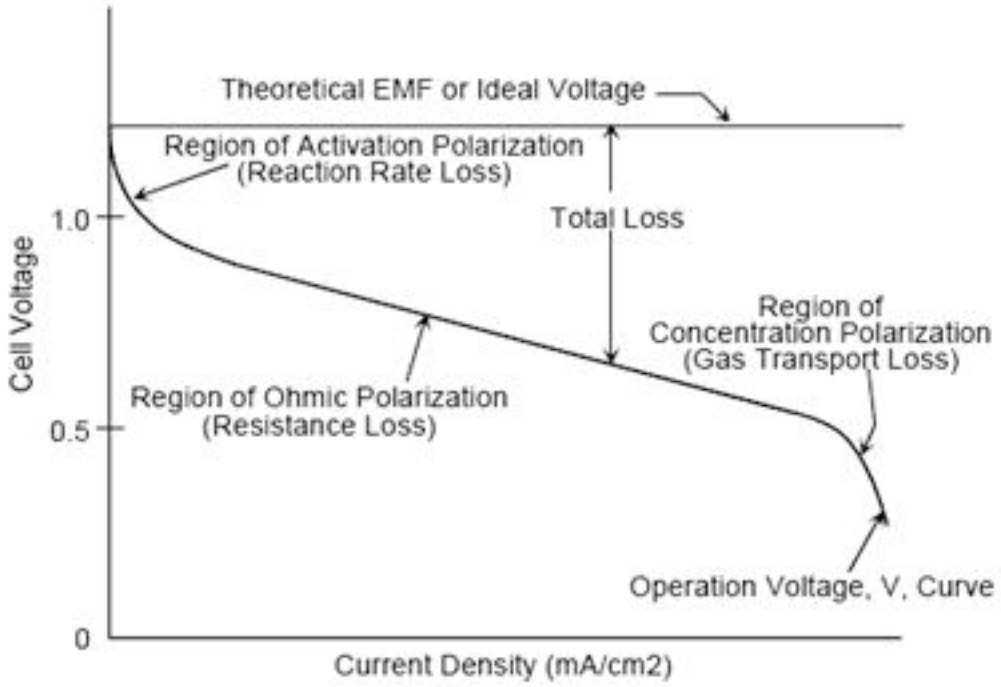

Figure 3: Typical PEMFC Polarization Curve [5]

The various losses are obviously affected by the operating conditions (temperature, composition, relative humidity, and pressure). In addition, the PEMFC sub-component material properties, which are a function of the composition and microstructure, influence the various physico-electro-chemical processes and ultimately the electrochemical performance of the cell. A fundamental understanding of the interplay between the aforementioned factors is a key to meeting the PEMFC technology research and development targets discussed below.

1.3 PEMFC Technology: R&D Targets and Challenges

The main focus for PEMFC research and development is to produce a commercially viable product. In order to reach this goal, several cost and durability requirements have been set. In a recent publication [7] Ballard Power has outlined some of the key challenges required to meet the

increased durability of 5000h stack life and the required steps to lower the cost of PEMFCs. Understanding of what factors affect performance losses and material degradation is essential in finding adequate solutions. It is suggested that advanced tools for performance diagnostics, ex situ structural characterization and accelerated durability testing are key areas of improvement for providing a strategy to improve fuel cell performance and durability. Reducing performance losses and degradation directly translate into cost reduction as well because price per kW and over the lifetime also decreases.

Cost Target/Breakdown

For automotive applications, since the PEMFC technology is considered as the replacement for the ICE technology, the cost target has been set to be $30/kW [7,8]. The cost targets, created by the U.S program for the development of fuel cells [8], for 2010 and 2015 are $45 for 30 kW and 80 kW, respectively for the net system. The actual 'commercial' cost of a PEMFC stack is difficult to calculate because appropriate consideration of the volume production must be taken. Nonetheless, a study by Isa-bar on (2001) reports the breakdown of cost of each component. The cost of the membrane electrode assembly (MEA) is estimated to be more than 50% of the total PEMFC component costs. The polymer electrolyte membrane and precious metal cost contributes to more than 80% of the MEA cost. The study by GM group also indicates that the cost of PEM and platinum add up to greater than 70% of the total PEMFC cost.

Clearly, two of the PEMFC components that contribute significantly to the cost of PEMFCs and ability to meet 2010 cost targets are the membrane and the precious metal catalysts [8]. In order to meet the cost objectives, several alternatives to the current membrane material - Nafion® - are being investigated. In general research is focused on organic membranes and composite membranes. The goal is to create a membrane capable of withstanding higher temperatures,

allowing for better PEMFC performance, and one which is capable of operating without humidification [9,10 and references within]. Current membranes must be hydrated in order to conduct their ion transport role which requires a humidification system that can be costly. Creating a self-hydrating membrane would significantly reduce the cost of the fuel cell.

Catalyst Cost Reduction Target

The challenge for precious metal cost reduction is elucidated via a simple analysis below. Let us accept the PEMFC cost target of $30/kW target. Now, let us restrict the platinum cost to be 10% of the total cost, i.e. $3/kW. Now, the peak power for the state-of-the-art PEMFC stack can be set as 0.9 W per cm^2 of electrode, as per the report from the GM group. Also, the current cost of Platinum is $1100/gm. Thus, to meet the $3/kW target for a PEMFC stack, the platinum loading (in mg per cm^2 electrode) can be calculated to be 0.06 mg/cm^2. In contrast, the platinum loading in the current PEMFC catalyst layers are in the order of 0.4 mg/cm2 and 0.2 mg/cm^2, i.e. a total of $0.6/cm^2$. Thus, the platinum loading must be reduced nearly 90% of the current level to meet the cost target. The reduction of platinum loading while maintaining high enough electrochemical performance is not a trivial task since the activation losses increase significantly with a decrease in catalyst loading. Nonetheless, recent computational analysis using effectiveness factor approach by Sun et al [11] indicates that a significant amount of catalyst in the PEMFC catalyst layers are poorly utilized because of significant mass transport limitations. It has also been shown [11] that by micro- and nano-scale engineering of the CLs, the Pt loading can be reduced significantly while still maintaining high electrochemical performance. For rational design/engineering of CLs, it is however important to understand the various physical/chemical processes occurring in the CL and how the microstructure influences the overall electrode performance.

1.4 PEMFC Catalyst Layer (CL)

This thesis is concerned primarily with the studies of the PEMFC cathode catalyst layer and, as such, a description of the CL structure and various physical/chemical occurring therein is presented in the following sections.

1.4.1 PEMFC CL: Composition and Structure

CL Constituents and Composition

The PEMFC catalyst layer (CL) is a porous composite of complex microstructure that is made of the building blocks - Platinum (Pt), Carbon, and ionomer. The catalyst layer also contains open pores. The platinum catalyst is dispersed on an electron-conducting support material, typically carbon black [6]. The platinum particles range 2-5 nm and the most commonly employed carbon support, Vulcan XC-72, is 20-30 nm diameter in size. Supported catalysts have resulted in a 10-100 fold increase in Pt surface area compared to the unsupported Platinum used in the early PEMFC systems [12]. The ionomer in the catalyst layer serves both as a binder and the pathway for the protons generated/consumed in the electrochemical reactions. A typical ionomer loading for the catalyst layer has been reported to be 2 mg/cm^2 [13]. However, the commercial electrode suppliers do not disclose the ionomer loadings or Pt to carbon ratio. As stated earlier, typical thickness of catalyst layers range from 10-30 microns and are a function of the material composition/loading (i.e. catalyst ink formulation) as well as the fabrication process. The Pt to Carbon ratio in commercial catalysts and the typical ionomer loadings strongly affect the performance of fuel cells. The fabrication method of high performance catalyst layer is a proprietary knowledge and usually considered to be an art with foundation in the science of ink formulation. The ultimate structure and, consequently, the performance of catalyst layer is a function of the fabrication process. Approach to optimized structure/composition of CL has been primarily empirical [13] although theoretical optimization studies are emerging [14]. Theoretical

work considers idealized microstructure and the true microstructure of the CL is still a matter of debate.

CL Microstructure

Among the most detailed description of the catalyst layer, insofar as the mathematical modeling effort has been concerned is the agglomerate structure. In fact, it is the mathematical modeling of PEMFC with a focus on the catalyst layer that has driven the efforts, in the past few years, to unravel the CL microstructure. The agglomerate description considers the CL to be composed of spherical/cylindrical agglomerates of Pt/C catalyst particles with porous inter-agglomerate space[11]. The intra-agglomerate space is either considered to be filled with polymer electrolyte ionomer [11,15] or with water [16] as seen below in Figure 4. The agglomerate is considered to be covered with a film of ionomer. The CL is then a porous structure made of random aggregates of the agglomerates. For electrochemical reaction to take place, percolating networks for transport of electrons, protons and chemical reactants (oxygen and hydrogen) must exist. Thus, the electrochemical reaction takes place at the platinum catalyst that is covered by ion-conducting media capable solvating the reactants. However, the participating reactants and products (electron, ion and O2/H2 and H2O) of the electrochemical reaction must be transported in as facile a manner to the reaction sites. Thus, the electrochemical reactions occurring at atomistic and nano-scale in the CL are coupled to the micro-scale transport of charged and chemical species.

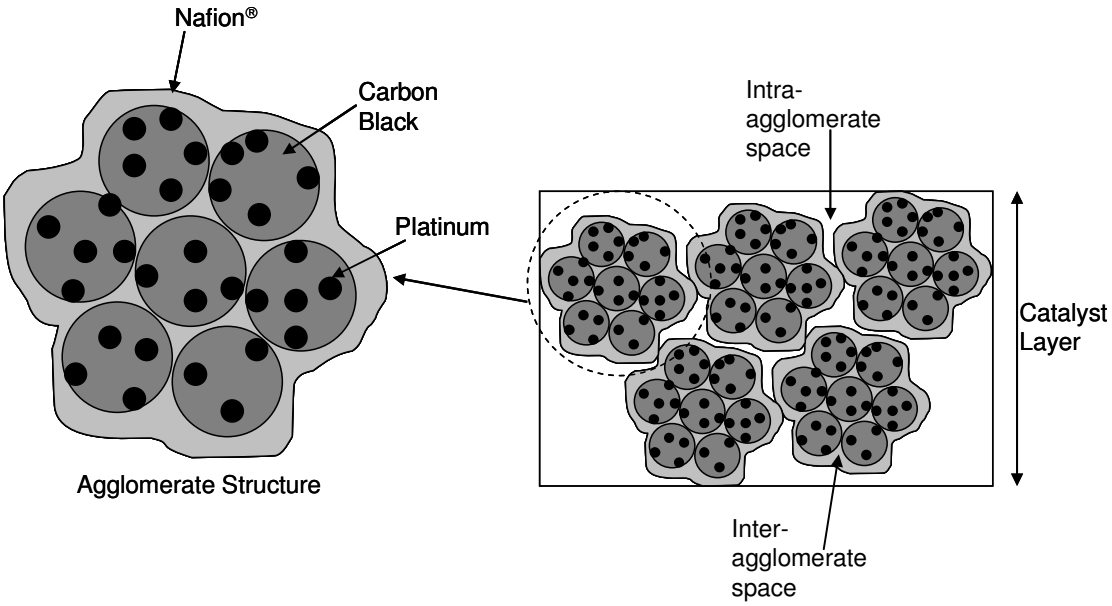

Figure 4: Catalyst Layer Agglomerate Structure

1.4.2 Coupled Reaction-Transport Processes in PEMFC Cathode CL

In this section, a brief description of the reaction-transport processes in the PEMFC cathode catalyst layer is presented considering the agglomerate-type microstructure. The cathode CL is selected since the Oxygen Reduction Reaction (ORR) at the cathode occurs much slower than the hydrogen oxidation reaction at the anode and, as such, is responsible for the dominant activation loss for a PEMFC. In fact, a significant proportion of the overall electrochemical performance loss of a PEMFC can be due to the cathode processes. Thus, the ORR and the cathode structure provide a great deal of concern for developers trying to lower platinum loadings.

Referring to Figure 4 above, the key processes occurring within the cathode catalyst layer can be broken down to the following steps:

1. Diffusion of chemical species in the catalyst layer: In this step the gaseous oxygen diffuses through air filled pores in the catalyst structure

2. Oxygen dissolution at the gas-electrolyte film interface: The oxygen dissolves into the ionomer phase and becomes part of the ionomer phase

3. Diffusion of dissolved oxygen in the electrolyte film which surrounds the agglomerates

4. Oxygen reduction reaction on the catalyst surface: Oxygen that reaches active catalyst site reacts with H^+ ions and electrons to create water.

Each of these steps plays a significant role in the overall reaction at the cathode. It is important to recognize that any one of these steps may act as the limiting process and it is thus important to examine the catalyst layer micro-structure in detail since it will affect each step.

Importance of CL design

In general, the electrochemical performance of a fuel cell is strongly influenced by physical/chemical processes that occur in its catalyst layer. The electrochemical kinetics is a function of the catalyst employed and the reaction conditions. The net reaction rate depends on how the three distinct species – electrons, ions and chemical - participating in an electrochemical reaction are transported to the active reaction sites. In order to be used effectively the platinum must have access to the gas, the electron conducting material (carbon supports) and the proton conducting phase (ionomer phase) [11]. The type and arrangement of carbon supports are thus essential in determining the effectiveness of the platinum. The key microstructural features that affect the electrochemical reactions are the extent of catalyst agglomeration, ionomer coverage of the catalyst and availability of pathways for transport of each species. The effectiveness of the catalyst is strongly affected by two main factors. First, it is affected by the ability of the oxygen to diffuse through the ionomer covering the catalyst and secondly by the extent to which the

ionomer and catalyst support phases form connected pathways for proton and electron transport respectively. For the latter, some of the catalyst particles may be inactive due to a lack of ionomer coverage, leaving no networks for ion (proton) transport. Current studies show that a significant amount of the platinum present on the carbon supports is not effectively utilized at high current density conditions as quantified by low effectiveness factor [11]. That is, due to its low diffusivity, most of the oxygen diffusing through the ionomer phase is used in the outer part of the catalyst agglomerate leaving the platinum particles in the core of the agglomerate unused.

Dissolved oxygen diffusion through the ionomer phase of the solid matrix of the catalyst layer is an important transport step in the overall reduction of oxygen at the cathode. By designing the catalyst layer microstructure such that oxygen transport path is reduced, catalysts can be effectively utilized. Such a design is shown as an alternative catalyst layer structure in Figure 5 below. The performance of such a structure has been assessed through computational modeling [11].

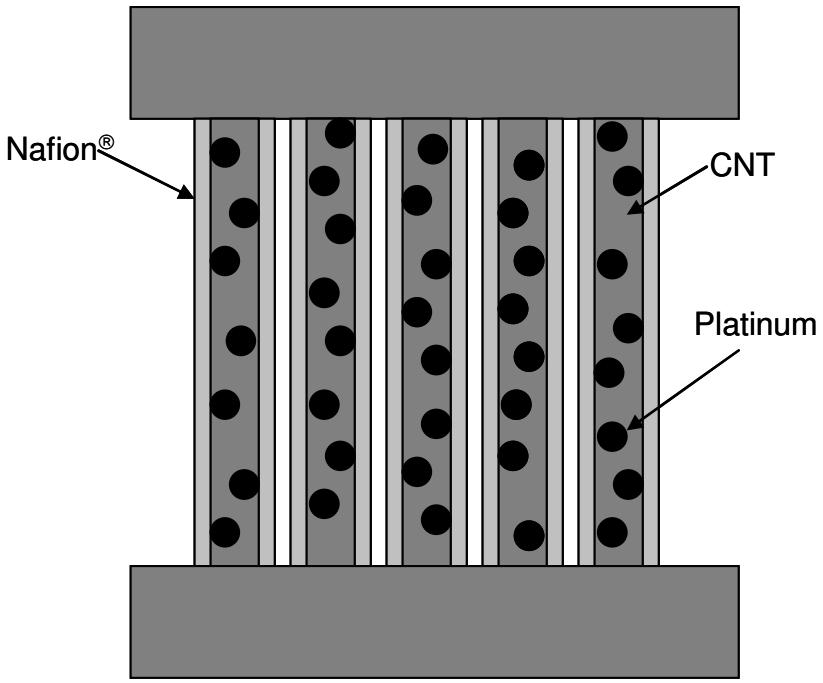

Figure 5: Suggested Cathode Catalyst Structure

This alternative microstructure consists of aligned high-aspect ratio carbon support with well dispersed platinum on its outer surface and covered by a thin layer of ionomer, e.g. Nafion. In this aligned structure carbon nanotube (CNT) a catalyst support can be used in contrast to carbon black (CB) used in conventional electrodes. In this aligned structure (Figure 5) the oxygen diffusion length in the ionomer phase prior to reaching the active platinum sites is short in comparison to agglomerate structure shown in Figure 4. This results in less resistance to diffusion and potentially a more utilized catalyst. Furthermore, some studies indicate that the CNT support would also help to reduce the rate of degradation since CNTs are more stable than CB [17].

1.5 Summary

Qualitative and quantitative analyses discussed above indicate that by micro- and nano-scale engineering of fuel cell electrodes, the amount of Platinum used and, thereby, the overall cost can be reduced compared to that for the state-of-the-art fuel cell electrodes. However, the limitation of

these quantitative analyses is that they are based on mathematical models with *idealized* representation of the catalyst layer microstructure. Further, several of the transport properties - the effective ionic conductivity, effective electronic conductivity and effective diffusivity – employed as input parameters in these mathematical models have not been experimentally measured. Even if these properties are known with acceptable level of accuracy, the fabrication CL with controlled microstructure as shown in Figure 5 provides its own challenges. For instance, with the building block of such CL architecture - Pt loaded on CNTs - is not available commercially. Thus, development of such new CL architecture requires that the methods for fabrication of Pt/CNT catalyst must be first investigated.

1.6 Thesis Objective

This thesis is concerned with PEMFC catalyst layer studies. Specifically, the two distinct but related objectives of the thesis are:

(i) Exploration of methods for determining the effective transport properties for oxygen in the ionomer phase of the carbon-ionomer composite representing the PEMFC catalyst layer

(ii) Synethesis of platinum CNT based catalysts –investigating the effect of the catalyst fabrication method and examining the physical, chemical and electrochemical characteristics of the catalyst

1.6.1 Thesis Outline

In this thesis, Chapter 2 contains summary of the prior research pertinent to the research objective outlined above. Chapter 3 contains description of experimental methods and relevant theoretical background for analysis of experimental data. Chapter 4 discusses the results pertaining to the determination of the effective oxygen permeability in Nafion®-carbon composite films. Chapter 5 presents catalyst properties obtained by the various preparation methods and the effect of several

key parameters in obtaining optimal catalyst performance. Finally Chapter 6 contains conclusions and recommendations.

Chapter 2
Literature Review

This chapter presents a review of literature on the topics most pertinent to the thesis work. These include catalyst layer structure and fabrication methods, deposition of platinum on carbon nanotubes, and studies on the determination of oxygen permeability in Nafion® films/membranes.

2.1 Preface to PEMFC Literature

PEMFC technology research and development began in 1960 and as such there is an immense collection of literature concerned with the science and engineering of PEMFCs. Significant progress on specific topics has been documented continually over the years and are available as Handbook [18] and research articles. Recent review articles summarize the current knowledge on the general topic of PEMFC Technology Status [19] and specific topics including development of non-Pt [20] and Ru-based [21] catalysts for oxygen reduction reaction, solid polymer electrolytes [10], methods for preparation of electrodes [13] or membrane electrode assemblies [22], bipolar plates [23,24,25], impact of contaminants [26], impact of water management [27], and computational models for PEMFCs [28,29]. Further, relevant to the thesis work, a review of methods for synthesis of Pt-carbon nanotube has been recently published [30], however, no review articles/papers on determination of effective transport properties of catalyst layers and structure of catalyst layer has yet been published.

2.2 PEMFC Catalyst Layer: Structure, Synthesis and Characterization Methods

The PEMFC catalyst layer is the heart of the fuel cell where the electrochemical reactions take place, generating electrons on one electrode (anode) while consuming electrons on the other

electrode (cathode). Useful work is done when the electrons generated on the anode flow through an external circuit (where work is done) and are eventually consumed at the cathode. As discussed in section 1.4, the design of catalyst layer must take into consideration both the electrochemical kinetics and the reactant (electrons, protons and hydrogen or oxygen) transport effects. Whereas the intrinsic kinetics of the half-cell electrochemical reactions will depend on the catalyst-electrolyte and reaction conditions, the microstructure of the CL will influence the effective transport properties. Since one aspect of the thesis is concerned with exploration of the method for determination of effective oxygen diffusivity (permeability) in the ionomer phase of the CL, it is deemed relevant to discuss the current understanding of CL microstructure, which is presented in section 2.2.1. Further, since a major focus of the thesis is the development and characterization of platinum supported on carbon nanotubes, sections 2.2.2 and 2.2.3 discuss the relevant literature on these topics.

2.2.1 Current Understanding of PEMFC Catalyst Layer Structure

The PEMFC catalyst layer is a complex porous composite of Pt/C catalyst and polymer electrolyte. The Pt/C composition is known and reported as the mass percent of Pt on carbon support. The nominal composition of Pt/C and polymer electrolyte for a catalyst layer is usually known by the manufacturers because the overall composition of the catalyst ink is specified. However, the actual state of aggregation of carbon or the shape and distribution of polymer electrolyte in the CL is not known. Thus, the structure of the building blocks of the catalyst layer in the ink stage of the CL fabrication is not known. The state of these building blocks in the catalyst ink is expected to dictate the final microstructure of the CL that may evolve. Now, idealized structures of PEMFC CL have been discussed in the literature and assume spherical agglomerates as shown in Figure 4. There are two variations of these structures. One structure considers the agglomerate to be filled with water and held together by a thin film of polymer electrolyte. The other structure considers the agglomerate to be filled with polymer electrolyte as

shown in Figure 4. It was hypothesized by Uchida et al [31] that either of the two structures could arise depending on the state of ionomer in the catalyst ink formulation. The state of the ionomer (polymer electrolyte) depends on the dielectric constant of the suspension media. Electron microscopy has been applied to examine the structure of the CL and despite the poor quality of the image, the agglomerate structure of the catalyst layer has been argued to exist. Examples of electron micrographs used for making such arguments are shown in Figure 6 below. Clearly, the spherical agglomerate like structure idealized in Figure 4 is very hard to deduce from the micrographs of Figure 6 below.

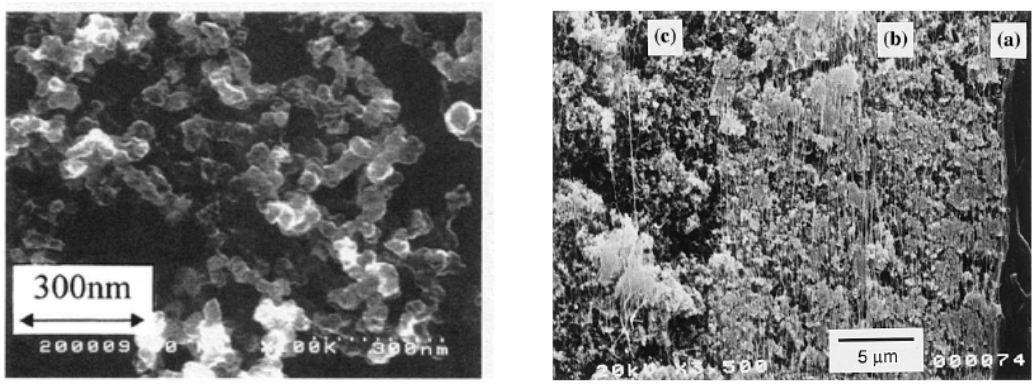

(a) (b)

Figure 6: Scanning Electron Microgrpahs of Catalyst Layers: (a) Uchida *et al* [31] and (b) Broka and Ekdunge[15]

More recently, through careful optimization of sample preparation steps, high quality images of a CL has been generated by Oak Ridge National Laboratory, USA. An example of TEM image of the PEMFC catalyst structure is shown in

Figure 7 [32]. It shows the presence of the three distinct building blocks of the catalyst layer - platinum, carbon, and the ionomer. The image appears to support the thin-film covered

agglomerate structure of the catalyst shown in Figure 4. However, these images must be interpreted with care. For instance, the TEM image is a two-dimensional image of a three-dimensional structure. Moreover, that this single image may be representative of all locations in the catalyst layer is not necessarily true. Furthermore, the structure will depend on the fabrication method/conditions. An excellent review of PEMFC electrode or catalyst layer fabrication methods has been presented by Litster et al [13].

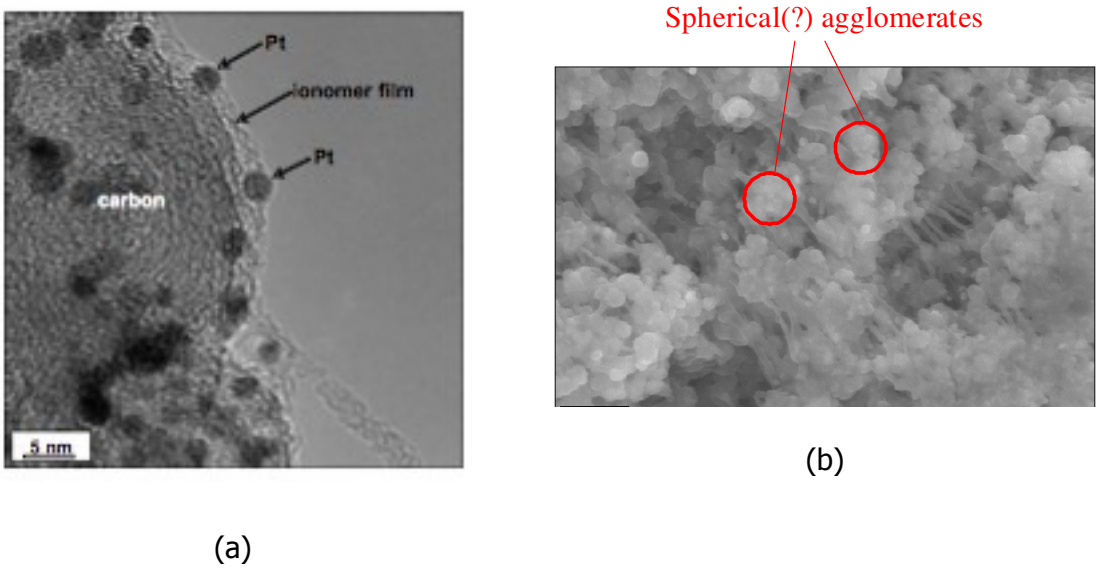

Figure 7: Electron Microscopy Images of PEMFC Catalyst Layer – (a) TEM image and (b) SEM Image [32]

2.2.2 Synthesis of Pt/CNT Catalysts

The discussions in the preceding section were essentially limited to catalyst layer structure made of platinum supported on carbon black [13,33]. Little information exists on the microstructure of electrodes made of platinum supported on alternative support such as carbon nanotube (CNT). This is not surprising, since it is only in the last 10 years that Pt/CNT have begin to be considered for application in fuel cells as discussed in a recent review on the progress in the synthesis of

carbon-nanotube supported Pt catalyst for PEM Fuel cell catalysis carried out by Lee et al [30]. It is worthwhile to mention that such catalysts are not commercially available. It is also useful to recall that one of the objectives of the thesis is the development and characterization of Pt/CNT catalysts, which ultimately is to be utilized in the creation of vertically aligned CNT based architecture of the CL as shown in Figure 5. The synthesis of CNT based catalyst involves the general steps of: functionalization of CNTs, deposition of Pt onto active sites, and finally the reduction of Pt^{+} to Pt metal. Experimental methods/procedures associated with each of these steps influence the Pt catalyst dispersion. Accordingly, brief review/discussion of the relevant aspects of Pt/CNT catalyst synthesis steps is presented in the following sub-sections.

2.2.2.1 Carbon Nanotubes

Literature related to carbon nanotubes is vast despite the fact that is was recently discovered in 1991. CNTs are typically classified into single walled nanotube (SWNT) or multiwalled nanotube (MWNT). SWNT can be thought of as a graphene sheet that is rolled into a seamless cylinder and MWNT are considered concentric SWNTs [34]. The diameter of SWNTs typically range from 0.5-4 nm and its length is in the order of microns [34]. MWNTs have multiple walls from the obvious lower range of 2 walls to upwards of 10s of walls. The distance between the walls is 0.34 nm, which is equal to the intergraphene distance [34]. The diameter of MWNT can reach up to 100 nm. The different types of CNT are shown in Figure below.

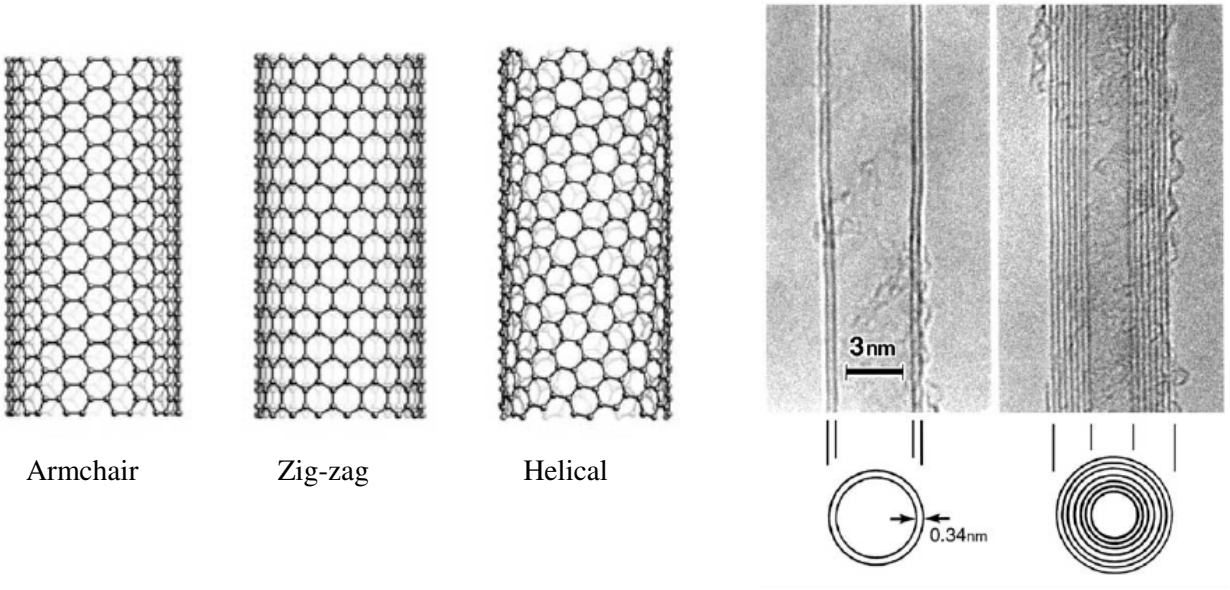

Figure 8: Different Types of Carbon Nanotubes [35]

In comparison to the conventional carbon black support for Pt catalysts, CNTs have higher surface area and electronic conductivities – both properties are preferable for functionality as a support for electro-catalysts. CNTs have specific surface area ranging 200-900 m^2/g [36] compared to 240 m^2/g for Vulcan XC-72 carbon black [37]. The electronic conductivity of CNT has been reported to be 104 S/cm [38] compared to 4 S/cm for Vulcan XC-72 [37]. A CNT as-fabricated is very inert and is not amenable to deposition of platinum on its surface. Although the nature of Pt-CNT interactions is poorly understood and only beginning to being studied [30], it is well known that the CNT surface has to be modified to promote platinum deposition [30].

2.2.2.1 Functionalization of CNT

The main objective of the functionalization step is to introduce oxygen-containing functional groups. Several different approaches have been attempted to functionalize CNTs using different oxidizing agents such as ozone [39,40], permanganate [41,42], and acids [40,43]. Functionalizing CNTs in a 1:1 solution of H_2SO_4 and HNO_3 is considered to yield large number of oxygen-

containing functional groups as determined by XPS [43]. The resulting functional groups are hydroxyl (-OH), carbonyl (-C=O) and carboxyl (-COOH). It is reported that the site ratios of these functional groups are roughly: 4(-OH): 2 (-COOH): 1 (-C=O). It has been proposed that for platinum deposition methods wherein platinum is introduced as an ion (salt) in a liquid medium, an ion-exchange reaction of the following type may occur between the functional group and the catalyst metal ion:

$$\text{CNT-COOH} + M^+X^- \rightarrow \text{CNT-COO}^- M^+ + HX \qquad \textbf{(2-1)}$$

This scheme of CNT functionalization and Pt deposition is depicted in Figure 9 below:

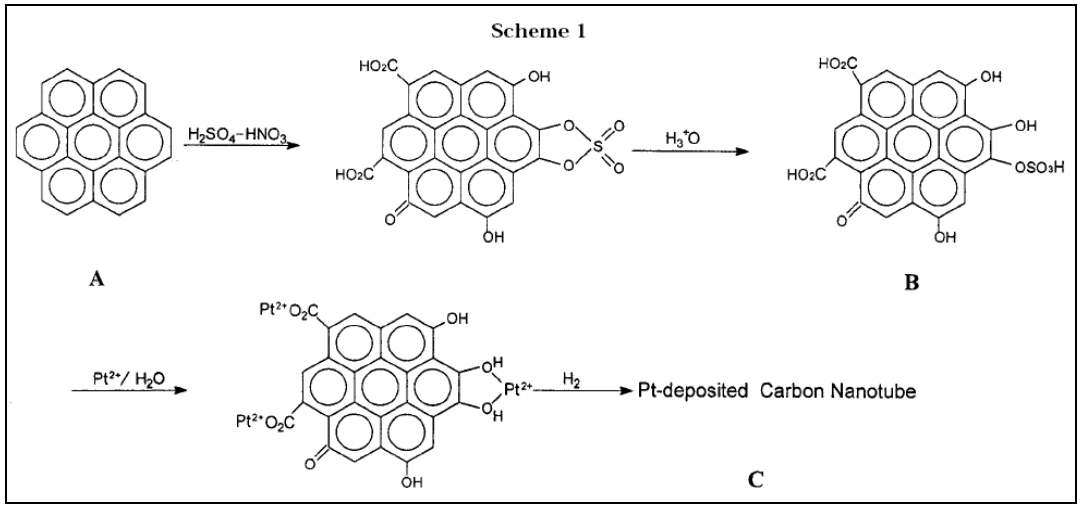

Figure 9: Representation of Scheme for CNT Functionalization and Platinum Deposition by Ion-Exchange Reaction [44]

2.2.2.2 Pt deposition on CNT

Another critical step in the catalyst synthesis procedure is the deposition of platinum onto the CNTs for which a wide variety of methods have been reported, which have been discussed in a recent review article [30], Although some methods that can be categorized as variation of vapor

phase deposition processes have been employed, synthesis methods based on liquid-phase precursors are preferred because they allows particle size control. For catalysis and electrocatalysis, the goal is to keep the catalysts size as small as possible because it equates into large catalytic surface area per mass of catalyst; although consideration must be given to long-term stability. For synthesis of metal nano-particles, four commonly employed liquid-phase precursor methods are – impregnation method, precipitation method, colloidal method and ion-exchange method. The fundamental mechanism for nano-size metal synthesis of each method is not fully understood, although a general understanding of the differences between the methods has been presented by Li and Hsing [43] as depicted in the Figure 10 reproduced from their paper. Briefly, impregnation method involves introduction of the liquid precursor into the catalyst support powder which upon drying leaves metal catalyst salt and with subsequent heating under reducing conditions generates Pt catalysts. In the precipitation method, the catalyst support is introduced into a liquid medium containing the Pt precursor to form a suspension. The precipitant, usually a hydroxide, is added slowly to precipitate out the metal-containing complex and subsequently subjected to a reduction step to generate the metal particles. The basic idea of the colloidal method is to generate the catalyst metal as colloids which are stabilized by the addition of a stabilizer such as polyvinyl propylene (PVP) [44]. The reduction step is achieved simultaneously in-situ; polyols (e.g. *ethylene glycol* - EG) have been employed as a reductant. The stabilizer can act as bridge between the catalyst support and the precipitated catalyst. Recent studies have suggested that EG may be employed as a stabilizer since it breaks down to form acetate at high temperatures which is believed to stabilize metal colloids [45]. In this case no addition stabilizer is required and it is suggested that the metal bonds first to the activated sites on the CNTs and is then stabilized there by the EG. For fuel cell or electrocatalysis application, the removal of stabilizer may be essential to ensure electronic contact between the support and catalyst particle. Finally, the ion exchange method has already been depicted in Figure 9.

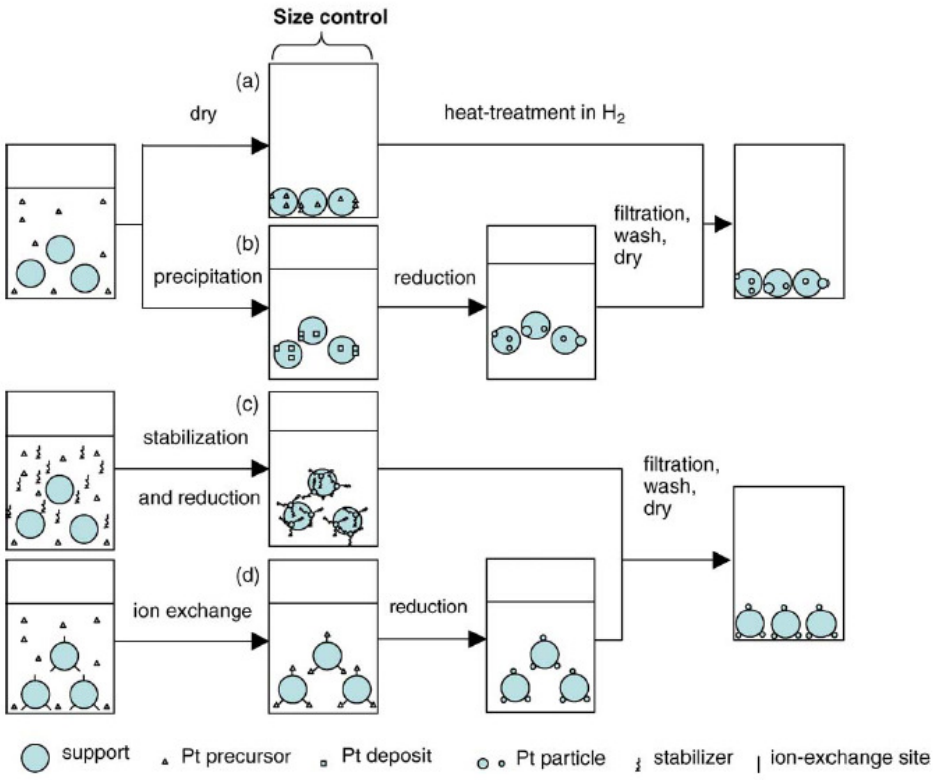

Figure 10: Schematic Depiction of Various Methods for Producing Supported Metal Catalysts (a) Impregnation (b) Precipitation (c) Colloidal (d) Ion-Exchange Methods [43]

Among the various platinum nano-particle synthesis methods [43], the precipitation and colloidal (and its variation) methods have proven to be the most promising methods and are discussed in further detail below

Precipitation Method: A number of studies have reported synthesis of Pt/CNT catalyst by the precipitation method [30,43,46]. A base such as NaOH or KOH was used as a precipitant. The precipitation methods depend on having a mechanically well mixed solution so that the platinum particles are deposited evenly on the CNTs. The Pt^{+} is able to bond to the activated sites on the CNTs and is then reduced by the base to Pt. Size control depends on the solvent used in the method, the agitation of the solution during deposition, the level of functionalization of the CNTs,

the reductant used and its method of addition to the solution. Although higher performance than typical catalysts were observed in catalyst synthesized by this method [46], comparison against other deposition methods [30,43] have suggested that it is not a reliable fabrication method.

Ethylene Glycol or Colloidal Method: Another deposition method and its variation which involves the usage of ethylene glycol (EG) as a reductant and has been referred to as the colloidal method has been reported by many researchers [30,43,47,48,49]. Because the precursor and the catalyst support surface co-exist in the suspension medium, it is not clear whether the metal particles form as a colloid and then deposit on the CNT surface or forms and stabilizes on the surface. It has been found that ethylene glycol is able to support colloidal metal particles in solution creating a well dispersed solution.

Due to its high viscosity, EG prevents the platinum from being transported too quickly to the reaction sites resulting in smaller platinum particle sizes [51]. Optimum EG:water ratios, i.e solution viscosities, have been studied [43,51] and it has been found that 20% water in EG results in the smallest catalyst particles. When the EG/water solution is heated it breaks down to form formaldehyde which acts as a reducing agent for the platinum [43]. The EG method has produced small platinum particle sizes, down to 2 nm [43] which is smaller than the platinum particle sizes of commercial catalysts, typically in the range of 4 nm [50]. Although it has been generally accepted that a higher pH leads to smaller platinum particle sizes [43,46], a systematic study on the influence of pH on this method has not been studied.

A modified colloidal method has been reported [51,52] wherein the deposition and reduction step occurs in a microwave. At high pH conditions for depositions, promising results were reported with average platinum sizes as low as 2.7 nm and electrochemically active areas as high as 96.4

m^2/g_{pt} as compared to the current catalyst active area of 70 m^2/g_{Pt}. It should be noted however that in these experiments the pH has not controlled throughout the duration of the deposition since it is occurring in a closed microwave system, thus the extent of the reaction is not well known.

Based on the results obtained in studies thus far it would be beneficial to examine the effect of different aspects of the deposition procedure. Specifically, since the EG method shows promising results it is important to study the effect of pH on this deposition procedure. The aim is to determine the optimal pH for synthesis of a CNT supported catalyst with small platinum particle size and high electrochemically active surface area.

2.2.3 Characterization of supported platinum catalysts

Novel catalyst created by any method must be compared to the current commercial catalyst to determine their applicability to the fuel cell application. The relevant physical characteristics are - Pt particle size and surface area while pertinent electrochemical kinetic parameters are - Tafel slope analysis and exchange current densities.

2.2.3.1 Physical characterization methods

Common methods of physical characterization for PEMFC catalysts are the determination of Pt particle size by X-Ray Diffractometry (XRD) and Tunneling Electron Microscopy (TEM); [13,50]. Surface area, or more correctly the electrochemically active surface area, of the Pt catalyst is determined by electrochemical technique called cyclic voltammetry. From the knowledge of surface area and the known mass loading of catalyst, mass specific surface area (in m^2/g). For platinum supported on carbon, the benchmark values of the catalyst size are 2-4nm, which correspond to mass specific area of 36-72 m^2/g_{Pt} [13,50]. An example of high resolution TEM image of Pt supported on carbon is shown below.

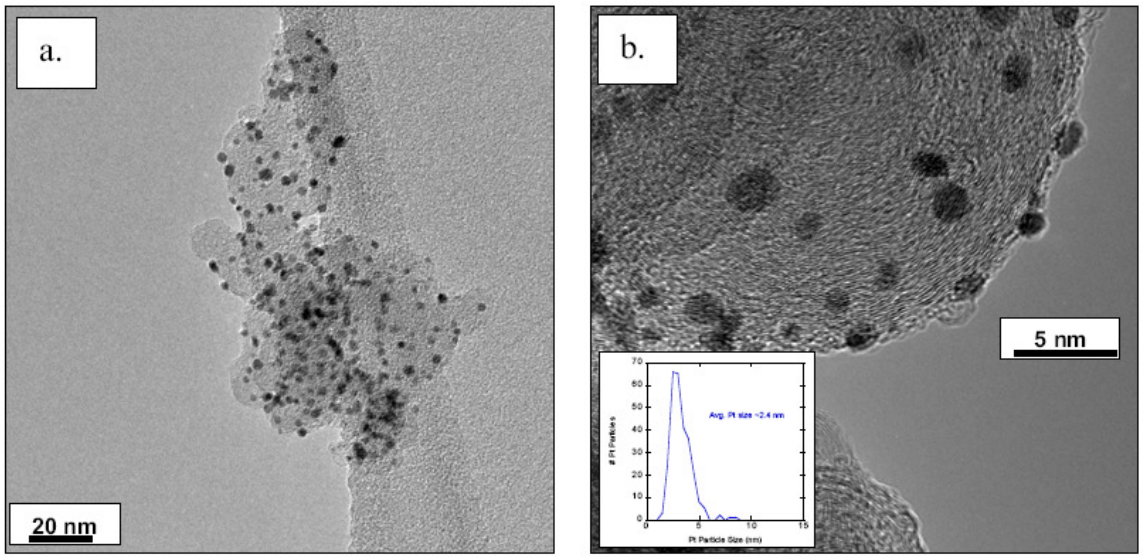

(a) (b)

Figure 11: Transmission Electron Microscopy Images of (a) agglomerated Vulcan XC-72 spherical carbon support showing uniform Pt dispersion of starting E-TEK powder and (b) individual Pt particles on surface of a single spherical carbon support [32]

2.2.3.2 Electrochemical Kinetic Characterization of PEMFC Catalysis

As stated in the preceding sub-section, the electrochemically active surface area is determined by standard cyclic voltammetry (CV) technique which is discussed in detail in Chapter 3 (Section 3.2.2.3). The characterization of electrochemical kinetics is specific to the type of reaction to be examined. For PEM fuel cells, the two main reactions of interest are the oxygen reduction reaction (ORR) and hydrogen oxidation reaction (HOR). This thesis is concerned with use of Pt/CNT catalyst for the cathode side (where ORR occurs) of the PEM fuel cell. Accordingly, the discussion below is limited to ORR kinetics. The electrochemical kinetics of ORR on Pt catalyst has been well studied in liquid electrolyte system using rotating disk electrode (RDE) systems [53]. One the other hand, the ORR kinetics under fuel cell operating conditions – i.e., polymer electrolyte and gaseous reactants – has been reported in only few studies [54,55].

Electrochemical characterization in liquid-electrolyte systems (Rotating Disk Electrodes): The RDE technique for studying ORR kinetics has been discussed in detail in Chapter 3 and also been recently summarized [50]. The kinetic parameters of interest are the exchange current density or Io (equivalent to pre-exponential factor in chemical rate constant) and Tafel slope, also described in Section 3.2.4, have been reported for Pt catalyst in acidic electrolyte. One group [56] has studied the effect of the electrolyte on the kinetics in order to gain insight into the reaction mechanism and determine manners in which the kinetic parameters may be improved. In the region of mixed kinetic-diffusion control there has commonly been 2 different Tafel slopes observed, 60 and 120 mV/dec. The change in slope from 120 mV/dec to 60 mV/dec typically occurs at 0.8 V vs *Standard Hydrogen Electrode* (SHE) and is believed to be due to the adsorption of –OH groups onto the Pt. There are still two common views for the first reaction step in the mechanism. The first view involves a simultaneous proton and charge-transfer step involving $O_2 \Leftrightarrow O_2(ads)$ followed by a rate determining charge transfer step described by: $O_2(ads) + H^+ + e^- \rightarrow products$. This mechanism is supported by experiments run to display pH and pressures dependencies of the reaction. The region below 0.8 V is described by Langmuirian kinetics while the region with a Tafel slope of 60 mV/dec was described by assuming oxygen adsorption under conditions with –OH present as a platinum poison. The second commonly supported mechanism involves dissociative chemisorption of O_2 onto the platinum, likely occurring simultaneously with the charge transfer. The primary difference between the two mechanisms is that the first involves only 1 platinum site while the second mechanism considers 2 adjacent sites. In this study a lower inherent activity for the oxygen reduction of Pt alloy electro-catalysts when the effect of –OH poisoning is removed, either by introducing a higher acidity environment or by removing concomitant poisoning with other anodic species, provides promising insights into possible increases in the ORR kinetics. In any case, the Tafel slope and exchange current densities are common kinetic parameters evaluated and compared for PEMFC

catalysts. In the study investigating the effect of the solvent on the kinetics [56], the Tafel slope and exchange current densities were determined by RDE studies at a rotational speed of 1225 and at a variety of electrolyte concentrations. For a 1M H_2SO_4 electrolyte, the $\log(I_o)$ for a 20% Pt/C Catalyst at room temperature was determined -6.19 mA/cm^2.

Fuel Cell Testing: Once catalysts have been screened experimentally in RDE type setup, it is of interest to determine the activity of catalyst in a working fuel cell. Typically, researchers fabricate membrane electrode assembly (MEA) comprising the polymer electrolyte membrane with catalyst layers on each side. Extraction of electrochemical kinetic parameters from a fuel cell polarization data is complicated because of difficulty in delineating the ohmic and mass transport losses described in section 1.2.1 Nonetheless, the kinetics have been obtained by analysis of the iR-free (ohmic loss compensated) plots of potential versus logarithm of current (i.e. the Tafel plot) for oxygen reduction reaction. In one study [57], kinetic information was extracted from fuel cell data to compare typical catalyst layer performance to that of a catalyst layer deposited by sputtering. The exchange current densities were found to be 5.4×10^{-4} mA/cm^2 and 1.5×10^{-4} mA/cm^2 for the sputtered and conventional catalyst films, respectively. This study suggests that the sputtered film improves the kinetics of the ORR. The base catalyst in each case was the same, although the method of catalyst layer fabrication was altered. The difference in the exchange current densities obtained is likely due to the difference in microstructure of the catalyst layer and not to the actual Pt-C particles.

Effective Oxygen Diffusivity in the Ionomer Phase of the Catalyst Layer: Transport properties – effective diffusivity of gaseous oxygen or hydrogen in the pores, effective diffusivity of oxygen or hydrogen dissolved in the ionomer phase, effective electronic conductivity, and effective protonic conductivies – of the PEMFC catalyst layers are important input parameters for

computational models which can affect the what optimum design and structure is predicted from such models. Experimental measurements of these properties will not only improve the predictive capability of these computational models but also provide insight into the microstructural features of the CL. Consider diffusivity of oxygen in the ionomer phase of the CL. Due to the composite nature of the CL, the diffusion coefficient of oxygen in solid ionomer (i.e. non-composite) material would have to be modified to account for partial occupation of the CL by the ionomer phase to yield an effective diffusivity defined in general terms as:

$$D_i^{eff} = f(\varepsilon) D_i \qquad \textbf{(2-2)}$$

The function $f(\varepsilon)$ denotes the functional form of dependency of the volume fraction (ε) of the relevant phase (ionomer phase in present discussion). It is of interest to determine the functional relationship $f(\varepsilon)$ so that appropriate effective properties can be employed for simulation. Further, the function can provide insight into the the distribution/structure of the relevant phase in the CL. For example, the widely employed function $f(\varepsilon) = \varepsilon^{1.5}$ also known as the Bruggeman relation captures the effective transport through a packing of spherical particles.

While the oxygen transport properties in the CL have not been investigated in ex-situ testing, some electrochemical analysis has been done on Nafion® membrane to determine the diffusion of oxygen through a Nafion® film [60]. All studies on oxygen diffusivity in polymeric ionomers have been carried out on polymer electrolyte membranes and not on composite structures representative of the catalyst layer.

2.2.4 Oxygen diffusivity in Polymer Electrolyte Membranes

A few methods, gas chromatography based and electrochemical based, are available to determine the diffusivity of a gas through a film or membrane.

Solid state microelectrode method: A method which is becoming more common for determining oxygen permeability in the polymer membrane is the use of a micro-electrode set-up as seen below in Figure 12.

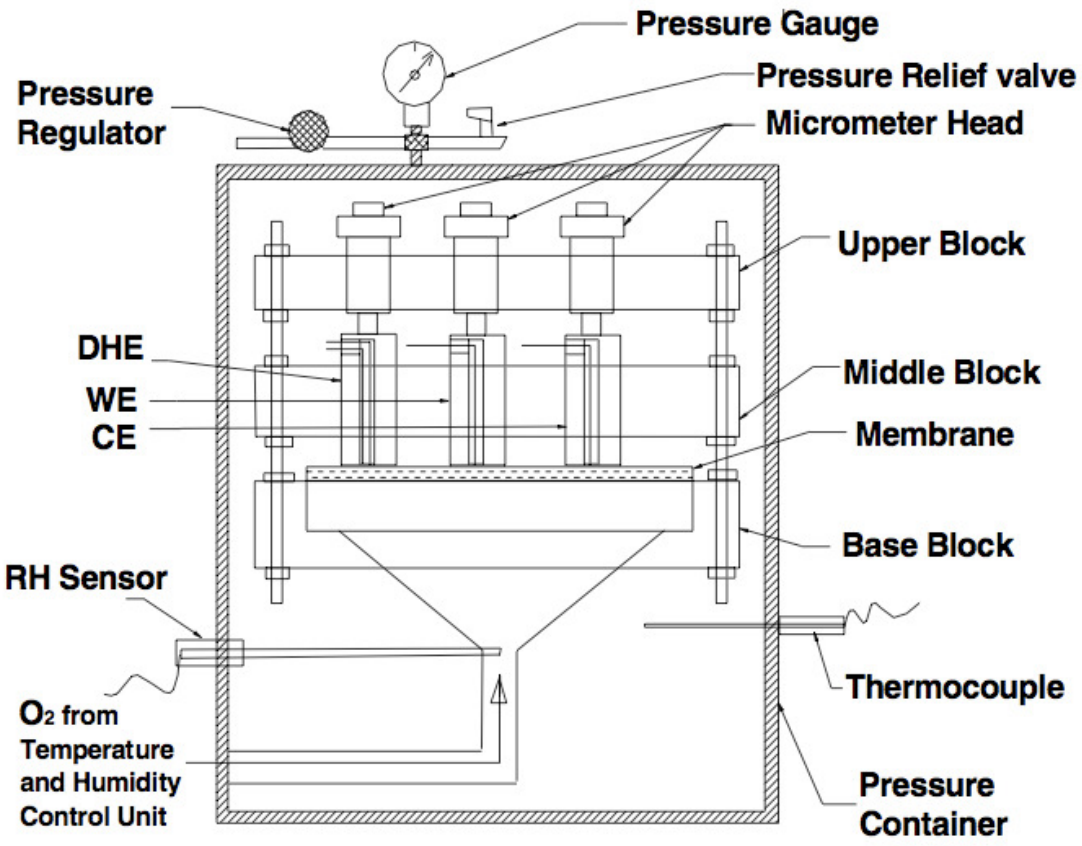

Figure 12: Solid State Micro-Electrode Apparatus for Determining Permeability of Oxygen Through Nafion Film [54]

Chronoamperometry experiments are used to determine the diffusion of oxygen through the Nafion® membrane. In these experiments the potential is brought to a region which is diffusion controlled and the current-time behaviour is utilized to determine mass transport properties. This method has been studied in detail to examine the effect of temperature and pressure on the diffusion of oxygen through a pure Nafion® membrane. These studies determined that the

diffusivity of oxygen through Nafion® increases with increases in temperature and pressure. The permeability at 100% RH, 323 K and 3 atm O_2 was reported to be 5.19×10^{-11} mol/cm.s [58] and at 273K and 1.55atm it was reported to be 1.25×10^{-11} mol/cm.s [54]. Interestingly, these studies have considered the membrane to be a macro-pore free film. The membrane has not been examined for the presence of pores. If the Nafion® film contains any pores the material transport property – oxygen diffusivity - being measured will be an effective property and the value obtained must be corrected for the porosity in order to determine the intrinsic material property.

Gas chromatography based method: Another method which has been employed to determine the diffusivity of oxygen through Nafion® membranes is gas chromatography based method [59]. This method uses experimental system similar to the solid state micro-electrode set-up wherein Nafion® membrane is pressed between two stainless steel plates, one with a gas inlet and one with a gas outlet as seen below in Figure 13. The oxygen is fed to the inlet and the gas chromatography unit determines the outlet flow of oxygen. These experiments were conducted under varying temperatures, pressures and membrane hydration values. The results showed that as expected permeability increases with temperature and the values ranged from 8.5×10^{-12} up to 13.5×10^{-12} mol/cm.s for 20 to 80^{o}C. The oxygen permeability was also found to be higher for gases with higher humidity. In this method the porosity of the Nafion® was again not considered the property being reported may therefore being an effective diffusivity.

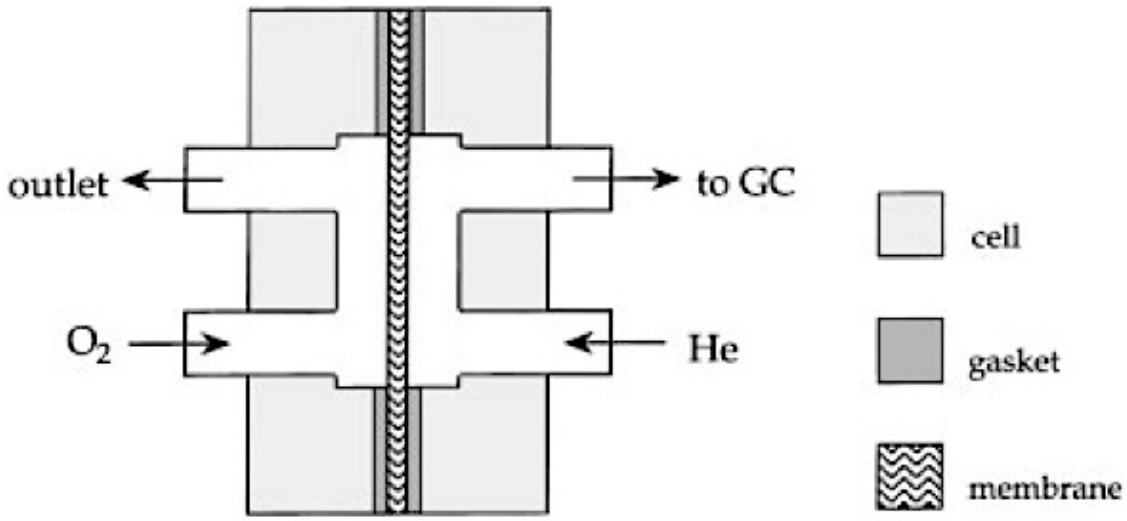

Figure 13: Gas Chromatography Set-up For Determining Oxygen Permeability Through Nafion Membrane [59]

RDE based liquid electrochemical method: Although microelectrode studies are a more representative method of mimicking PEMFC operational conditions, research has also been done on determining mass transfer properties by electrochemical methods [60]. In this study, a Nafion® film was deposited onto the working electrode of a rotating disk electrode by micro-syringe and allowed to dry. The thickness of the film in its dry state was determined by a Dektak Surface Profile Measuring system. The method of determining thickness is of importance when considering the effective nature of the property being investigated. This is because the thickness may be used to determine the porosity of the film which should be considered when investigated effective properties. RDE experiments were carried out in an oxygen rich electrolyte. The rotational speed of the electrode was varied from 1600 to 2900 rpm. With analysis described in Chapter 3, the limiting current and peak currents for the film-covered electrode can be compared to those of the bare electrode to obtain the diffusion coefficient. For inert films, the following relationship according to Gough and Leypoldt was used:

$$\frac{\alpha D_f}{\delta_f} = \frac{i_L}{\left(i_L / i_D - 1\right) nFC_{sol}} \qquad \textbf{(2-3)}$$

Based on this equation the product $D_f C_f$ can be determined. The linear dependence of the peak current on the sweep rate can be used in the following manner to determine $D_f^{1/2} C_f$ as follows:

$$i_p = 3.0 \times 10^5 n(\beta n_a)^{1/2} C_f D_f^{1/2} (dV/dt)^{1/2} \qquad \textbf{(2-4)}$$

This equation was developed in the case of slow interfacial charge transfer kinetics and it was assumed that the electrode was a smooth Pt electrode leading to a βn_a value of 0.5.

From both the peak current (i_p) and limiting current (i_L) data collected the diffusion coefficient of oxygen was determined in the Nafion® film and was found to agree with literature values when the wet thickness of the film was assumed to be 65% greater than that determined by the profile measuring system. The value for permeability of oxygen in Nafion® obtained in these experiments was reported to be 1.24×10^{-11} mol/cm.s. Again, in this study, the presence of macro-pores in the Nafion film was not examined. That the Nafion film thickness had to be artificially increased to match with the literature values for Nafion membranes, is indicative of the porous nature of the Nafion® film deposited on the electrode.

There has been a limited amount of work done on the mass transfer properties through Nafion® by electrochemical analysis. No studies have been completed on the micro-structure of the Nafion® to determine if it is porous in nature in either a film or membrane form and the effect of this has

been largely disregarded. Furthermore no research has attempted to carry out experiments to determine the mass transport properties of oxygen through catalyst films (carbon/Nafion® films) rather than solely through the Nafion®. Adding carbon to a Nafion® solution significantly changes its structure and will, therefore, change the oxygen transport properties. It would be beneficial to obtain insight into the catalyst mass transfer properties since this limits PEMFC performance.

Chapter 3
Experimental Method and Background Theory

This chapter presents the details of the experimental methods and relevant background theory for – (a) oxygen permeability measurements and (b) synthesis of platinum (Pt) supported on carbon nanotube (CNT) catalyst and characterization thereof

3.1 Determination of Oxygen Permeability in Ionomer-Carbon Composite Film

One of the objectives of the thesis was to explore experimental methods for characterization of a key transport property of the catalyst layer. More specifically, it was of interest to investigate if the effective permeability of oxygen in carbon-ionomer films could be experimentally measured. It may be useful to recall that in the PEMFC catalyst layer, dissolved oxygen diffusion through the porous ionomer phase of the solid matrix (Pt/C-ionomer) of the catalyst layer occurs and is an important transport process. The key parameter that describes the oxygen transport is the product of diffusion coefficient and solubility, which is known as permeability in this field.

In this study, oxygen permeability was measured using a rotating disk electrode system.

3.1.1 Physical Description of Rotating Disk Electrode and Associated Processes

A brief description of the main component of the experimental system – rotating disk electrode – and the key processes occurring therein during the oxygen permeability measurement is presented prior to providing theoretical background. This is to allow the reader to develop a physical image of the system and relevant physics.

The rotating disk electrode (RDE) consists of a disk of the electrode material imbedded in a casing of insulating material, commonly a plastic as shown in Figure 14. The electrode material, a smooth Pt surface is coated with an ionomer-carbon film. As shown in Fig 14b, to ensure film

coverage only over the Pt electrode, an adhesive tape with a hole the size of electrode is applied during film preparation. The film coated electrode is placed in an oxygen-saturated liquid electrolyte. The electrochemical reduction of oxygen at the Pt surface drives the flux of oxygen through the ionomer-carbon film. The oxygen flux is related to the electrical current which is readily measured and monitored. The maximum or limiting current that can be drawn is limited by the maximum amount of oxygen that can be transported to the electrode surface and is a function of the electrode rotational speed and oxygen diffusion/solubility property of the film. Provided the film thickness is known, the 'effective' permeability can be computed from the measured limiting current and known rotational speed based on theoretical treatment developed by Levich [71], as discussed in section 3.1.2.

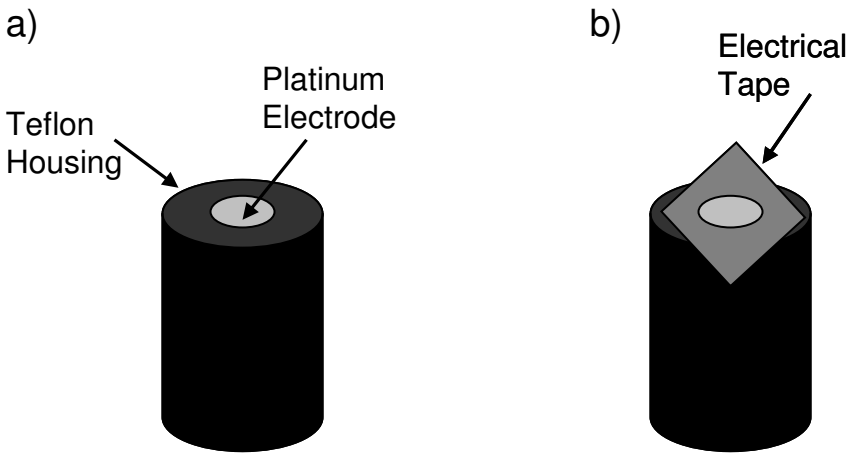

Figure 14: Schematic representation of rotating disk electrodes, (a) Platinum electrode housed in Teflon (b) Platinum Electrode Prepared for Ionomer-Carbon Film Deposition

3.1.2 Theory of Rotating Disk Electrode

3.1.2.1 Bare or uncoated electrode

A smooth rotating disk submerged in a fluid develops a well-defined velocity profile at steady-state (see Appendix A) as shown in Figure 15 such that near the electrode surface (i.e. for small y) the following approximate solution exists

$$v_r = -0.51\omega^{3/2}\nu^{-1/2}y^2$$
$$v_y = 0.51\omega^{3/2}\nu^{-1/2}ry \qquad \textbf{(3-1)}$$

where, r and y are the radial and axial coordinate (perpendicular to surface). And, v_r is the velocity of fluid in the radial direction, v_y is the velocity of fluid in the y direction, ω is the rotational speed of the electrode, and ν is the kinetic viscosity of the fluid.

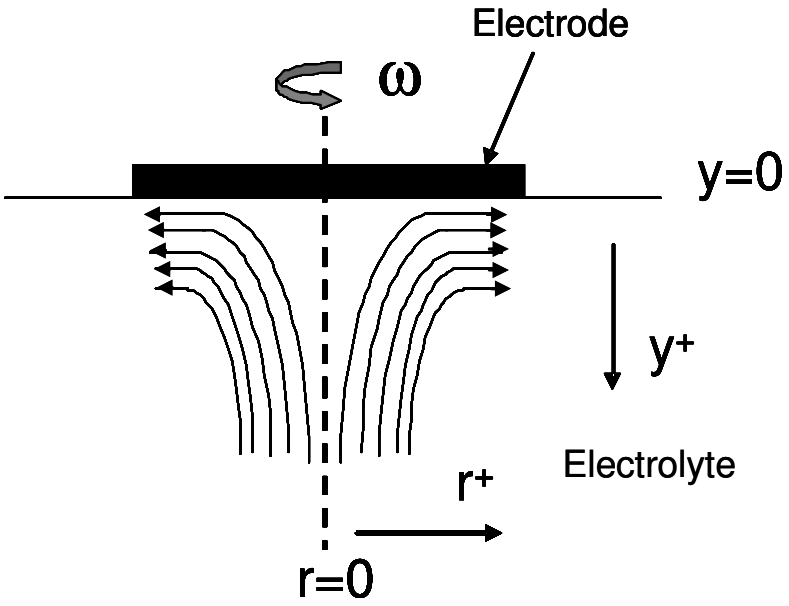

Figure 15 : Velocity Profile of Gas Saturated Electrolyte to Bare Electrode

When a reactant (oxygen) solubilized in the liquid-phase (an electrolyte e.g. H_2SO_4) is consumed at the electrode surface via an electrochemical reaction, the convective-diffusive transport of the reactant to the electrode surface is described by the following species balance equation:

$$v_r\left(\frac{\partial C_o}{\partial r}\right)+v_\phi\left(\frac{\partial C_o}{\partial \phi}\right)+v_y\left(\frac{\partial C_o}{\partial y}\right)=D_o\left[\frac{\partial^2 C_o}{\partial y^2}+\frac{\partial^2 C_o}{\partial r^2}+\frac{1}{r}\frac{\partial C_o}{\partial r}+\frac{1}{r^2}\left(\frac{\partial^2 C_o}{\partial \phi^2}\right)\right] \quad \textbf{(3-2)}$$

An expression for maximum possible flux, i.e. when surface concentration is zero or C(y=0)=0, can be obtained solving the above equation with the velocity profiles defined by equation 3-1. This expression presented below (see Appendix A.2 for detailed derivation) was originally derived by Levich [71]:

$$D_o\left(\frac{\partial C}{\partial y}\right)_{y=0}=0.62AD_o^{2/3}\omega^{1/2}\nu^{-1/6}C_o^* \quad \textbf{(3-3)}$$

where, D_o is the diffusion coefficient of the reacting species, A is the area of the electrode, ω is the rotational speed of electrode, and C_o* is the concentration of the component in the bulk solution.

For the electrochemical reaction at the surface, the associated maximum or *limiting current* (i_l) is then readily obtained from Faraday's law:

$$i_{lc}=0.62nFAD_o^{2/3}\omega^{1/2}\nu^{-1/6}C_o^* \quad \textbf{(3-4)}$$

The above equation is commonly known as the Levich equation. The linear plot of i_l versus $\omega^{0.5}$ then allows the determination of D, if the solubility concentration of the reactant, Co* is known.

Illustration via Boundary Layer Concept

The limiting current can also be described in terms of a boundary layer concept as depicted in the Figure 16. All of the concentration gradient is considered to occur within a thickness δ_n – the diffusion boundary layer. Since no reaction occurs within this boundary layer and the transport is essentially described by diffusion, the net flux to the surface can be given by the following equation:

$$D_o\left(\frac{\partial C}{\partial y}\right)_{y=0} = D_o \frac{(C_o - C_s)}{\delta_n} \qquad \textbf{(3-5)}$$

Under limiting current density condition, the surface concentration $C_s = C(y=0)$ is equal to zero. Thus, the limiting flux is:

$$D_o\left(\frac{\partial C}{\partial y}\right)_{y=0}\Bigg|_{limiting} = D_o \frac{C_o}{\delta_n} \qquad \textbf{(3-6)}$$

From equations (3-3) and (3-6), it can be readily derived that the diffusion boundary layer (δ_n) is:

$$\delta_n = 1.61 D_o^{1/3} \omega^{-1/2} \nu^{1/6} \qquad \textbf{(3-7)}$$

It can be noted that the boundary layer is a function of the rotational speed and the reactant diffusivity.

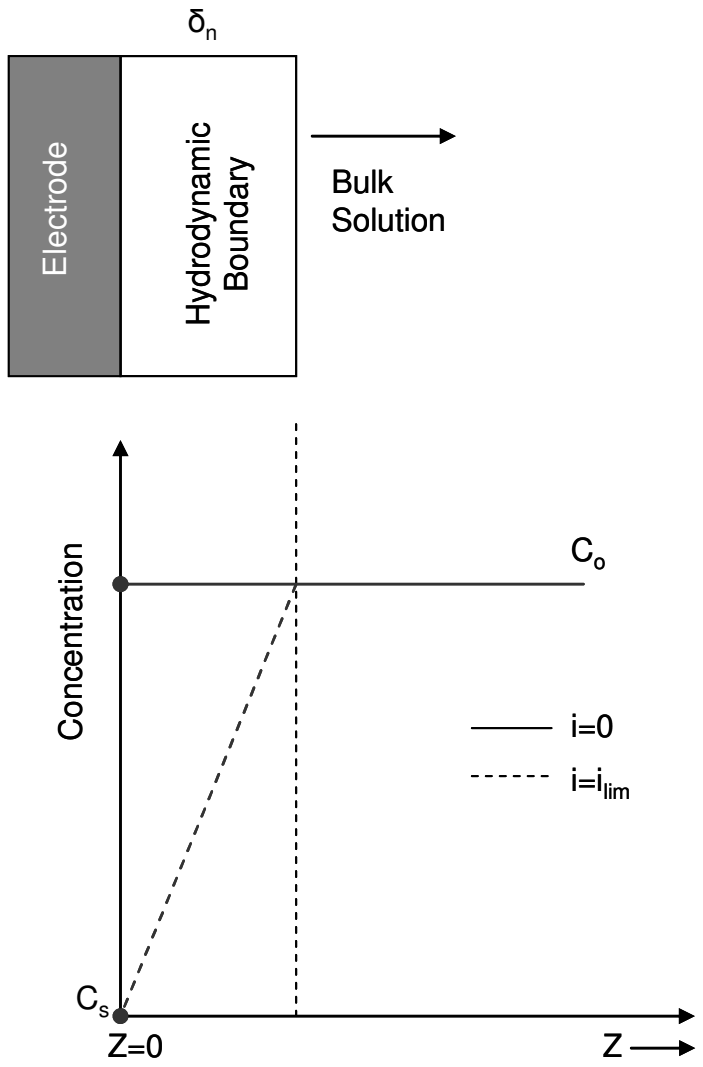

Figure 16: Concentration Profile of Oxygen in Hydrodynamic Boundary Layer and Bulk Solution

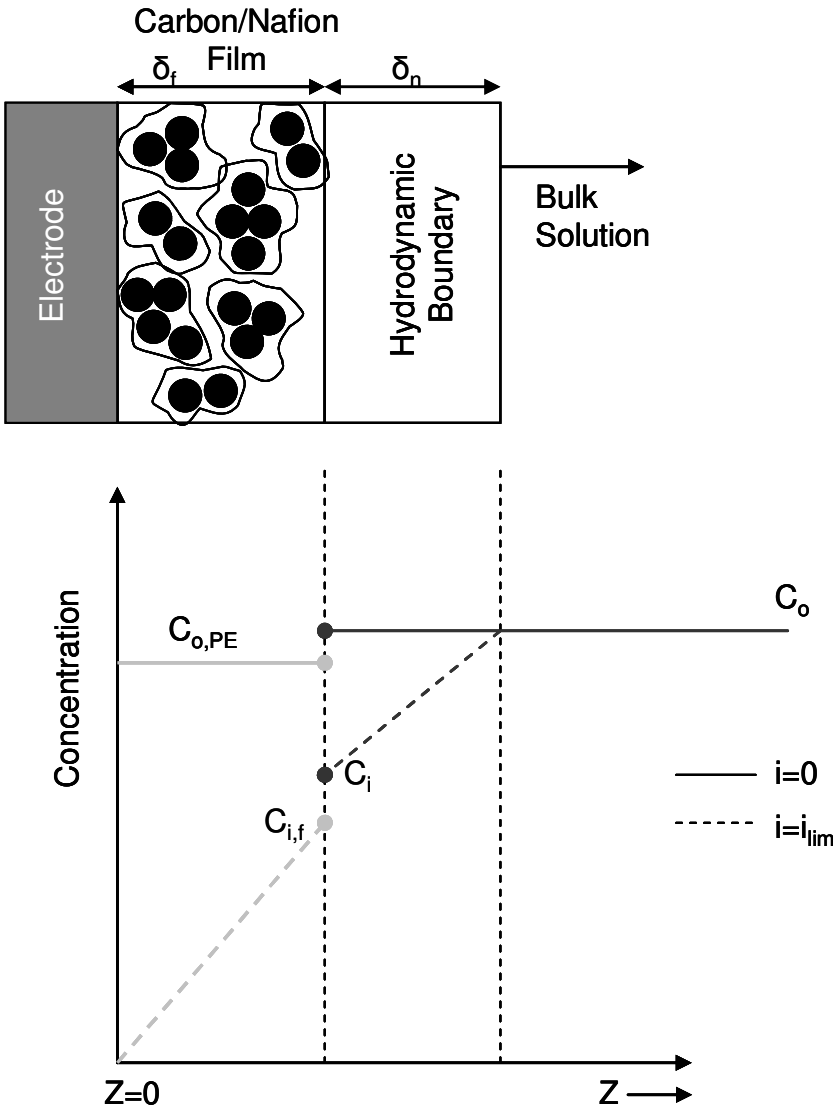

Figure 17: Concentration Profile of Oxygen in Hydrodynamic Boundary Layer, Catalyst Film and Bulk Solution

In the next section, the boundary layer concept will be applied to derive an expression for limiting current of RDE covered with a film.

3.1.2.2 Electrode covered with thin film

For the electrode covered by a thin film, the fluid flow outside the rigid film is assumed to be the same as that for a bare electrode as shown in Figure 18 below. The film is considered to be a

smooth surface insofar as the fluid flow in considered. This assumption is necessary to maintain the outlined theoretical treatment.

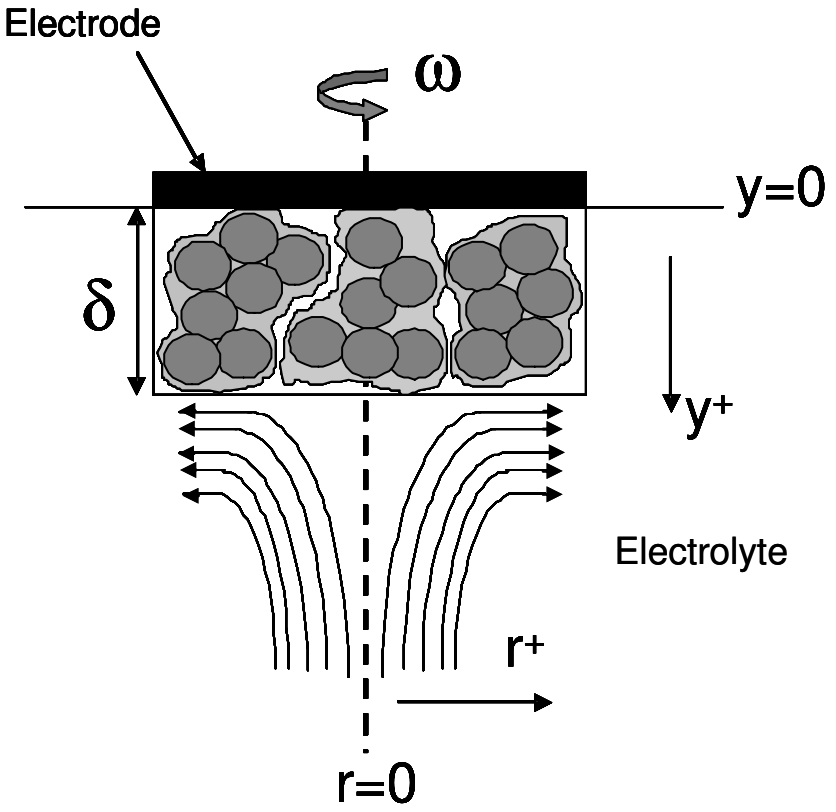

Figure 18: Velocity Profile of Gas Saturated Electrolyte to Filmed Electrode

Now, an additional resistance to the transport of the reactant (oxygen) from the liquid to the electrode surface is offered by the film. If the film is assumed to be rigid, a reasonable assumption for a polymer or polymer composite film, then the transport of the reactant through the film can be treated to be a diffusive process. Under the conditions that the reactant is being consumed at the electrode surface, the overall process can be broken down into the following steps – convective-diffusive transport in the liquid, dissolution of the reactant into the film followed by diffusive transport through the film and ultimately the reaction at the electrode surface. Now, the diffusive-convective transport in liquid has already been discussed in section 3.1.2.1. The

solubility of the reactant in the liquid and the film is expected to be different. Invoking the equilibrium assumption at the interface between the liquid and the film, the concentration of the species just outside the film [$C_i(\delta^+)$] differs from that within [$C_{i,f}(\delta^-)$] by the following partitioning coefficient:

$$\kappa = \frac{C_{i,f}(\delta^-)}{C_i(\delta^+)} \qquad \textbf{(3-8)}$$

where, δ describes the film thickness. The diffusive transport through the immobile film can be described via Fick's law.

At steady state, the reactant flux is same through any cross-section within the diffusion boundary layer and film domain, and accordingly we have:

$$D_o \frac{(C_o - C_i)}{\delta_n} = D_f \frac{(C_{i,f} - C_{s,f})}{\delta_f} \qquad \textbf{(3-9)}$$

Invoking the equilibrium assumption at the liquid-film interface, the interfacial concentration C_i and C_{if} are related via equation 3-8.

The maximum flux that can be attained is under the conditions that the surface concentration tends to zero. Under such condition, which is equivalent to limiting current condition, equation 3-9 reduces to:

$$D_o \frac{(C_o - C_i)}{\delta_n} = D_f \frac{C_{i,f}}{\delta_f} = D_f \frac{\kappa C_i}{\delta_f} \qquad \textbf{(3-10)}$$

And, we get

$$(\frac{D_o}{\delta_n})C_o = (\frac{D_o}{\delta_n} + \frac{\kappa D_f}{\delta_f})C_i$$

or **(3-11)**

$$C_i = \frac{(\frac{D_o}{\delta_n})}{(\frac{D_o}{\delta_n} + \frac{\kappa D_f}{\delta_f})} C_o$$

Thus, the maximum or limiting flux can be written in terms of the diffusion coefficients, boundary layer and film thicknesses, and bulk concentration (Co), from equation (3-10) and (3-11), as follows:

$$J_{c,\lim} = \frac{\kappa D_f}{\delta_f} C_i = \frac{(\frac{D_f \kappa}{\delta_f})(\frac{D_o}{\delta_n})}{(\frac{D_o}{\delta_n} + \frac{\kappa D_f}{\delta_f})} C_o$$

or **(3-12)**

$$\frac{1}{J_{c,\lim}} = \frac{\delta_n}{D_o C_o} + \frac{\delta_f}{\kappa D_f C_o}$$

Substituting the value of δ_n from equation (3-7), we get:

$$\frac{1}{J_{c,\lim}} = \frac{1}{0.62 D_o^{2/3} \omega^{1/2} \nu^{-1/6} C_o} + \frac{\delta_f}{D_f \kappa C_o} \quad \textbf{(3-13)}$$

The associated limiting current can be obtained readily from the Faraday's law:

$$\frac{1}{i_{\lim}} = \frac{1}{0.62\, n\, F\, A\, D_o^{2/3} \omega^{1/2} \nu^{-1/6} C_o} + \frac{\delta_f}{n\, F\, A\, D_f \kappa C_o} \qquad \textbf{(3-14)}$$

The limiting current can be measured experimentally and a plot of $1/i_{lc}$ vs. $\omega^{-1/2}$ should yield a constant slope regardless of whether the electrode is covered with a film or not. The intercept of such a plot is $\frac{\delta_f}{nFAD_f \kappa C_o}$ when a film of thickness δ_f is present or zero when no film is present.

The permeability ($= D_f \kappa C_o^*$) of the reacting/diffusing species can be easily obtained, provided the film thickness is known. Further, if the partitioning coefficient (κ) is known, the diffusion coefficient can be determined.

In the current study, the permeability of oxygen in the films of ionomer-carbon composite is being evaluated. Owing to the composite nature of the film, the measured property – permeability - is actually an *effective* property. This is due to the tortuous nature of the path through which diffusion must occur.

The velocity profile used in this discussion (Equation 3-1) was developed for the area very close to the bulk boundary. In order for the following development to be valid the thickness of the film must be less than the thickness of the boundary layer described by the velocity profile. This ensures that the velocity profile previously developed can still be used.

3.1.3 Experimental Method

3.1.3.1 Experimental Setup

The experimental setup employed for oxygen permeability is shown schematically in Figure 19a. The key components of the setup are the BASi-2 rotating disk electrode (RDE), seen in Figure 19b, a specially designed glass 3-port flask which is able to create a salt bridge between the compartment containing the electrode and that containing the counter electrode, a BASi Ag/AgCl reference electrode, a thin wire platinum counter electrode and a SI 1287 Solartron Analytical potentiostat. The working electrode consists of a disk of the platinum electrode material imbedded in a casing of insulating material, commonly a plastic. The rod of insulating material is attached to a motor so that it can be rotated at different speeds.

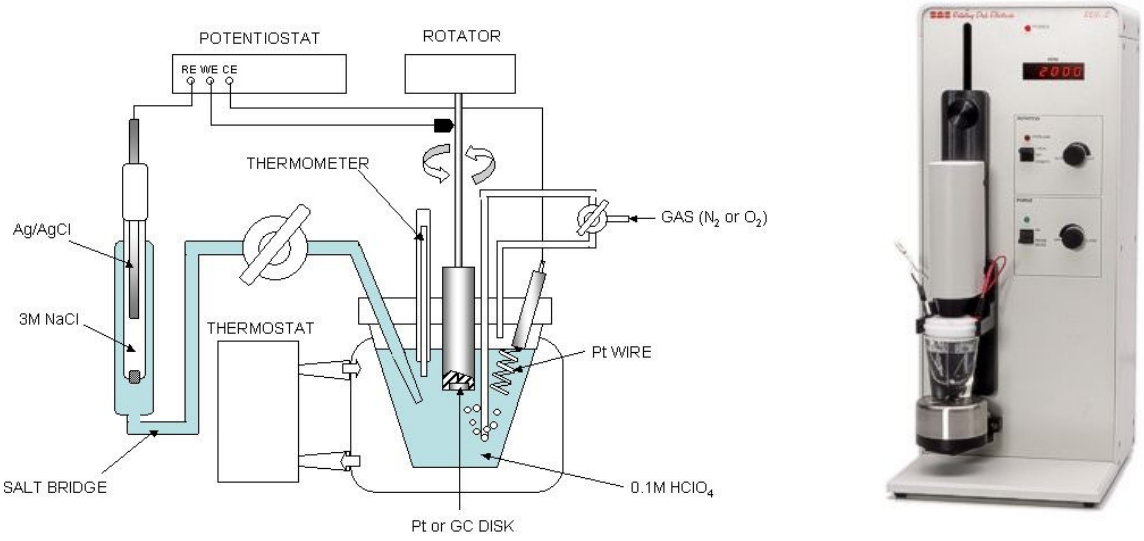

(a) (b)

Figure 19: (a) Schematic diagram of the rotating disk electrode setup and (b) Picture of RDE BASi apparatus

3.1.3.2 Material

The ionomer used in fabricating carbon-ionomer films was a 5wt% Nafion® solution (Alfa Aesar) - Perfluorosulfonic acid-PTFE copolymer. The carbon source for the solutions was carbon black Vulcan XC72 (Cabot) with particle diameters of 30 nm. The electrolyte used in the RDE experiments was a 0.1M Perchloric Acid, $HClO_4$, obtained from Fluka Chemical Company. The oxygen used in electrochemical evaluation of the catalyst activity was of ultra high purity (grade 4.3), and was obtained from Praxair, Canada. The argon used in RDE experiments was provided in house, and was of 99.997% purity.

3.1.3.3 Ionomer-Carbon Film Preparation

For fabrication of ionomer-carbon film of desired carbon content, a suspension was first prepared by adding a known amount of carbon to a mix of 1000μL of 5 wt% Nafion® solution, 7 mL of de-ionized water and 3 mL of isopropanol. The RDE electrode upon which the film was to be deposited was covered with an electric tape that has a hole slightly larger than the electrode area. The hole was cut using a leather hole punch. The electrode was then loaded with ten 5μL droplets. The tape ensured that the suspension remains restricted to the electrode area. It was also ensured that each drop did not dry completely before the next drop was deposited; this stopped the Nafion® from forming individual layers before all the solution is deposited.

Cyclic voltammetry was run on each coated electrode to ensure that the film was saturated in the liquid electrolyte, resulting in a stable response prior to RDE experiments.

3.1.3.4 Physical Characterization Ionomer-Carbon Film

In the early stage of the thesis work, the film thickness was estimated assuming a uniform dense film. At a later stage, a laser-based tool for surface pofilometry was made available. This equipment was 3D Cobra surface scanner *Optical Gaging Product* (OGP). The ionomer carbon films were prepared on glass micro-slides (see Figure 20 below) by following the same procedure

as that for coating electrodes with films. The electrical tape was carefully removed and the micro-slide with film was subjected to laser scanning. The measurement yielded a three-dimension profile of the film. The image was then analyzed using the associated software package Talymap to obtain the thickness profile and also the volume of the film. The porosity of the film was calculated from the laser measured film volume and the ionomer-carbon volume from known composition.

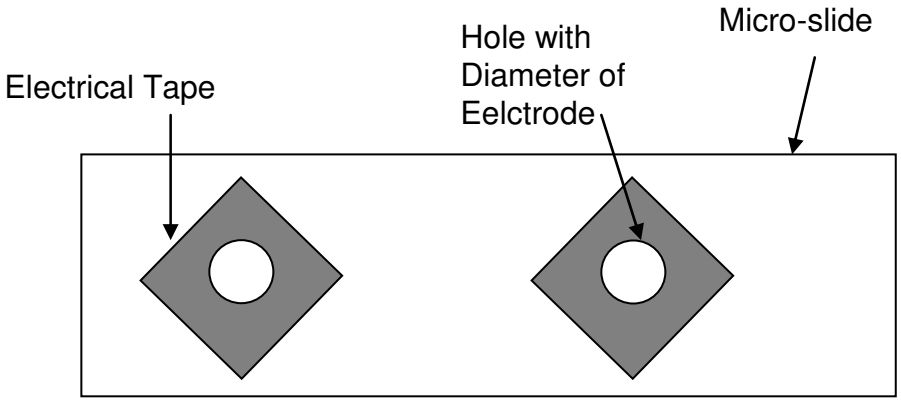

Figure 20: Depiction of micro-slide preparation of films

3.1.3.5 Procedure for Permeability Measurements for Ionomer-Carbon Films

The underlying theory for permeability measurement has been presented in 3.1.2.2. The basic idea is to measure the limiting current as a function of rotational speed for smooth Pt electrode covered with ionomer-carbon film. The film was prepared by method described in section 3.1.3.3 and the experiments were carried out in the setup described in section 3.1.3.1.

The experiment was initiated by saturating the electrolyte, 0.1 M $HClO_4$, with oxygen at atmospheric pressure and room temperature (24^oC) by allowing the gentle bubbling of oxygen for 30 minutes. The rotational speed of the disk electrode was set to a known level. The potential was swept from -0.2 to 1.2 V, measured against Ag/AgCl Reference Electrode. The current was measured during the scan and the resulting limiting current was determined. The rotational speed was then changed to the next higher level and experimental procedure describe above repeated.

Experiments were carried at the following rotational speeds: 1000, 1300, 1600, 1900, 2200 and 2500 rpm. The potential sweep was carried out for 10 cycles at which point a steady response is obtained. A plot of limiting current versus inverse of square-root of rotational speed was generated and the permeability was determined by the method described above.

3.2 Catalyst Synthesis and Characterization

3.2.1 Catalyst Synthesis

The general approach to fabrication of platinum dispersed on carbon support is described in Figure 21 below. The first step is to functionalize the carbon nanotubes to introduce surface functional groups for platinum deposition to occur. The deposition step occurs by adding H_2PtCl_6 to a suspension containing the CNTs. The $PtCl_6$ is allowed to bond to the defect sites on the CNTs by reacting for a certain amount of time. The final step in the deposition procedure is to reduce the $PtCl_6$ to Pt. A variety of methods is available which in many cases depends on the type of suspension media employed. The reduction methods include passage of H_2 gas over the CNT-$PtCl_6$ at a high temperature (typically 80^{o}C), or slow addition of reducing agent such as NaOH or $NaBH_4$ resulting in the reduction of the platinum salt. In the surfactant-stabilized methods and EG methods, the reacting mixture is placed in a heating bath at a high temperature of 90 ^{o}C and 140 ^{o}C respectively, and the solvent in these cases acts as the reducing agent as they break down at these high temperatures to form compounds capable of reducing the Pt salt.

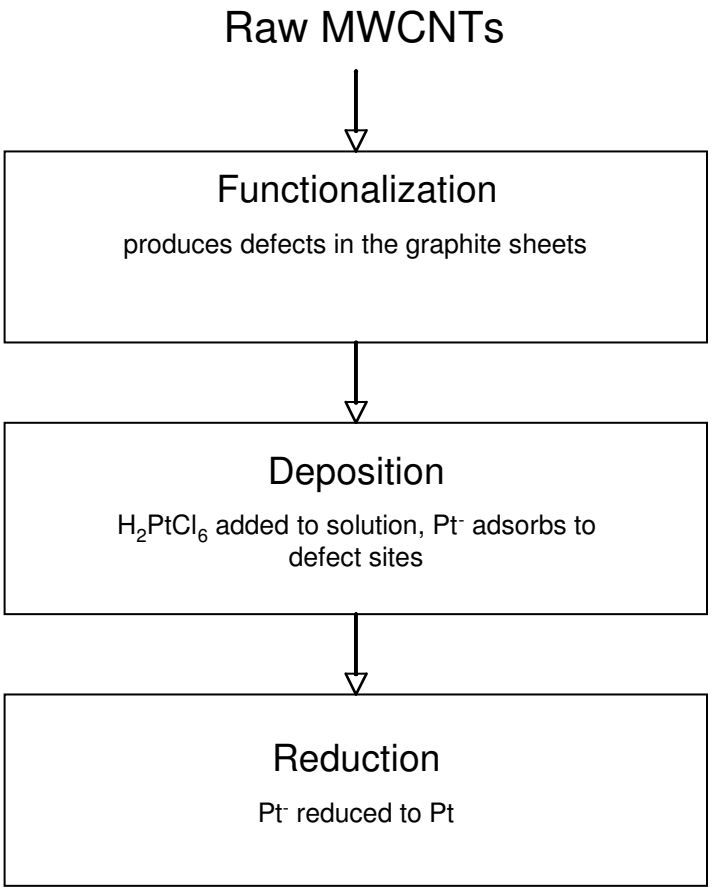

Figure 21 : Scheme for synthesis of Pt/CNT catalysts

3.2.1.1 Material

Multiwall carbon nanotubes from Microtech Nano (USA) were used. MWCNTs had diameters of 40-60 nm and lengths of 1-15 μm. The platinum precursor used was H_2PtCl_6 (Alfa Aesar) of specification 99% metal basis. For the CNT functionalization step, the MWCNTs were mixed in 98% H_2SO_4 and 70% HNO_3 - both obtained from Fischer Scientific Canada. The electrochemical kinetic measurements were completed using 0.1M Perchloric acid obtained from Fluka Chemical Company,USA, as an electrolyte. The oxygen gas blanketing the electrolyte in electrochemical measurements of ultra high purity, >99.999% from Praxair, Canada, was used.

For fuel cell testing, gas diffusion layers (SGL_10BB) from E-TEK were employed. A half MEA (one side of membrane pre-coated with 0.3 mg_{Pt}/cm^2 Pt/C catalyst layer) from Ion Power (USA) were used. The fabricated catalyst loading of the catalyst layer was 0.2 mg_{Pt}/cm^2.

3.2.1.2 CNT Functionalization

The objective of CNT functionalization is to introduce oxygen-containing functional groups on the CNT surface. For functionalization or surface oxidation, MWCNTs were mixed with a 1:1 mixture of 98% H_2SO_4 and 70% HNO_3. Approximately 100 mg of CNT were added to 10 mL of the acid mixture in a round bottom flask and sealed. The mixture was allowed to react for 24 hours at ambient conditions. The CNTs were then filtered, followed by rinsing with de-ionized water and acetone, and, finally, dried at room temperature.

3.2.1.3 Platinum deposition on CNT

Precipitation Method

For the precipitation method, functionalized MWCNTs were added to water and sonicated to obtain a well dispersed solution/suspension. H_2PtCl_6 (Alfa Aesar) was added to the CNT solution/suspension in order to achieve approximately a 15wt% Pt on CNTs catalyst assuming all the Pt adsorbs onto the CNTs. The solution was stirred magnetically at room temperature for 24 hours. The $PtCl_6$ adsorbed onto the CNTs was reduced to Pt by slow drop wise addition a 0.1/1 M solution of $NaBH_4$/NaOH. The reacting mixture turned yellow indicating onset of reaction and upon completion of reduction it turned clear. The solution/suspension was then filtered and rinsed again with de-ionized water and acetone. The CNT-Pt catalyst was allowed to dry at room temperature.

Colloidal Method

In this method, the functionalized CNTs were added to a known amount of EG (Sigma-Aldrich), approximately 80 mg of CNT in 22 mL of EG, and sonicated/magnetically mixed until a well

dispersed solution is obtained. The H_2PtCl_6 is dissolved in sufficient water to attain 20% of the total liquid volume. The amount of H_2PtCl_6 added to the solution upon complete deposition would result in a 15 wt% Pt on CNTs. To study the effect of pH on the Pt size, after addition of the H_2PtCl_6 solution, the pH of the mixture was adjusted to the desired value by addition of NaOH in a 20 vol% water/EG mixture. Next, the solution was placed in an oil bath at 140^{o}C for approximately 3 hours until the reaction was completed. The pH was monitored during this period and maintained at the desired level by further addition of the NaOH solution. The level of the solution in the beaker was maintained by addition of a 20% water/EG mixture. Once the pH was no longer changing, the CNTs were filtered and rinsed with de-ionized water and acetone and allowed to dry at room temperature.

3.2.1.4 Preparation of RDE Electrode

The electrode was prepared for catalyst deposition by first polishing with 1 μm alumina powder, followed by washing with D.I. water and subsequently sonication for 10 minutes. The catalyst suspension was separately prepared based on standard methods [50]. Approximately 20 mg of Pt/CNT were suspended in a 10 mL solution of iso-propanol, water and 5 wt% Nafion solution. The suspensions were sonicated for 30 minutes prior to deposition. In some cases, when the suspension did not disperse well it was further mixed mechanically by placing a magnetic stirring bar in the sample and placing it on a mixing plate. The suspension was deemed to be well mixed when it appeared to contain no solids upon visual inspection. The catalyst suspension (ink) was deposited in 5 μL droplets onto surface of glassy carbon using a micro-syringe and was allowed to dry overnight at room temperature. A total of volume of 30 μL of the catalyst ink solution was deposited onto the electrode and was left open to the surrounding air for drying.

3.2.1.5 Preparation of Pt/CNT Electrodes For Fuel Cell Testing

A catalyst layer consisting of Pt/CNTs catalyst, Nafion® solution and iso-propanol was applied on the gas diffusion layer. An airbrush was used for catalyst application. The electrode was dried in an oven at 90°C for 2 h. A conventional preparation method was used to determine the ratio of the various components in the MEA [61]. The ratio of dried Nafion® to Pt/C was 1:3 by weight and the Pt loading was 0.2 mg_{Pt}/cm^2. The electrode area was 6.25 cm^2 and typical loadings of Nafion® ionomer in the electrode was in the range of 0.5-0.7 mg/cm^2. After fabrication, the MEA was pressed together with the diffusion layer at 120°C by applying a pressure between 1.4 and 2.0 MPa for 2 min.

3.2.2 Characterization of Physical Properties of Pt/CNT Catalysts

This section contains description of methods employed for characterization of functionalization of CNT as well as characterization of platinum deposited on CNT. The platinum deposited on CNT was characterized for average particle size by X-Ray Dispersion (XRD) and Tunneling Electron Microscopy (TEM). The total surface area of platinum on CNT was determined by an electrochemical method via estimation of charge associated with hydrogen desorption on Pt as determined by cyclic voltammetry.

3.2.2.1 CNT Functionalization

The functionalization of CNT was examined by analysis of functional groups determined by X-Ray Photoelectron Spectroscopy (XPS). These measurements were performed at the XPS facility at the Department of Chemistry, Queen's University by Amit Rudrake, a graduate of the chemical engineering department.

3.2.2.2 Physical Characterization of Deposited Platinum Size

Pt loading on CNT

The loading of the Pt on CNT was determined by the evaluation of the platinum remaining in the filtrate of the deposition experiments as determined by atomic adsorption (AA). All platinum not remaining in the filtrate solution is assumed to be deposited on the CNTs. These experiments were carried out at Royal Military College by Bob Whitehead.

Pt size analysis by XRD

The powder CNT/Pt XRD samples were analyzed by a Scintag (Thermo/ARL) X1 unit by Bob Whitehead at the Royal Military College of Canada (RMC). The sample scan began at an angle of 20^{o} and was carried through to 130^{o}. A sample of the XRD plot obtained for a CNT/Pt catalyst is seen below in Figure 22. The peak fitting analysis was completed by employing the Scintag software associated with the XRD unit. This software is able to provide the average crystal size associated with each peak. The location of peak expected for a given element is constant and thus the average size of each element present can be obtained.

Pt size by TEM

The TEM samples were prepared by mixing the synthesized CNT/Pt samples in methanol and depositing the suspension by micro-syringe onto copper grids. A small volume, approximately 5 μL, of the sample was deposited in order to insure that a thin sample is created. The samples were analyzed in a Philips CM20 TEM apparatus at Queen's University by Alison Mark, a graduate student of the department of Mechanical and Materials Engineering.

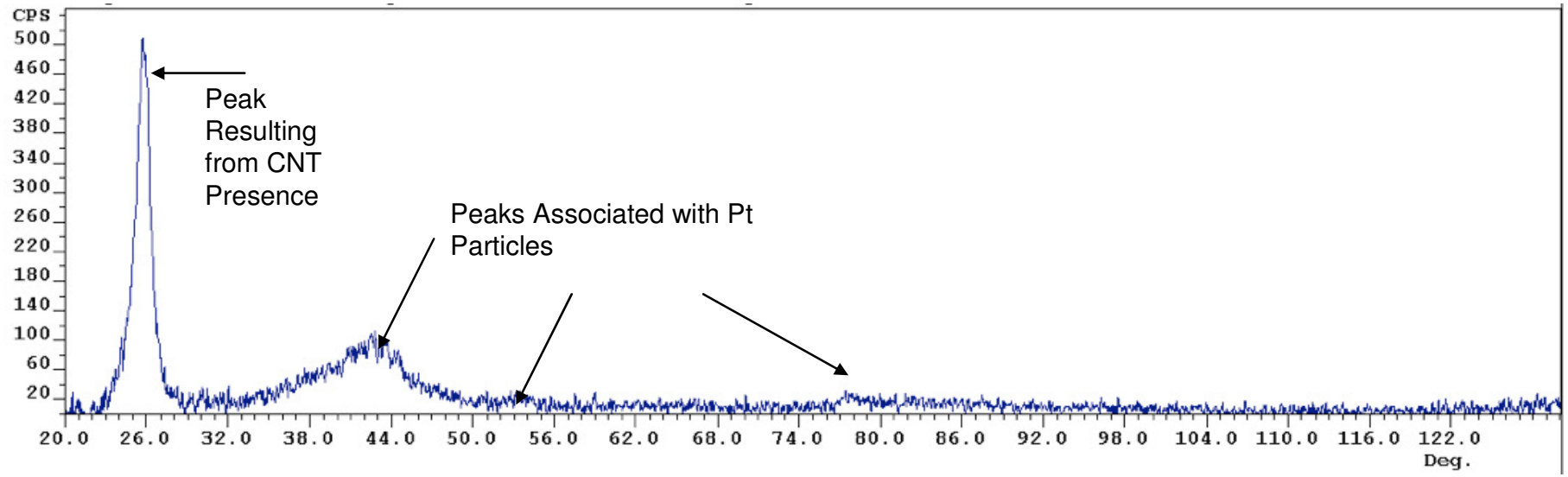

Figure 22: Sample XRD for Platinum on CNTs: Area Under Indicated Peaks Used to Determine Particle Size Based on Scherrer Equation

3.2.2.3 Pt Surface Area by Hydrogen Adsorption/Desorption Cyclic Voltammetry

Theoretical Background

Cyclic voltammetry is an electrochemical method that allows determination of the real surface area of noble metal catalysts such as Platinum by measuring the coulombic charge associated with the deposition or removal of a chemisorbed monolayer of a species, usually hydrogen. For hydrogen, 210 micro coulombs of charge correspond to coverage of $1cm^2$ of Pt area. When platinum electrode (electro-catalyst) is exposed to an aqueous acidic medium (electrolyte), the hydrated proton discharges with the formation of electro-adsorbed hydrogen according to the following reaction:

$$M\,(Pt) + H^+ + e^- \leftrightarrow M - H_{ads} \qquad \textbf{(3-15)}$$

By altering the potential of the electrode, the reaction can be affected in the forward or reverse direction. In cyclic voltammetry, the electrode potential is cycled between two potentials and the current is measured. A plot of current versus electrode potential is recorded; a typical voltammogram is shown in Figure 23.

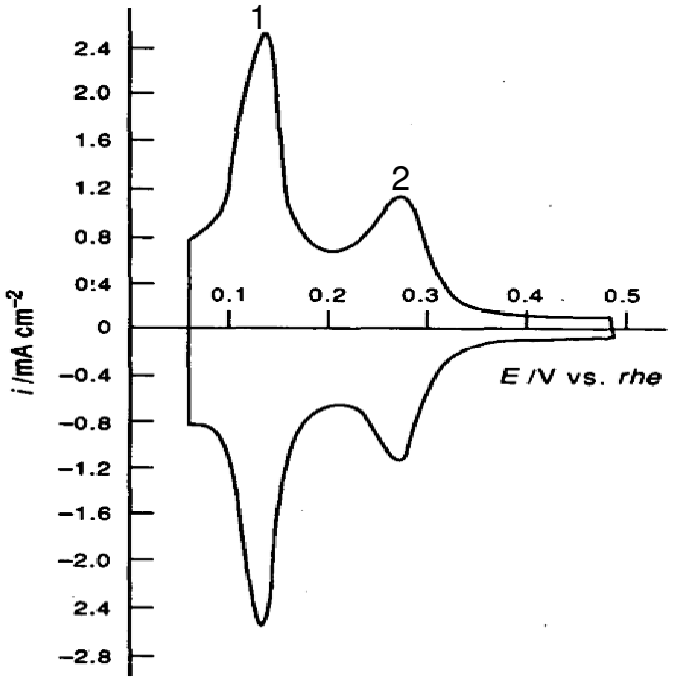

Figure 23: Typical cyclic voltammogram for platinum exposed to acidic electrolyte

There are 2 main states of hydrogen adsorption that may be seen in a platinum CV. Moving in the anodic sweep direction (from zero to 0.45V), the reaction (3-15) proceeds in the reverse direction indicating the oxidation of adsorbed hydrogen, i.e hydrogen desorption. Peak number 1 is associated with the strongly adsorbed hydrogen while peak number 2 is associated with the weakly adsorbed hydrogen. The charge associated with area under both peaks is used to determine the active area of the platinum. The charge can be calculated by integrating the current versus time data over the 0 to 0.45 V range. The adsorption and desorption of hydrogen should be symmetrical however in practice a charge is created by carbon in the cathodic sweep direction (hydrogen adsorption) which makes the area calculated for platinum on carbon catalysts unrealistically high if the adsorption peak is used [62]. Thus the desorption curve is typically used for these type of catalysts.

One of the key issues involved in determining the area by cyclic voltammetry is the use of a baseline to use as a reference in determining what area under the peak should be included. The baseline should be selected such that it represents the electrode when no platinum is present, so that the reaction of interest is not occurring. Then any changes in the shape of the curve can be attributed to the platinum. In this case the functionalized CNTs should be used as a baseline. In theory this seems simple enough however each batch of CNTs has slightly different properties resulting in different areas and therefore produce different current as shown below in Figure 24. The shape of the curve however is consistent and will be scaled for each catalyst examined. This is done by expanding the base curve shape to fit the curve obtained for the Pt/CNT catalyst. By this method, a baseline is created that can be used to evaluate the area under the hydrogen adsorption peak.

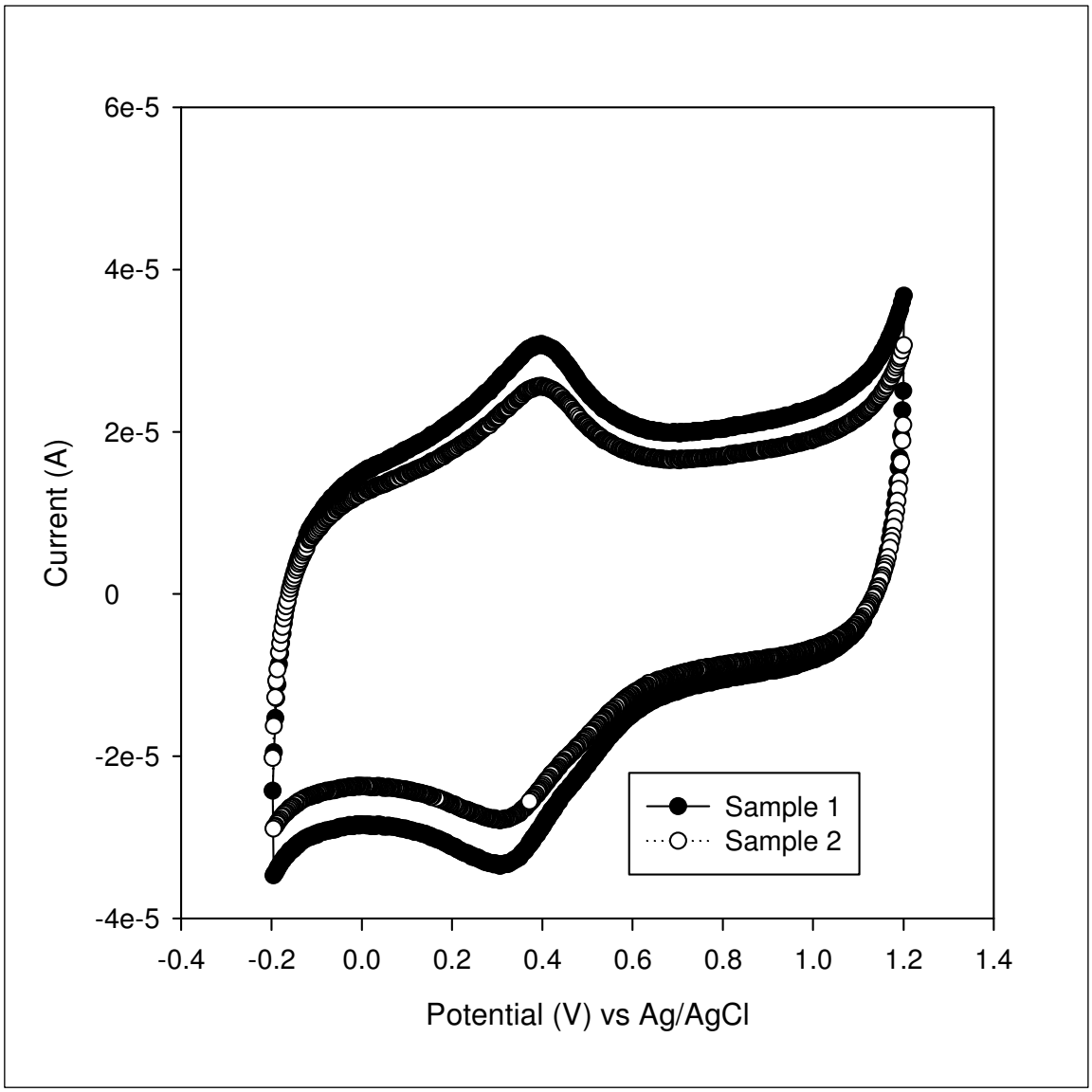

Figure 24: Cyclic voltammetry of bare CNT. Run at 25°C and 101.3 kPa in $HClO_4$ electrolyte saturated with Ar, 20 mV/s scan rate.

Experimental Description

The cyclic voltammetry experiments were carried out in a three-electrode glass cell setup shown in the Figure 19. A 0.1M perchloric acid solution (Fluka Chemical Company) gassed with pure argon served as a supporting electrolyte. The working electrode was mounted on a shaft of rotating disk electrode system BASi-2 RDE. The reference electrode was a Ag/AgCl electrode in

a 3M NaCl solution separated from working electrode compartment using a porous glass filter and salt bridge filled with supporting electrolyte. A platinum wire served as the counter electrode.

The Pt catalysts to be subjected to CV were applied on the working electrode, which was a glassy carbon disc with a 0.07 cm^2 area encased in a plastic ring outfit.

The catalyst-coated working electrode was placed in the RDE system at room temperature (24^oC), and the electrolyte (0.5M H_2SO_4) was purged with argon for 20 minutes. The argon was then switched into a blanketing position, in this position the argon no longer bubbles vigorously through the electrolyte but passes over the electrolyte solution to insure no air enters the system. The potential was swept from -0.2 to 1.2 V vs Ag/AgCl electrode at 20 mV/sec and the current was recorded. The cycling continued for 500 cycles which is equivalent to 9.72 hours and the stability of the response was evaluated by comparing the curve after 500 cycles to the curve when it first became stable.

The cyclic voltammetry plot results in an active area in units of m^2 and in order to obtain the desired units m^2/g_{pt}, to compare with literature values, the mass of platinum loaded onto the electrode must be known. In the deposition experiments a measured amount of H_2PtCl_6 is added to a known value of CNTs. It was assumed that all Pt present in the experiment was deposited onto the CNTs in elemental form. This assumption was verified by running *atomic adsorption* (AA) spectrometry on the filtrate of the experiment. A platinum standard was used to calibrate the AA unit and the level of platinum in the filtrate was so low that it was undetectable. This is visually apparent as well with the platinum filtrate being a clear colour rather than tinted yellow colour prior to the deposition experiment. These experiments were carried out at RMC.

3.2.3 Electrochemical KineticCharacterization of Pt/CNT Catalysts

Brief theory of electrochemical kinetics

One of the objectives of this thesis is to characterize the Pt/CNT catalyst for their electrochemical performance of the oxygen reduction reaction. An electrode (Pt) in contact with an electrolyte (ion conductor) saturated with reactant (oxygen) develops an equilibrium potential difference between the electrode (electron conducting) and electrolyte (ion conducting) phases when no net current flows. For conditions of net current flow and under conditions where no mass transport and ohmic losses exist, the electrode-electrolyte potential difference is altered from the equilibrium potential by a certain amount called the 'activation overpotential'. The activation overpotential is the difference above the equilibrium value required to produce a current. A generalized relationship between current and overpotential is given by the Butler-Volmer equation:

$$I = A \cdot i_o \left[\exp\left\{ \frac{(1-\alpha) n \cdot F}{R \cdot T} (E - E_{eq}) \right\} - \exp\left\{ \frac{-\alpha \cdot n \cdot F}{R \cdot T} (E - E_{eq}) \right\} \right] \qquad \textbf{(3-16)}$$

where, I is the electrode current, A is the active surface area of the electrode, i_o is the exchange current density, E is the electrode potential, E_{eq} is the equilibrium potential, α is the symmetry factor, F is the Faraday constant (=96485 Coulombs/mol); R is the universal gas constant, T is the system temperature, and *n* is the number of electrons involved in the reaction.

At higher overpotential, the second term on the RHS becomes insignificant compared to the first term, under such conditions, the so-called Tafel approximation can be applied and the resulting equation can be rearranged the following equation, commonly referred to as the Tafel equation:

$$\eta_{act} = B \ln\left(\frac{i}{i_o} \right) \qquad \textbf{(3-17)}$$

where, η_{act} is the activation overpotential (in Volts), B is the Tafel Slope, and i is the current density (in A/cm^2)

The exchange current density, i_o, is the equilibrium current which describes the rate at which both oxidized and reduce species react at the electrode. It can be thought of as the electrochemical reaction rate constant. A larger exchange current density indicates that the reaction catalyst surface is more active and a current is likely to flow in the forward reaction direction. Since this exchange current density is controlling the rate of the sluggish ORR and ultimately the fuel cell performance it is important to make it as high as possible. The constant B (also known as the Tafel slope) is given by:

$$B = \frac{RT}{2\alpha F} \qquad \textbf{(3-18)}$$

In the above equation the charge transfer coefficient, α, depends on the reaction that is occurring.

When examining the exchange current density in the region limited by the kinetics the ORR can be examined. For oxygen reduction the kinetic current for the mixed activation-diffusion controlled area, where the current is a product of both kinetic and diffusion contributions can be calculated as follows:

$$\frac{1}{i} = \frac{1}{i_k} + \frac{1}{i_L} \qquad \textbf{(3-19)}$$

$$i_k = \frac{i \cdot i_L}{i_L - i}$$

The diffusion limited current can be found from the polarization curve and used to convert the total current to kinetic current for the kinetically controlled region of the curve as seen below in Figure 25. This kinetic current can then be used in the Tafel equation to create a plot of log (i_K) vs. potential. From the Tafel equation the exchange current and Tafel slopes can then be determined to evaluate the kinetics of the catalyst being examined.

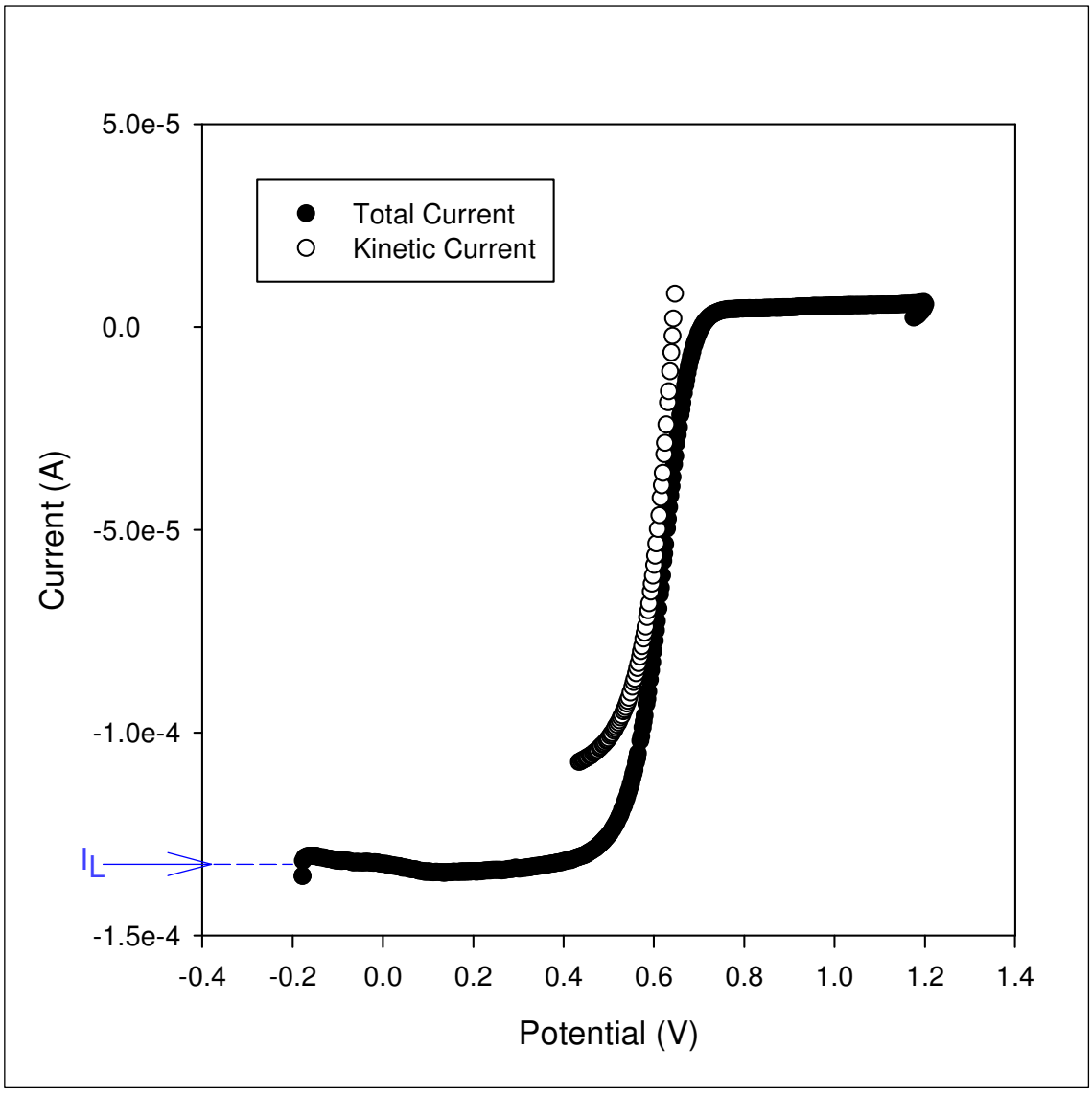

Figure 25 : Illustration of polarization curve corrected to obtain kinetic current in activation controlled region

3.2.4 Experimental Procedure for ORR Kinetics Measurements

The Basi-2 RDE experimental set-up seen above in Figure 19 was used for the kinetic studies of novel catalysts. The electrolyte (0.1M perchloric acid, Fluka Chemicals) at room temperature (24^{o}C) and at atmospheric pressure was saturated with ultra high purity oxygen for 20 minutes. The glassy carbon working electrode, prepared for cyclic voltammetric evaluation of the catalyst, was placed in the electrolyte and rotated at 1600 rpm. The potential was swept from -0.2 to 1.2 V vs Ag/AgCl electrode at which point a stable response is obtained. The curve is then fitted to the Butler-Volmer equation as described above to obtain the Tafel slope and exchange current density.

3.2.5 Experimental Procedure for Fuel Cell Testing of Pt/CNT Catalyst

Currently the major losses in fuel cell performance arise from the cathode side of the membrane thus the CNT/Pt membranes prepared for fuel cell testing were prepared for the cathode. A catalyst layer consisting of Pt/CNTs catalyst, Nafion® solution and iso-propanol was applied on the gas diffusion layer. An airbrush gun was used for catalyst application. The electrode was dried in an oven at 90 °C for 2 h. The ratio of dry Nafion® to Pt/C was 1:3 by weight and the Pt loading was 0.20 mg/cm^2. The electrode area was 6.25 cm^2 and typical loading of Nafion® ionomer in the electrode was in the range of 0.5–0.7 mg/cm^2. The anode was Ion-power catalyst coated membrane with a Pt loading of 0.3 mg/cm^2. After fabrication, the MEA was pressed together with gas diffusion layer at anode side at 120 °C, between 200-300 psi, for 2 min.

Polarization curve experiments were carried out a single fuel cell test station (Hydrogenics FCATS-S800, Canada). The cell temperature was held at 60 °C by heating the endplates. The cell was fed with air on the cathode side (Praxair, Inc.) and pure hydrogen on the anode (MEGS Specialty Gases, Inc.). The flow rate varied according to current density to maintain

stoichiometric ratios of 1.4 for hydrogen and 3.5 for air. The relative humidity of the feed gas streams were set to 100%. Both the anode and cathode gas back pressure was set to 35 kPa. In situ cyclic voltammograms were measured at a scan rate of 50 mV/s by supplying N_2 to the cathode side (serving as working electrode) and H_2 to the anode side (serving as counter and reference electrode). MEA fabrication and fuel cell testing was carried out by Dr. Madhu Saha, a post-doctoral fellow at the FCRC.

Chapter 4
Results and Discussion

The results and analysis of the experimental work is presented in two parts. The first part (section 4.1) discusses the results of the measurements of oxygen permeability in ionomer-carbon films. The second part (section 4.2) presents the results for the Pt/CNT catalysts characterization.

4.1 Oxygen Permeability in Nafion®-Carbon Films

4.1.1 Raw Data

For permeability measurement the raw data collected is the polarization curve from the RDE experiments, as per the method described in section 3.1.3. Example polarization data for various rotational speeds for an ionomer-carbon film with 1.9 vol% carbon content is shown in Figure 26 below.

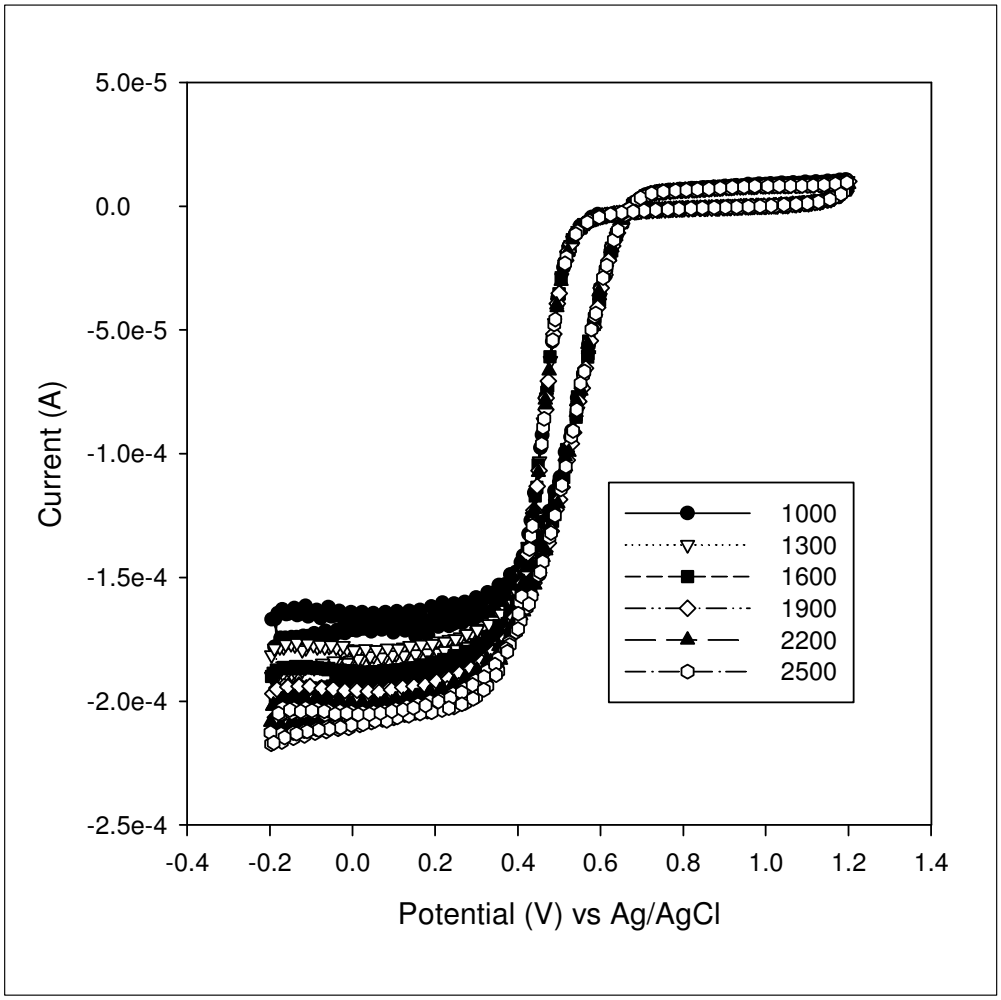

Figure 26: Polarization data from RDE experiments for ionomer-carbon film with 1.9 vol% carbon content. Run at 25°C and 101.3 kPa in $HClO_4$ electrolyte saturated with O_2, 20 mV/s scan rate.

The limiting currents at each rotational speed are obtained at -0.2V and a Levich plot (limiting current vs $\omega^{-1/2}$) based on these values was created. The linearity of the plot allows the applicability of the modified Levich equation.

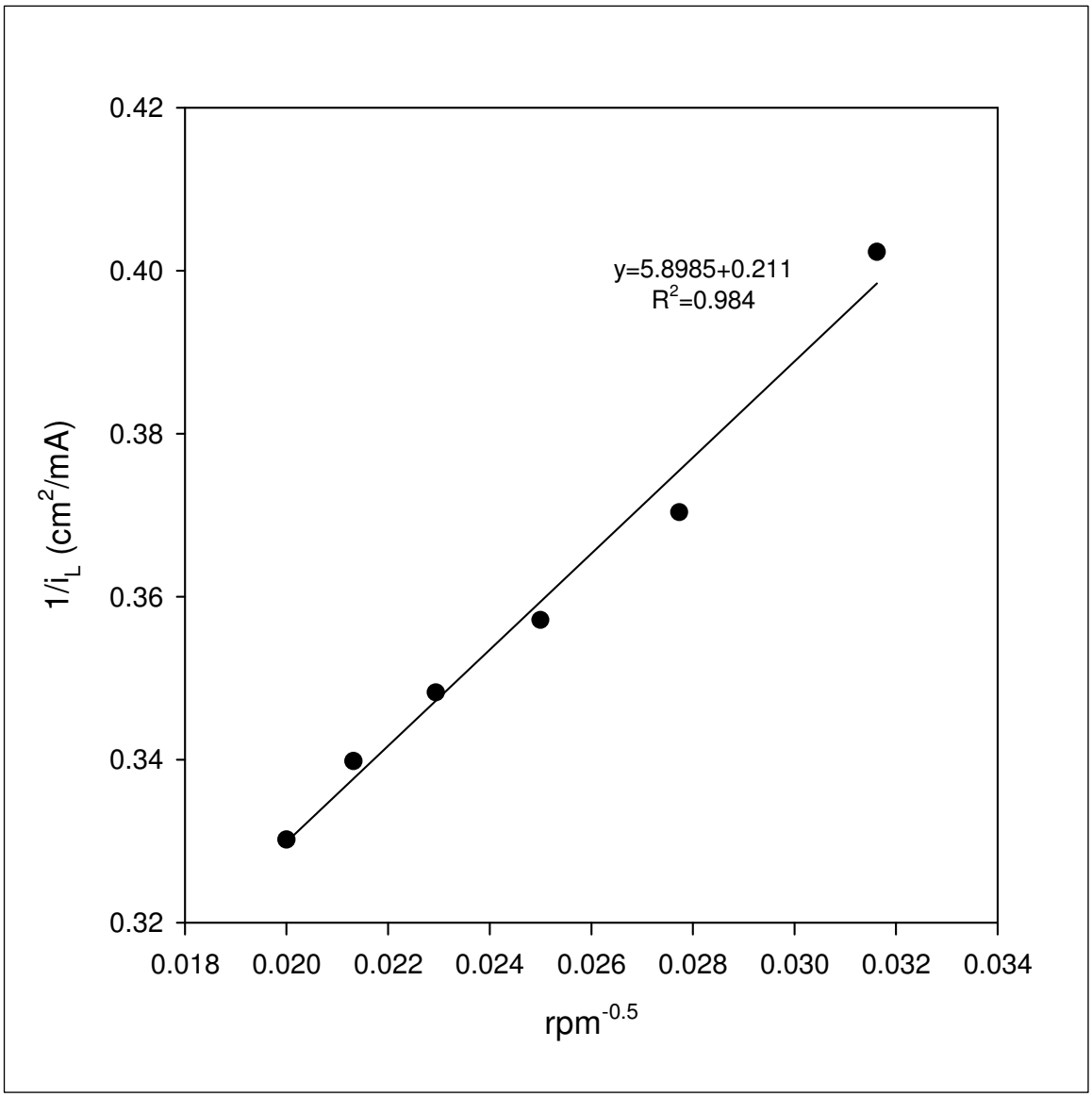

Figure 27: Levich plot for 1.9vol% carbon:ionomer film

4.1.2 Oxygen permeability analysis based on estimated film thickness

4.1.2.1 Pure Nafion® Film

Experiments were carried out with pure Nafion® films, i.e. zero carbon content, of varying thicknesses. The thicknesses were calculated assuming the film was dense. The results are presented in Figure 28.

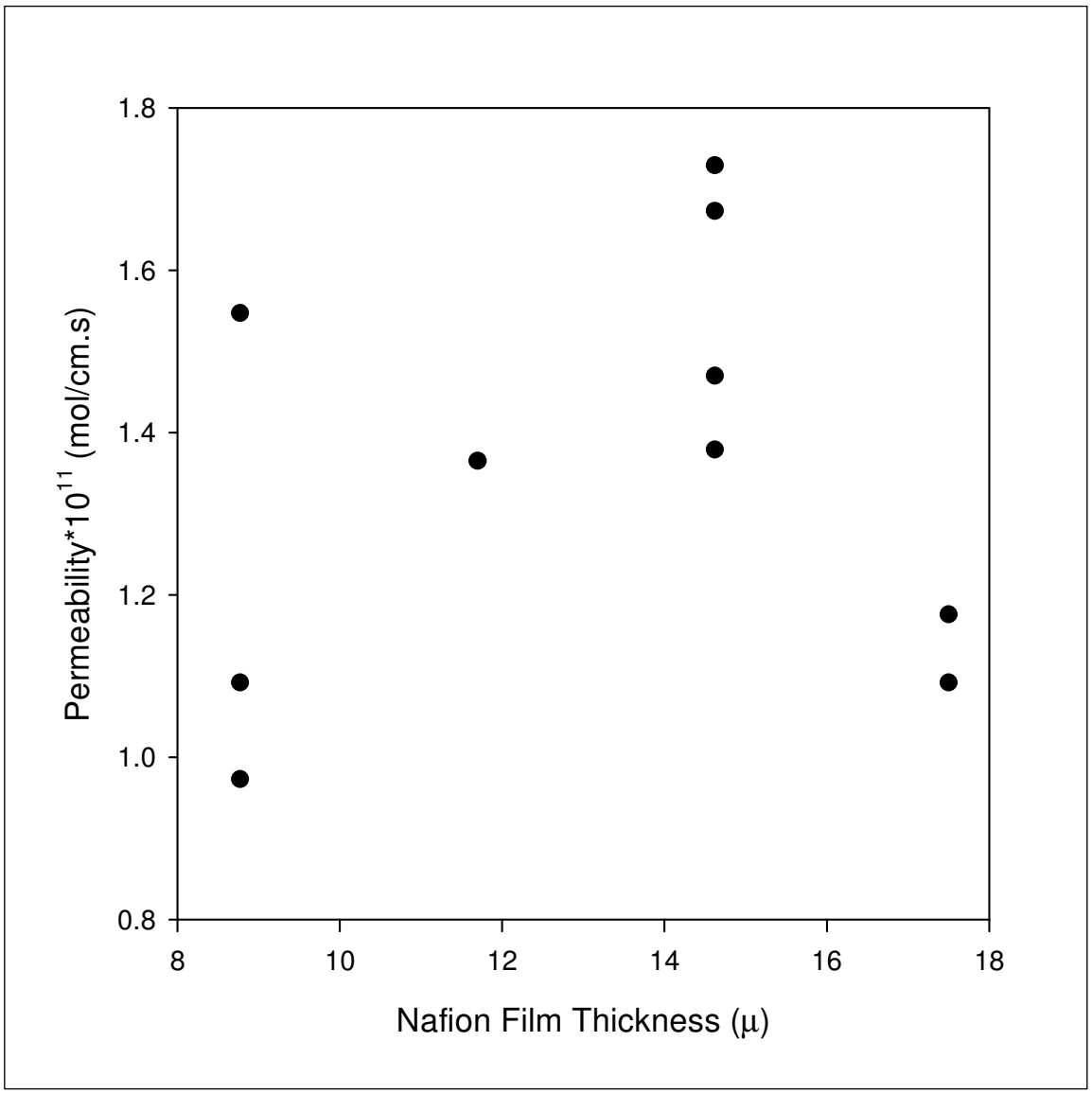

Figure 28: Permeability of Oxygen Through Nafion® Films of Various Thicknesses (Dense Film)

A significant amount of scatter can be observed from the data which masks any trend between oxygen permeability and film thickness. In order to examine this relationship in more detail a statistical analysis of a linear relationship between thickness and permeability was examined in JMP. The statistical parameters of interest are found below:

Table 1: Statistical Parameters for Nafion® Permeability vs. Thickness Fit

Parameter	**Value**
R^2	0.024925
R^2 adjusted	-0.0972
F ratio	0.2027
t-ratio intercept	0.6645
t-ratio slope	0.0104
Mean Permeability	1.35×10^{-11} mol/cm.s

Both the R^2 and R^2 adjusted value are very low which support the hypothesis that no relationship exists between the permeability of oxygen in Nafion and the film thickness. The MSR/MSE ratio (F ratio) also supports the conclusion that this is an inadequate model even at a low 75% confidence region. Finally both the intercept and thickness parameter are statistically insignificant. Based on the quantitative diagnosis it can be concluded that no statistically significant correlation between permeability and film thickness exists. An average value of permeability equal to 1.35×10^{-11} mol/cm-s can be derived from the set of data.

4.1.2.2 Ionomer-Carbon Film

Experiments were carried out for various ionomer-carbon films with 'nominal' carbon volume fraction varying from 0 to 11%. In these experiments, the ionomer was Nafion® and the carbon was Vulcan XC72. The underlying theory and relevant equations have been discussed in section

3.1.2. Accordingly, the measured limiting current can be expressed in terms of two unknowns - film thickness and permeability (product of concentration and diffusivity) as follows:

$$\frac{1}{i_{lc}} = \frac{1}{0.62nFAD_o^{2/3}\omega^{1/2}\nu^{-1/6}C_o^*} + \frac{\delta_f}{nFAD_f\kappa C_o^*} \quad \textbf{(4-1)}$$

The film thickness, assuming a dense film, was estimated from overall composition and the densities of Nafion® and carbon of 1.58 and 2.25 g/cm3, respectively. The overall permeabilities were subsequently calculated as a function of the volume fraction of carbon in the film and are presented below in Figure 29.

The overall trend shows a decrease in Nafion® permeability as the amount of carbon in films increases. This trend is expected since it is hypothesized that carbon will block the diffusion path of oxygen through the Nafion® causing the permeability to be lower at higher carbon loadings.

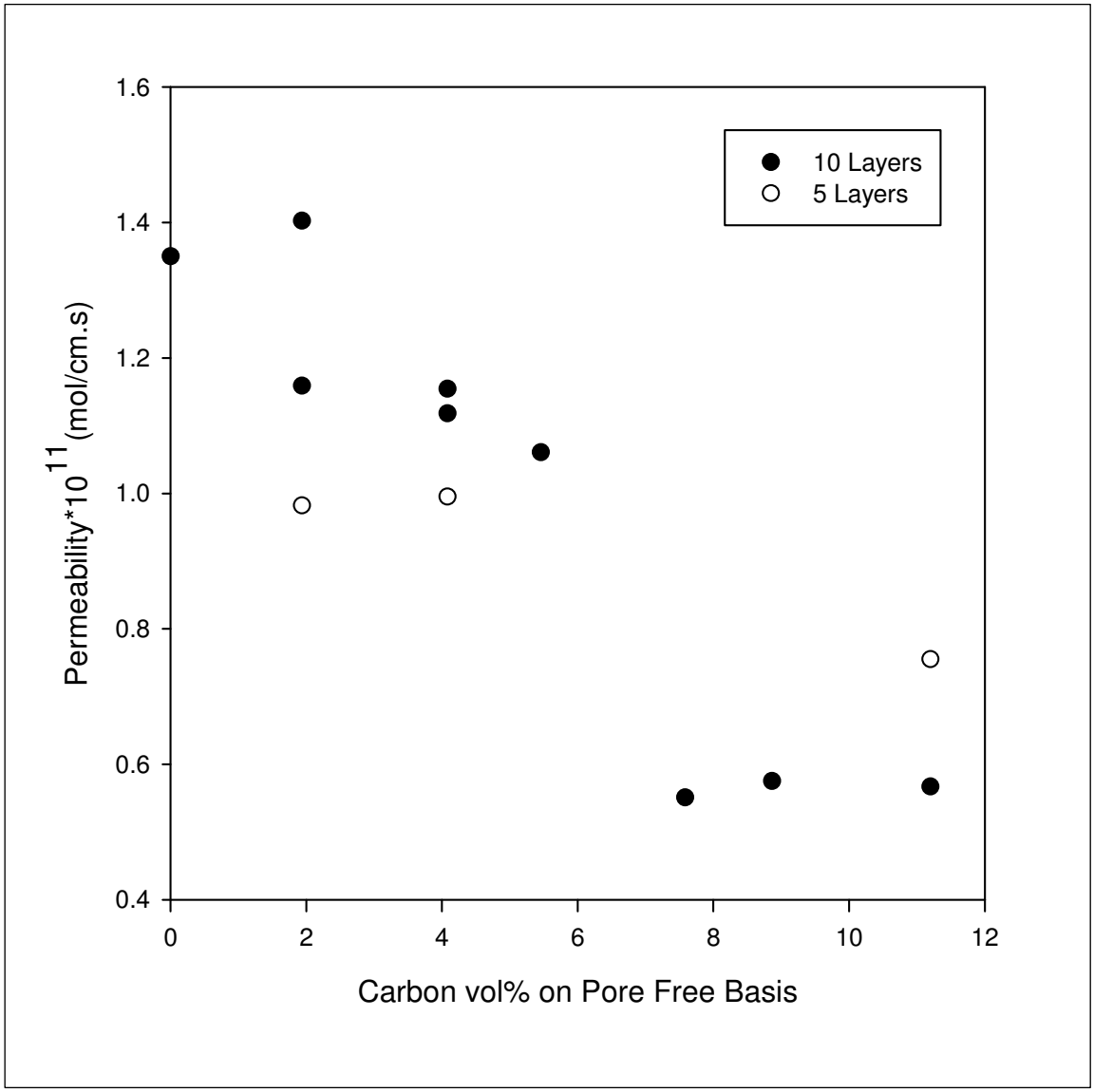

Figure 29: Oxygen Permeability in Ionomer-Carbon Films as a Function of Carbon Content of the Film

The thickness of the film has a major impact on the calculated permeability. By visual inspection it appeared that films were not of even thickness. It was also hypothesized that the films were porous in nature which would make the thickness estimation based on solid densities inaccurate. As a result measurements of film thickness were of great interest.

4.1.3 Characterization of film

The assumption that the films of Nafion®-carbon may not be dense was not questioned until a late stage of the thesis work. This was due both to unavailability of tools to measure very small thicknesses (in the order of a few microns) and to the fact that the calculated permeability followed the expected trends with respect to carbon content. At a late stage of the thesis, film profile was quantified using laser-based optical method described in section 3.1.3.4 and both the thickness and the porosity of the prepared films was estimated. The analysis methods and results are presented in the following subsections.

4.1.3.1 Topology of film

A sample three-dimensional topography of a prepared film is shown in Figure 30. The variability of the thickness at a single cross-section is presented in Figure 31.

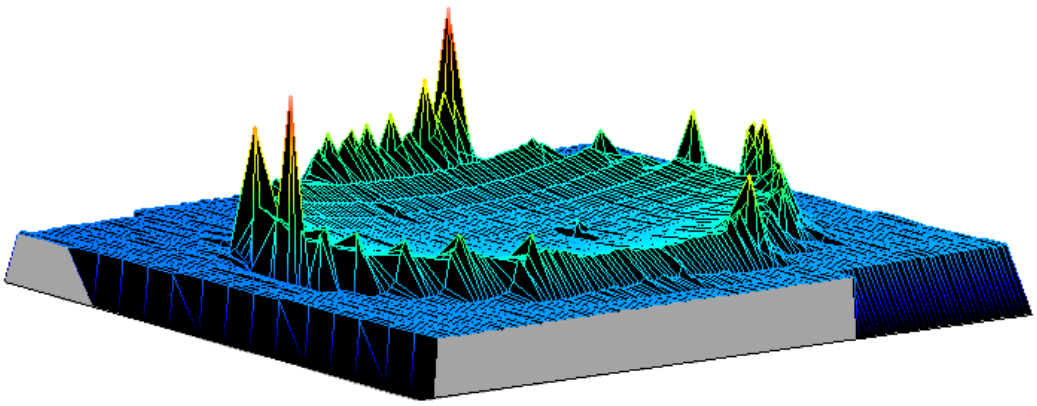

Figure 30: Three-dimensional profile of the ionomer-carbon film containing 1.9 vol% carbon

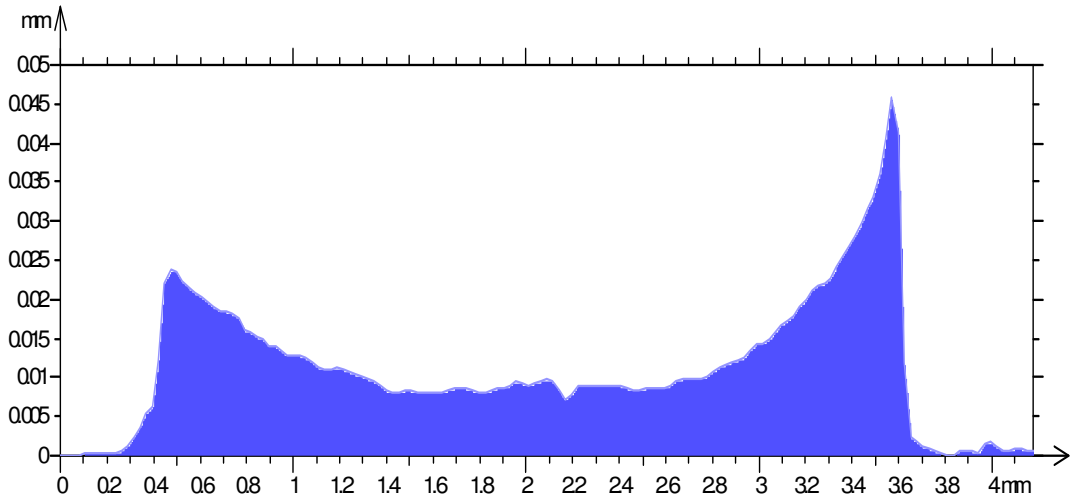

Figure 31: Thickness profile of Nafion® film containing 1.9 vol % Carbon

From Figure 30 and Figure 31, it is clear that film thickness is non-uniform and that the edges of the film are much thicker than the center.

Implications of Non-Uniform Film Thickness

Physically, the non-uniform film thickness implies that the oxygen would diffuse preferentially through the thinner regions to arrive at the Pt surface rather than the thicker outer region. Since the equations employed in the permeability analysis are based on the assumption of uniform film thickness, the calculated results may appear to introduce significant error. It must be recalled that the films were prepared by placing drops of Nafion®-carbon suspension over the electrode which had an electrical tape with a hole slightly larger than the electrode diameter. Thus, the highest peak edges lie just outside the diameter of the electrode and the oxygen flux through this region of the film is expected to be negligible, if not zero. A majority of the oxygen flux is expected to go through the central region which appears to be slightly more uniform in thickness.

Accordingly, the average thickness of center piece with a diameter equivalent to that of the electrode was employed for permeability calculation. Regardless of the elimination of the edge peaks of the film in estimating thickness, the region which is being used to evaluate the permeability is still an uneven film region. This will affect the results and must be considered in the analysis.

4.1.3.2 Average Film Thickness

The thickness of the central region of film for various film compositions is presented in Figure 32. From the figure, it appears that there is no significant change in the film thickness with carbon content of the film for carbon volume fraction (based on Nafion®-carbon composition only) up to 9%. Since the carbon content in the films is small, a large difference in thickness is not expected. It is also possible that the films are porous and that the increase in carbon content is compensated with a reduction in porosity.

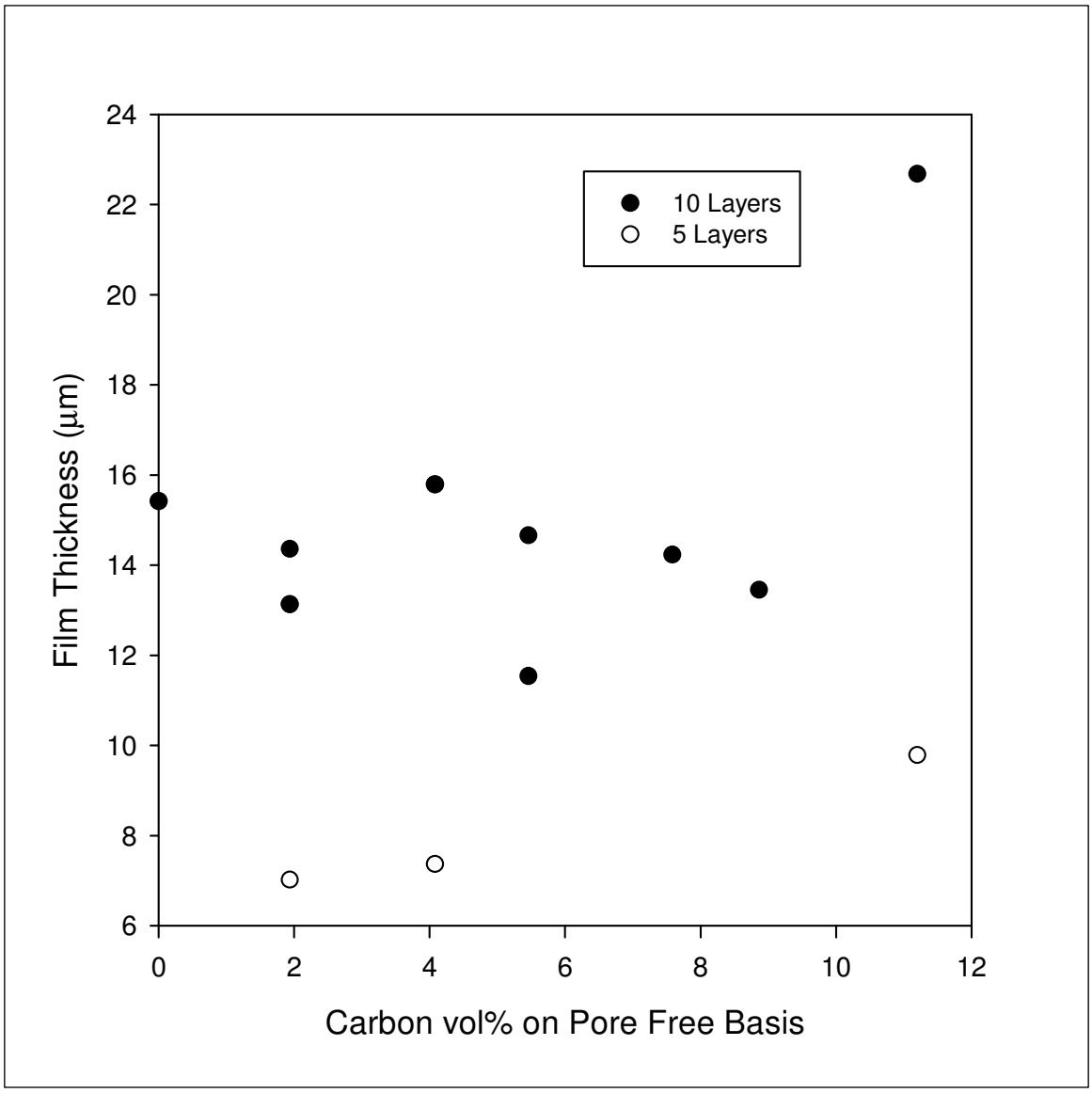

Figure 32: Film thickness as a function of carbon content

The average thicknesses were used to re-estimate the oxygen permeabilities and the re-calculated permeability values are presented in Figure 33 below:

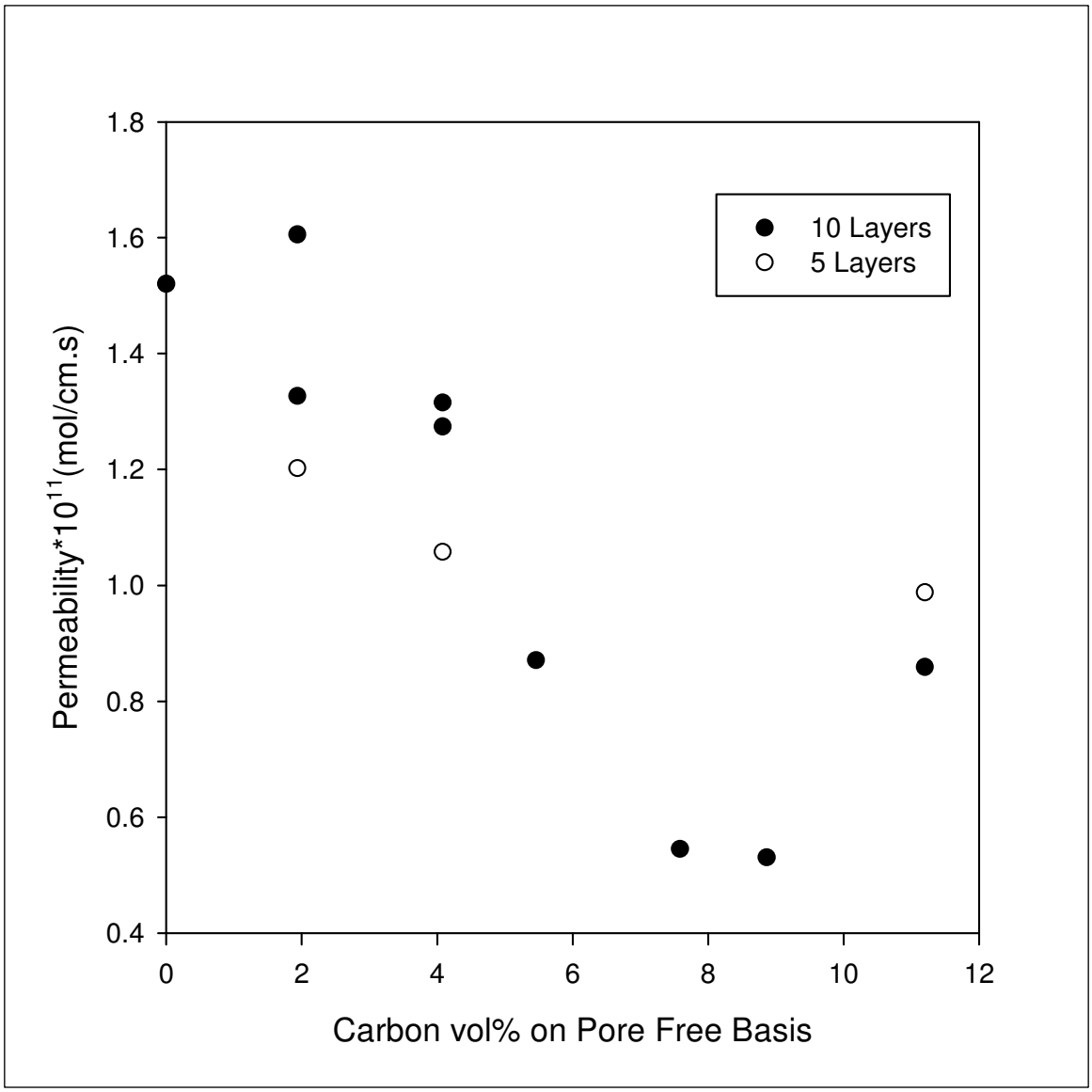

Figure 33: Oxygen permeability as a function of film carbon content.
(Effective permeability calculated from profilometry measured thickness)

From Figure 33 it is visible that there is a decrease in permeability as the amount of carbon in the film increases. As suggested earlier, this may be due to carbon which packs into the pores in the film creating greater resistance to the diffusion of oxygen. Based on the laser obtained thickness,

the permeabilities are determined to be higher than the permeability based on dense thickness. This is due to the higher thickness which is observed by the laser on the OGP. The average Nafion® permeability determined based on the laser OGP thickness is found to be 1.52×10^{11} mol/cm.s.

4.1.3.3 Estimation of Film Porosity

It was suspected that the ionomer-carbon films may be porous in nature. The porosity of the films can be estimated from the actual volume of film and the volume of pore-free, ionomer-carbon material that can be calculated from film composition. The actual film volume was estimated from the film profilometry. An example of the three-dimensional profilometry information for an ionomer-carbon film is presented as a color coded 2D image in the Figure below. By selecting the film region as the calculation domain, the image analysis software yields the cross-section area and the enclosed volume using the lowest height point as the reference height of zero.

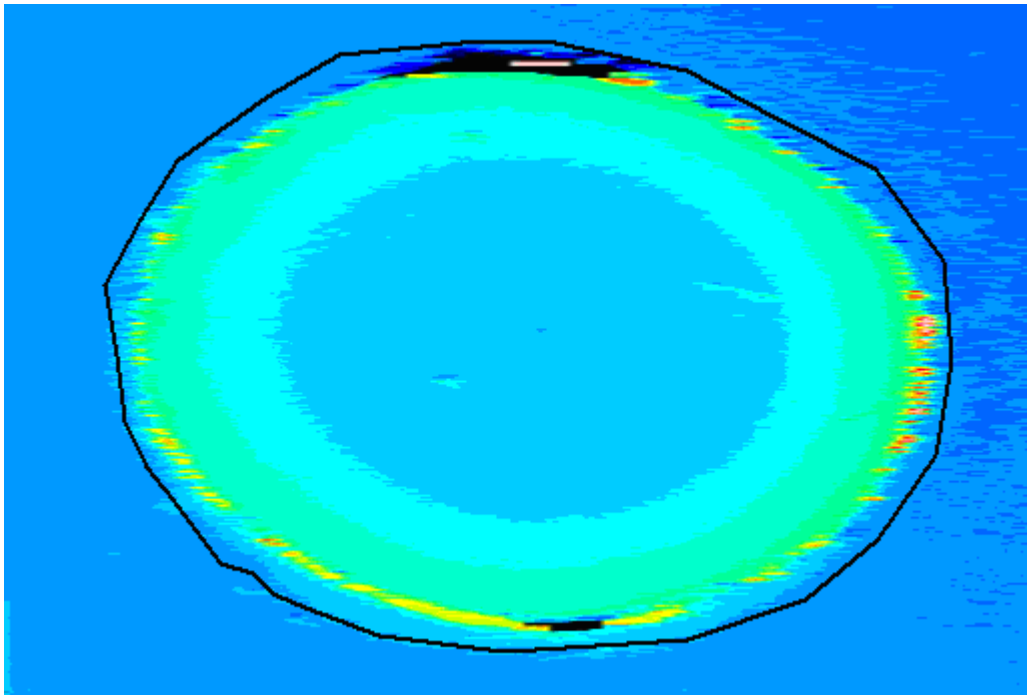

Surface Volume (m^3)	1.82×10^{-10}
Max Depth (m)	0.000158
Mean Depth (m)	0.0000187

Figure 34: 3-D Image of Carbon-Nafion Film Obtained by Optical Guidance Probe (OGP) Laser Used to Determine Film Volume by Using Film Height and Area

The porosity is then readily calculated by the following equation:

$$\varepsilon = 1 - \frac{V_s}{V_f} \qquad (\mathbf{4\text{-}2})$$

where, V_s is the solid or ionomer-carbon volume calculated from the known composition and V_f is the film volume determined from profilometry analysis. The film porosity as a function of carbon content is presented in the Figure 35 below.

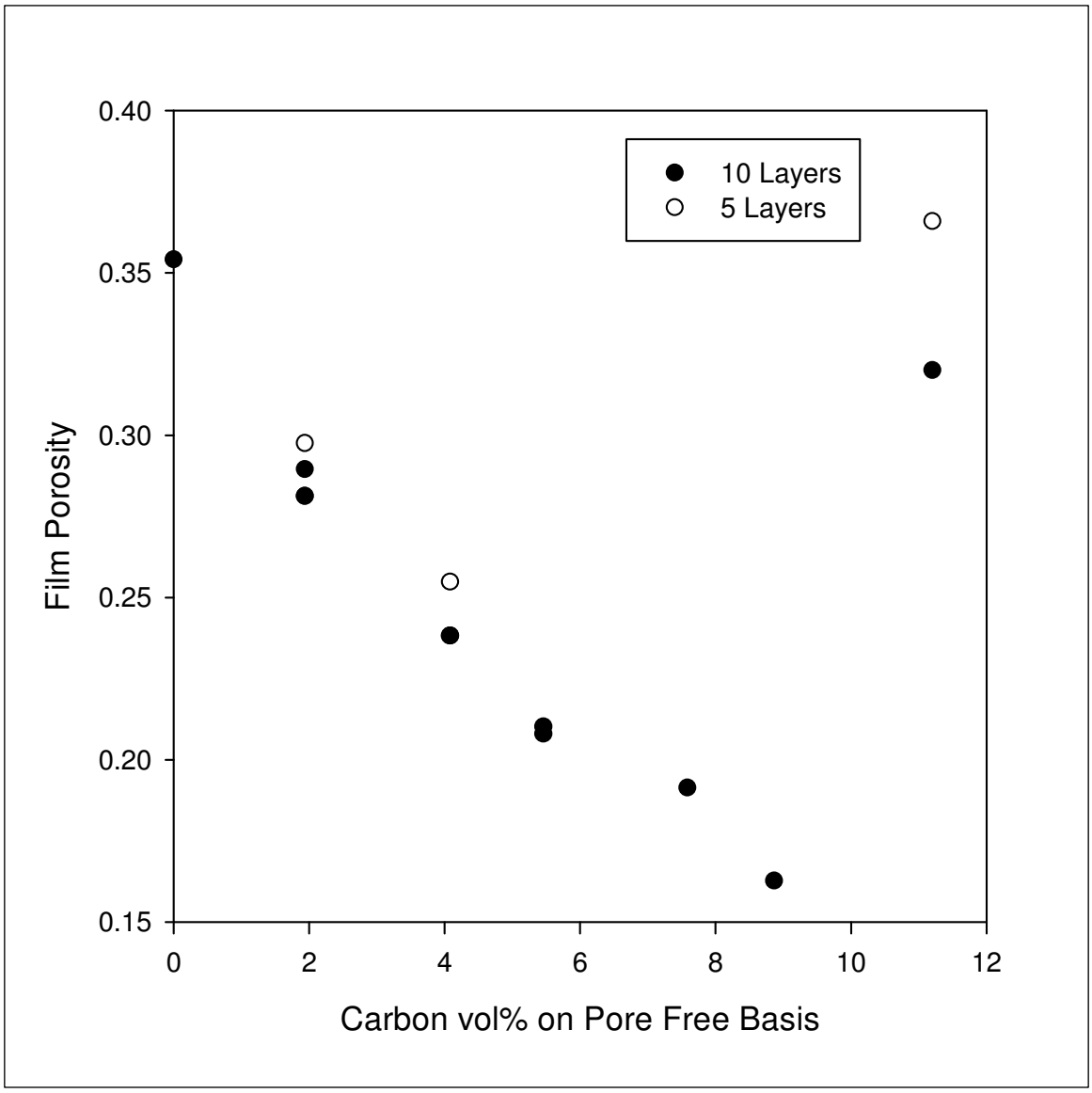

Figure 35: Estimated porosity as a function of carbon loading in the film

Several remarkable features can be noted from the Figure 35. First, the film has significant porosity ranging 15 to 35 percent. Second, the porosity initially decreases with an increase in carbon content up to a carbon content of 9 percent (based on pore-free ionomer-carbon film

volume) and then increases. It appears that upon increasing the carbon content it causes the Nafion® to pack more tightly leading to a less porous film. It is possible that at higher carbon loadings this behaviour no longer exists and the large amount of carbon creates very large pores in the film. This is supported visually by the fact that this high carbon loading film has cracks visible to the naked eye while lower carbon loadings appear to be uniform films as seen below. It should be noted that the volume of the film is estimated by examining the entire film despite the fact that it is thicker at the edges than at the center. It is then assumed that the porosity obtained is constant at all locations in the film.

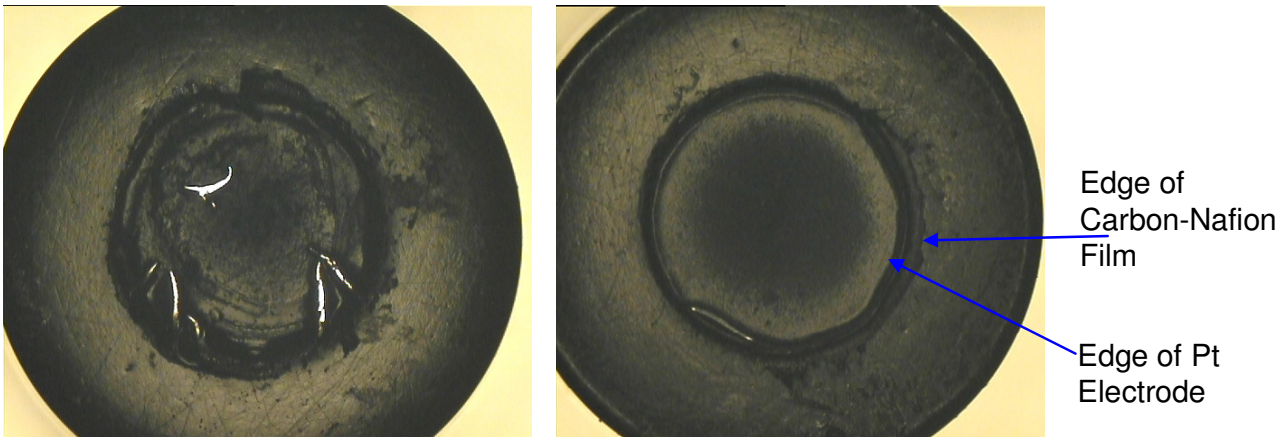

Figure 36: OGP Images of Films with 11.7% [Left] and 4.1% [Right] Carbon

Implications of Porous Ionomer-Carbon Film

The porous nature of the ionomer-carbon film affects the oxygen permeability through the ionomer phase of the film by introducing increased tortuosity. A more serious implication is that the pores will introduce additional pathway for oxygen transport. Thus, the permeability measured is an overall effective property which is affected by the porosity of the film. Further, to estimate the oxygen permeability through the ionomer phase, the theory discussed in section

3.1.2, which assumes dense ionomer-carbon film would have to be modified to account for the additional pathway.

4.1.3.4 Proposed Structure of the Films

Based on the estimated thickness and porosity of the film as a function of carbon content of the ionomer-carbon films, the following structure emerges for a film of approximately 5 vol% carbon.

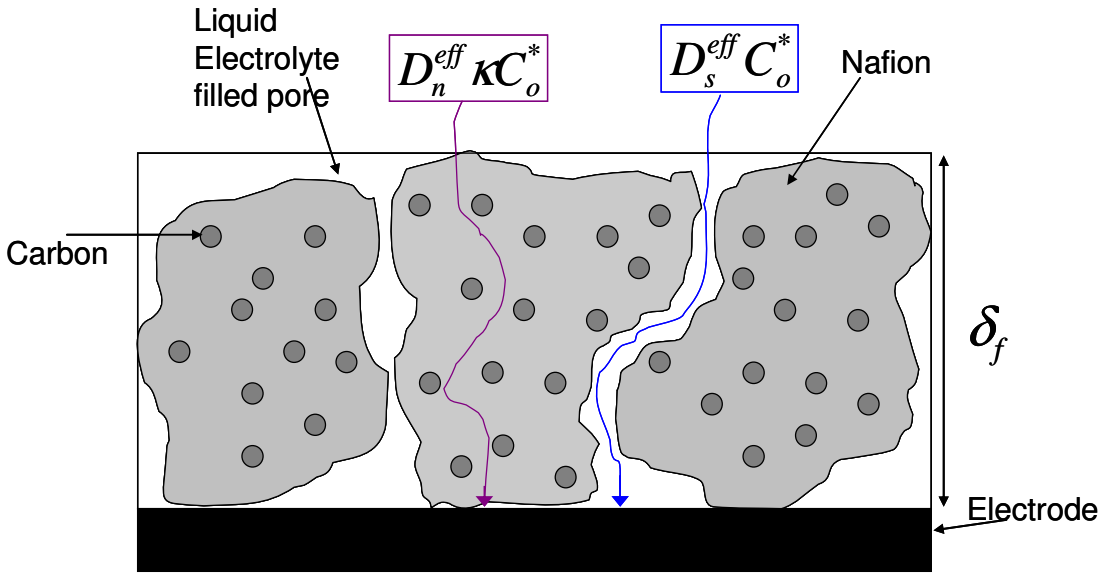

Figure 37: Schematic representation of Carbon/Nafion® film with 5 vol% Carbon

Based on visual inspection it appeared that at higher carbon loadings the porosity of the film decreased. This hypothesized is supported by Figure 35. Since the porosity decreases as carbon increases, at the highest carbon loading examined in these experiments, approximately 11% carbon, the diagram may appear more as shown below.

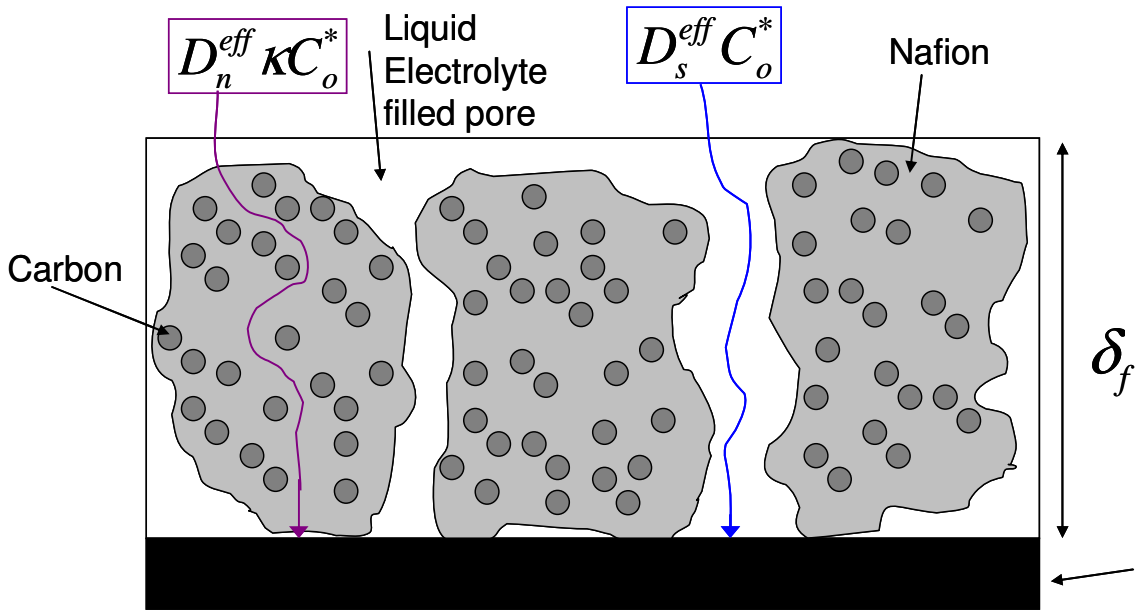

Figure 38: Schematic representation of Carbon/Nafion® film with 11vol% Carbon

4.1.4 Oxygen permeabilities in Nafion® – Data analysis accounting for film porosity

So far in the analysis of data, the porosity of the film has not been considered. Let us consider the pure Nafion® film (zero carbon content) system. From analysis in the preceding section, the film contains nearly 35% porosity. A schematic representation of the porous Nafion® film is shown in Figure 39 below. The pores of the film will be filled with the oxygen saturated electrolyte when it is immersed in the liquid electrolyte medium. The oxygen can be transported both through the ionomer phase and the electrolyte filled pore. Thus, two parallel pathways for oxygen transport exist – oxygen transport in liquid phase (though the liquid-filled pores) and the oxygen transport in ionomer phase. The permeability through a porous Nafion® film in a liquid electrolyte will be an overall property resulting from oxygen transport through two pathways.

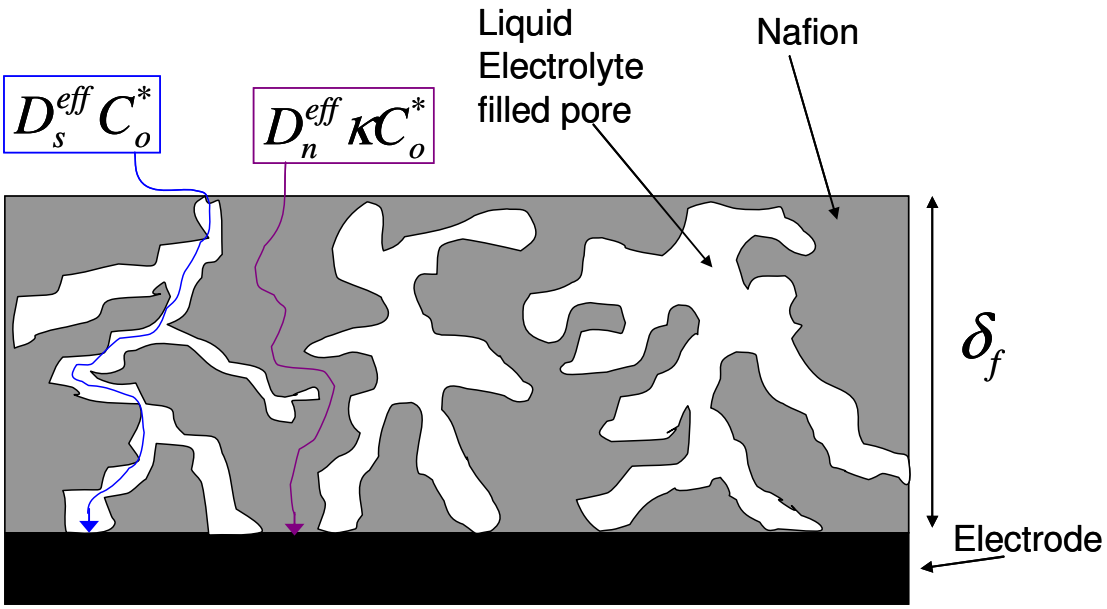

Figure 39: Schematic representation of porous Nafion® film

Now, the liquid filled pore can provide an alternative path to transport oxygen as shown by blue arrow. In such a case, the effective paths taken by oxygen depend on the characteristic transport lengths (pore diameter and ionomer strand thickness) and oxygen diffusivities in the two phases. Without the knowledge of the actual microstructure of the porous film, an appropriate analysis cannot be done. If a simplification is made that the oxygen transport occurs independently via two distinct non-interacting pathways, i.e. through the ionomer phase and through the liquid filled pores, then the effective transport property of the ionomer can be determined.

The transport rate of oxygen for each path (phase) can be expressed as a function of the oxygen diffusion coefficients of the respective phases as follows:

$$\begin{pmatrix}\text{Overall Transport}\\ \text{Rate of } O_2\end{pmatrix} = -D^{eff} A \frac{\partial C_o}{\partial x} \quad \textbf{(4-3)}$$

$$\begin{pmatrix}O_2 \text{ Rate Through}\\ \text{Nafion}\end{pmatrix} = -D_n^{eff} \frac{\partial C_o}{\partial x} \quad \textbf{(4-4)}$$

$$\begin{pmatrix}O_2 \text{ Rate Through}\\ \text{Pores}\end{pmatrix} = -D_p^{eff} \frac{\partial C_o}{\partial x} \quad \textbf{(4-5)}$$

As seen in Figure 39 it is possible to model the permeability as 2 parallel paths as follows:

$$\frac{1}{i_f} = \frac{\delta}{nF\left[AD_{o,overall}^{eff} C_{o,avg}^*\right]} = \frac{\delta}{nF\left[AD_p^{eff} C_o + AD_n^{eff} \kappa C_o^*\right]} \quad \textbf{(4-6)}$$

where, the subscript *p* refers to the pore-phase or electrolyte solution and the subscript *n* refers to the Nafion®-phase. From the above equation we can see that:

$$D_{o,overall}^{eff} C_{o,avg}^* = D_p^{eff} C_o^* + D_n^{eff} \kappa C_o^* \quad \textbf{(4-7)}$$

Now, the effective oxygen permeability in Nafion® ($D_n^{eff} \kappa C_o^*$), could be estimated if the effective permeability in electrolyte filled pores was known. Although, the oxygen permeability in the liquid electrolyte can be gathered from literature data, the modification of this quantity to account for the pores is required. In general for composite systems, the *effective* diffusion coefficient (or other transport properties) can be expressed in terms of the pure-phase diffusion coefficient and the volume fraction of the phase (ε) in the material of interest:

$$D^{eff} = D \cdot \varepsilon^a \quad \textbf{(4-8)}$$

where, the exponent *a* depends on the microstructure. Since the solubility is structure-independent, the effective permeabilities in equation (4-7) can be expressed via expression of the form indicated in (4-8) to yield:

$$D^{eff} C_o^* = D_p C_o^* \varepsilon_p^x + D_n C_o^* \varepsilon_n^y \qquad \textbf{(4-9)}$$

where, exponents x and y are unknown constants which depend on the geometry of the films. The porosity (ε_p) has been estimated from profilometry. The Nafion® volume fraction is then (1- ε_p).

Calculation of Nafion® Permeability

Estimation of Nafion® permeability via equation 4-9 requires knowledge of oxygen permeability in liquid electrolyte and the exponents *x* and *y*. The diffusivity and solubility of oxygen in 0.1M $HClO_4$ at 25°C reported in literature [63] is 1.93×10^{-5} cm^2/s and 1.26×10^{-6} mol/cm^3, respectively. Thus, the permeability can thus be calculated is:

$$D_p C_o^* = \frac{1.93\times10^{-5} cm^2}{s} \times \frac{1.26\times10^{-6} mol}{cm^3} = 2.43\times10^{-11} \frac{mol}{cm-s}$$

In section 4.1.3.2, the mean, overall oxygen permeability in porous Nafion® films was reported to be 1.52×10^{-11} mol/cm-s. The average film porosity was estimated to be 0.35 from profilometry. Next, the exponent '*x*' is required for estimating effective Nafion® permeability and, subsequently, the exponent '*y*' would be required to obtain the pure or pore-free Nafion® permeability.

In fuel cell modeling literature, the effective transport properties are commonly described by Bruggeman relation wherein the exponent of 1.5 is used assuming tortuous transport path. On the other hand, if the transport path is relatively straight an exponent of 1 can be expected. Without the direct knowledge of the microstructure of porous Nafion® film, the choice of one exponent over the other cannot be justified. The effective Nafion® permeability assuming exponent *x* (eqn 4-9) of 1 and 1.5 was calculated to be 0.67×10^{-11} and 1.013×10^{-11} mol/cm-s, respectively.

The Nafion® permeability can then be computed assuming the exponent *y* (eqn 4-9) of 1 and 1.5 to be 1.03×10^{-11} and 1.28×10^{-11} mol/cm-s, respectively if the effective permeability value of 0.67×10^{-11} mol/cm-s is considered. On the other hand, if the effective permeability value of 1.013×10^{-11} mol/cm-s is considered, the Nafion® permeability can be estimated to be 1.56×10^{-11} and 1.93×10^{-11} mol/cm-s for exponents of 1 and 1.5, respectively.

Next, the calculated Nafion® permeability is compared with the literature data.

4.1.4.1 Oxygen permeability in Nafion®: Comparison with previous studies

A summary of the results obtained experimentally by other groups at conditions which most closely match those in these experiments can be found below in Table 2.

Table 2: Summary of oxygen permeability in Nafion® reported by other researchers

System (Gas/Liquid)	Temp. (K)	Oxygen Pressure (atm)	Permeability$\times 10^{11}$ (mol/cm.s)	Reference
Gas	293	1.00	0.85	Broka and Ekdunge [59]
Gas	323	0.88	1.48	Zhang *et al* [58]
Gas	323	1.55	1.25	Parthasarathy *et al* [54]
Liquid	298	1.00	1.24	Gottesfeld *et al* [60]

Two of the data points above are at different temperatures and oxygen partial pressures than what is being studied in this case. As a result of the effect of temperature and pressure one must be cautious when comparing these values to experimental results.

In a previous experimental work [60], the Nafion® film was fabricated in the same manner as that in this thesis work. The estimated thickness of such films by profilometer but no mention and consideration of porosity was made. If it is assumed that the films created were similar in nature to those obtained experimentally in this study the diffusion through the pores must be subtracted from that through the Nafion® and the Nafion® property reported should still be reported as an effective property due to the tortuous path through which the oxygen must travel through the Nafion®. The porosity of Nafion® films determined by analysis of laser-profilometry data was determined to be 0.35. This relatively high porosity would likely result in interconnected pores as seen above and the effect of such pores significantly affects the permeability of oxygen obtained.

If it is assumed that the films studied in the previous case had similar pore characteristics as films created experimentally in this study, the average porosity estimated in this work to correct the

permeability and the following permeability through pure Nafion®, based on a Bruggeman correction is obtained:

$$D_p^{eff} C_o^* = D_p C_o^* \varepsilon_p^{1.5} = \frac{2.43\times10^{-11}(0.352)^{1.5}\,cm^2}{s} = 5.01\times10^{-12}\,mol/cm.s$$

$$D_n^{eff} \kappa C_o^* = (1.52\times10^{-11} - 0.50\times10^{-11})\frac{mol}{cm.s} = 1.02\times10^{-11}\,\frac{mol}{cm.s}$$

$$D_n \kappa C_o^* = \frac{D_n^{eff} \kappa C_o^*}{\varepsilon_n^{1.5}} = \frac{1.02\times10^{-11}}{0.648^{1.5}}\frac{mol}{cm.s} = 1.96\times10^{-11}\,\frac{mol}{cm.s}$$

The effective permeability through Nafion® is found to be 1.02×10^{-11} mol/cm-s, as commonly used in models, and the permeability of oxygen through pure Nafion® is estimated to be 1.96×10^{-11} mol/cm.s. In the liquid phase experiments, the value was corrected by both removing the effect of the pores and by accounting for the tortuous nature of the oxygen's path through the Nafion®.

It is possible that measurements carried out on the fabricated Nafion® membranes [54,58,59] are carried out on a pure Nafion® film, macro-pore free, in which case the experimentally obtained permeability is not an effective parameter, however no studies have been carried out on the Nafion® membranes properties to ensure that they are pore free. It is unlikely that the porosity of such membranes is as high as the films prepared in this study since porosities of 0.35 would likely results in gas crossover issues which are not typically observed in PEMFCs.

In gas systems [54,58,59] the dissolved oxygen can diffuse only through the Nafion®, thus no oxygen will diffuse through the pores and they do no contribute to the effective diffusion obtained experimentally. However the measured value should still be reported as an effective Nafion® permeability if there are likely still pores present which will act as a blocking layer to the diffusion of oxygen. This type of situation is seen below:

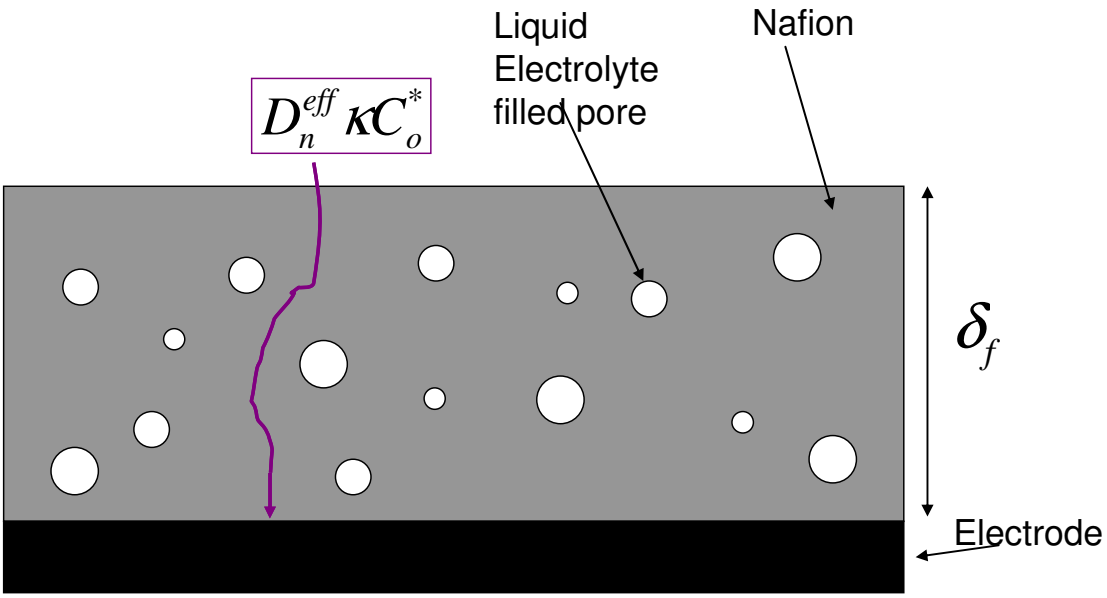

Figure 40: Schematic representation of Nafion® film with close pores

4.1.5 Oxygen Permeability in Carbon-Nafion® Film – Correction to Account for Porosity

The overall permeability of the ionomer-carbon films were reported in section 4.1.3.2 To extract the effective ionomer phase permeability, the formulation developed in section 4.1.4 can be adapted and equation (4-9) can be used. The porosity estimated from laser-profilometry data can be used and the ionomer volume fraction in the film can be obtained from the following set of equations:

$$\varepsilon_p + \varepsilon_n + \varepsilon_c = 1 \quad \textbf{(4-10)}$$

From the known solution composition the ratio of carbon and Nafion® can be determined:

$$\frac{\varepsilon_c}{\varepsilon_n} = R \quad \textbf{(4-11)}$$

The Nafion® volume fraction accordingly expressed as follows:

$$\varepsilon_n = \frac{1-\varepsilon_p}{1+R} \quad \textbf{(4-12)}$$

The effective permeability is obtained from the following equation and the data is analyzed for both cases of exponent x being equal to 1 and 1.5.

$$D_n^{eff} C_o^* = D^{eff} C_o^* - D_p C_o^* \varepsilon_p^x \quad \textbf{(4-13)}$$

The results of the analyses are presented in Figure 41 and Figure 42.

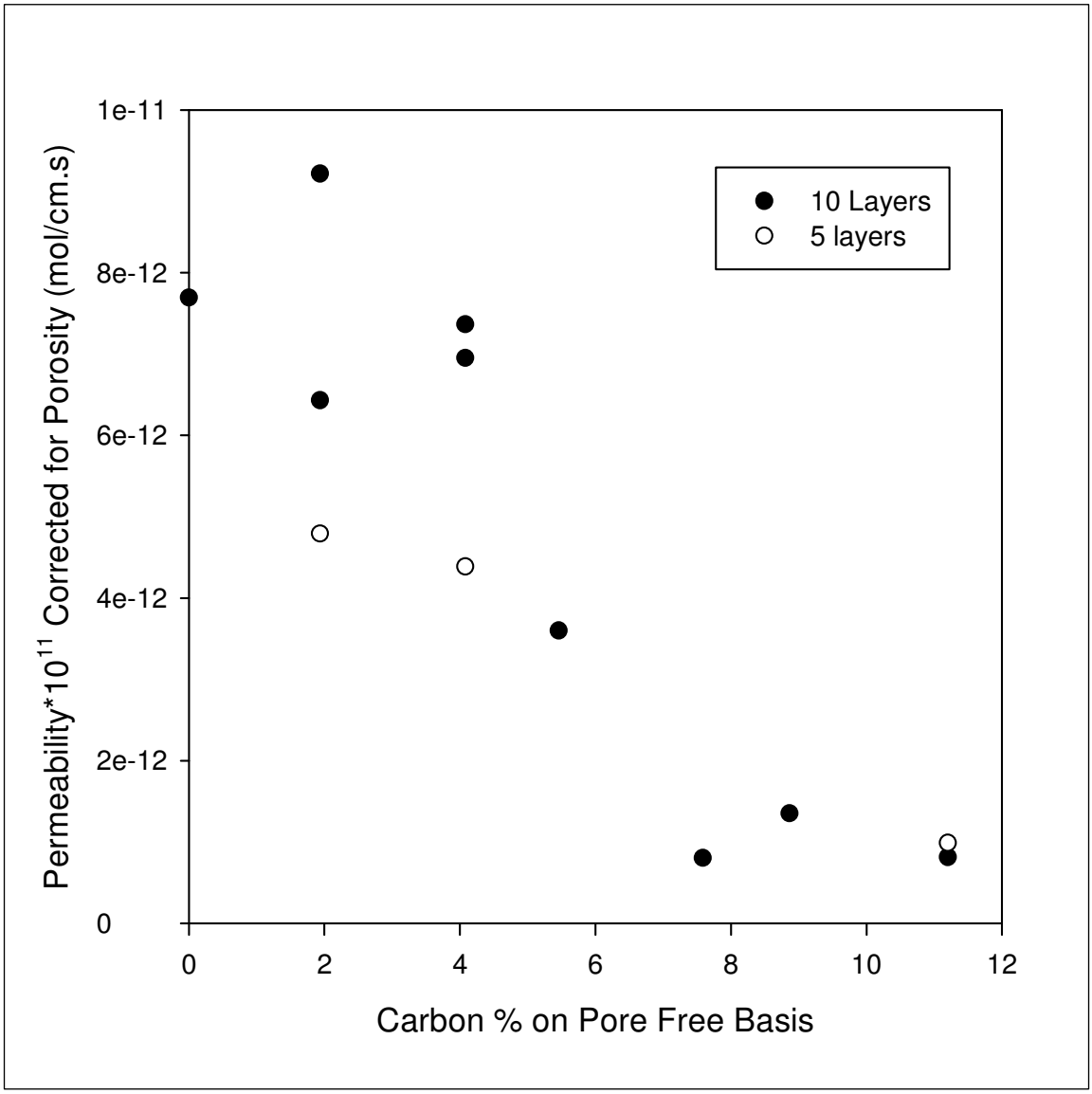

Figure 41: Effective Nafion® permeability as a function of carbon content assuming exponent x=1 in equation 4-13.

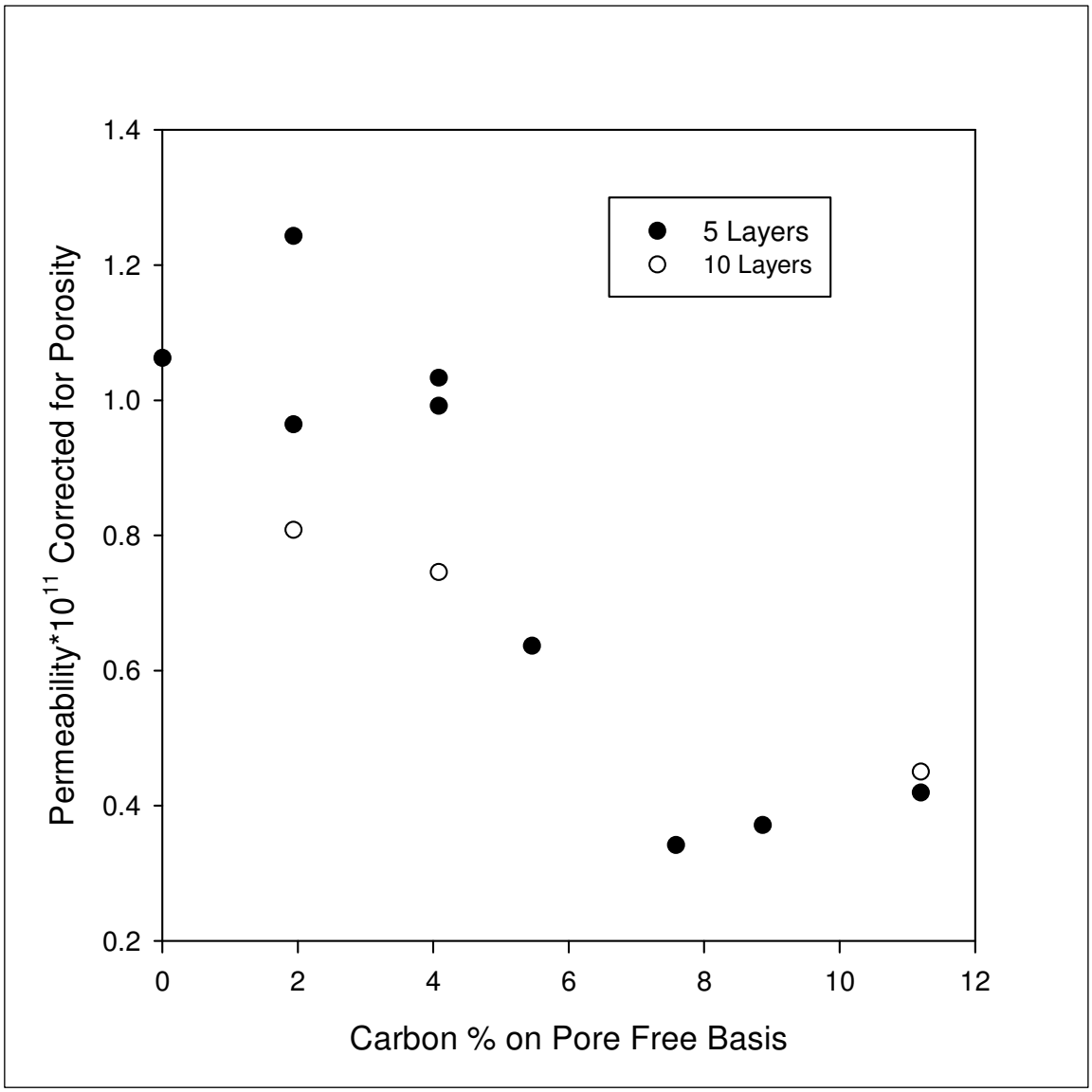

Figure 42: Effective Nafion® permeability as a function of carbon content assuming exponent x=1.5 in equation 4-13.

In each case, with x=1 and x=1.5, the resulting trend shows a decrease in the permeability of oxygen through Nafion® as the amount of carbon increases. This result suggests that the shape of the Nafion® film, created by pores, affects the transport of oxygen. It would appear that as more carbon is added to the films the path for transport of oxygen through the Nafion® becomes more

tortuous leading to a lower permeability. In the case where the exponent of 1.5 was used the resulting permeabilities are significantly higher than in the case where 1 was used.

Since the ultimate objective of the permeability measurement is to determine the relationship between the *effective* Nafion® permeability and the Nafion® volume fraction, further analysis was done. From equation 4-7, below the following relationship is expected:

$$C_o^* \kappa D_n^{eff} = C_o^* \kappa D_n \varepsilon_n^{\ y} \qquad \textbf{(4-14)}$$

A plot of $\log(C_o^* D_n^{eff})$ vs $\log(\varepsilon_n)$ should yield a slope of y and an intercept of $2\log(C_o^* D_n)$. This relationship is plotted below for permeabilities corrected on both x=1 and x=1.5:

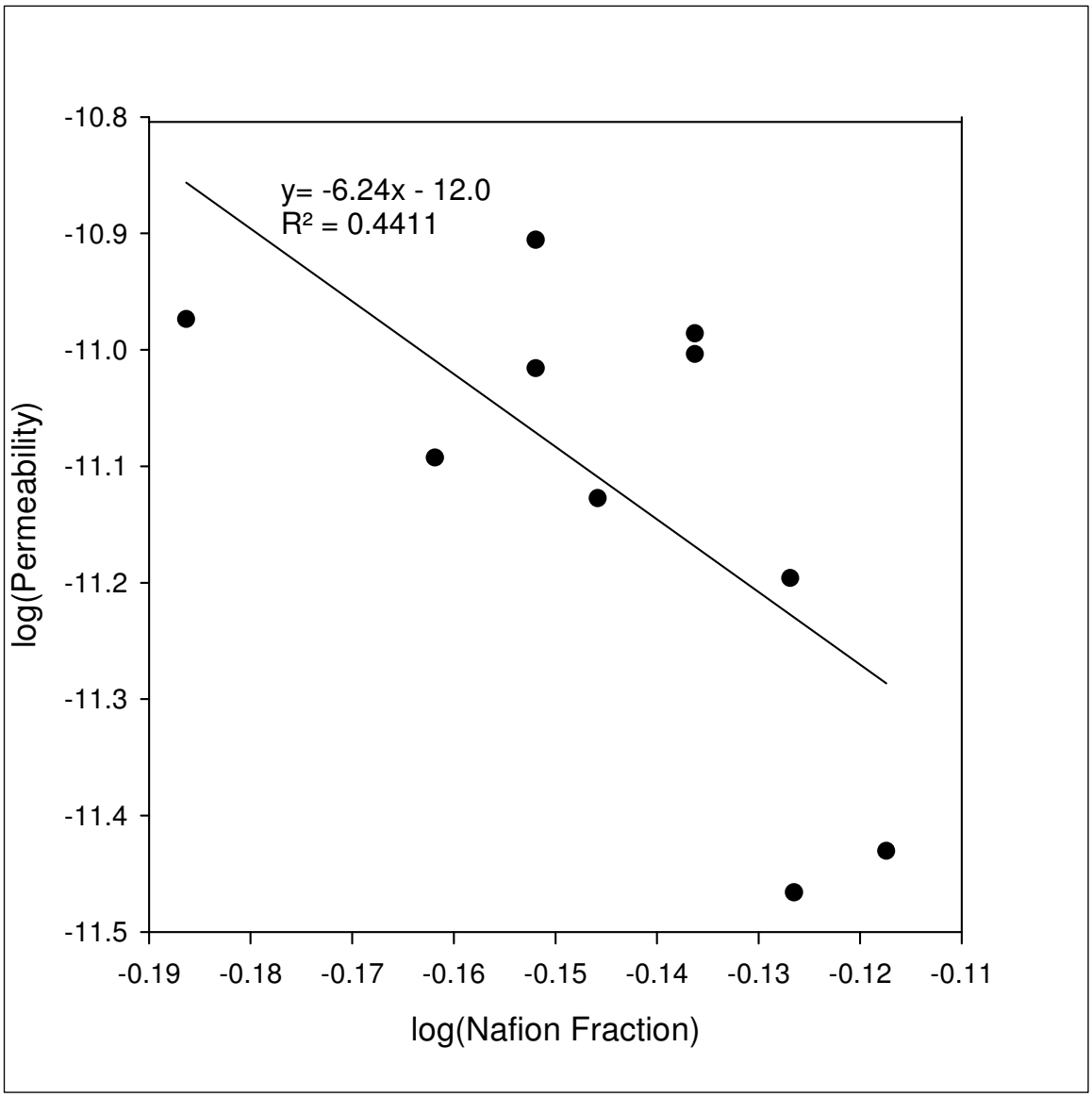

Figure 43: Plot of log (effective permeability) versus log (Nafion® volume fraction). Effective permeability obtained from equation 4-13 with x=1.5

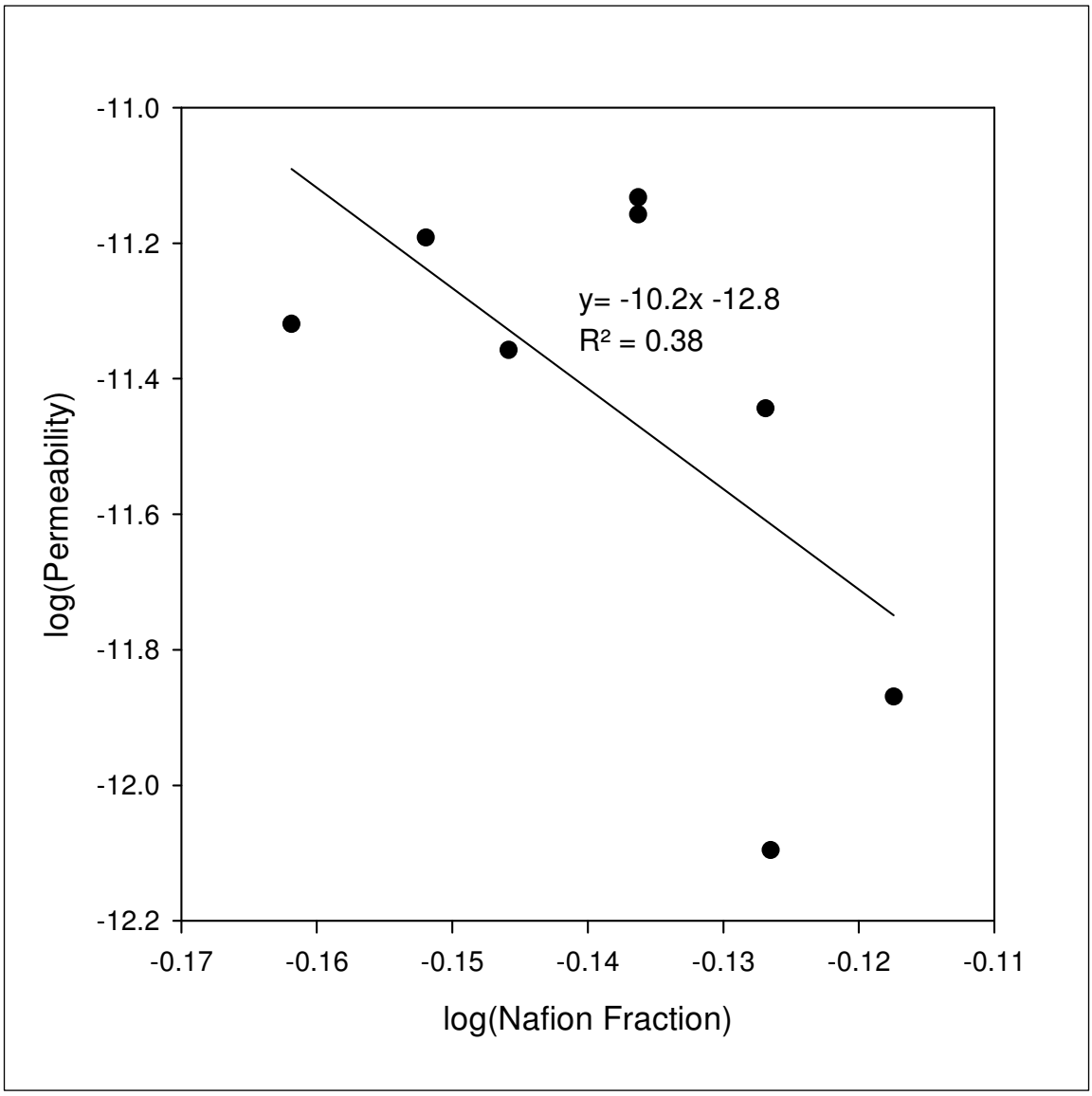

Figure 44: Plot of log (effective permeability) versus log (Nafion® volume fraction). Effective permeability obtained from equation 4-13 with x=1.0

It is clear from the R^2 value that a relationship does not exist based on the equation above in either case.

4.1.5.1 Discussion on Sources of Errors

There are many sources of error which could contribute to the lack of relationship between the Nafion® content and the effective diffusion of oxygen through the catalyst layer. Along with those listed above another source of error is the porosity of the film which is estimated by use of the OGP. The thickness of the films was determined by depositing the desired volume of solution onto a glass slide with the electrical tape acting as the electrode area as seen in Figure 20. It is possible that the film does not dry into the same form on the glass slide as it does on the electrode. Unfortunately the electrode is not an even surface and does not provide a flat baseline, thus, it is not possible to determine the thickness and porosity of the film after it has been deposited onto the electrode.

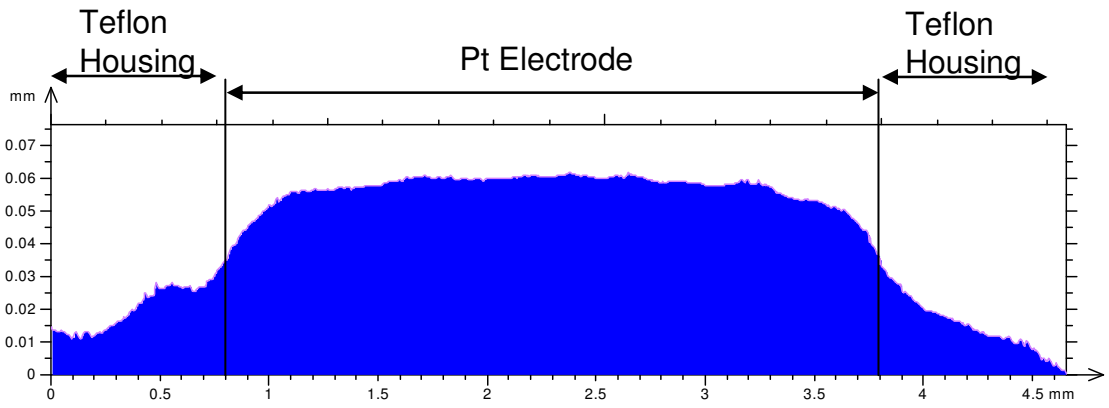

Figure 45: Platinum Bare Electrode Thickness Profile

Since the OGP measures the volume on a glass slide rather than on the platinum electrode, it is not possible to guarantee that the porosity obtained by the OGP is the same as the porosity which would be obtained for the actual film. Also it is possible that the porosity is not consistent

throughout the film as assumed. It may be different at the thicker edges of the film than in the center, unfortunately this cannot be determined by use of the OGP.

Another possible source of error is the use of the Levich model in determining the permeability. This equation was developed based on the velocity profile to a smooth surface. It is apparent from Figure 31 that the films created in these experiments are not smooth and of even thickness. It is possible that the velocity profile used to develop the Levich model is not valid for such films making the calculation of permeability inaccurate.

4.2 Pt/CNT Results

The functionalized CNT was characterized by XPS to examine the enhancement in surface functional groups after functionalization. Two methods for platinum deposition on CNT were attempted – the precipitation method and the colloidal/ethylene glycol method. The Pt/CNT catalysts synthesized were characterized for Pt electrochemical active surface area by cyclic voltammetry and for average Pt particle size by XRD and TEM. The activity of Pt/CNT catalysts for oxygen reduction reaction (ORR) was examined in liquid electrolyte system using rotating disk electrode system. The Pt/CNT catalyst performance in fuel cell environment was also examined.

4.2.1 Physical Characterization of CNT and Pt/CNT Catalysts

4.2.1.1 CNT Functionalization Determined by XPS

XPS has been used to examine enhancement of functional groups after the functionalization step involving oxidation in HNO_3-H_2SO_4 acid as described in section 3.2.2.2. As discussed earlier in

section 2.2.2, the functionalized groups contain oxygen. Thus, quantifying the oxygen peak present in the XPS spectra would allow assessment of whether the functionalization step resulted in an increase in oxygen-containing functional groups. Several samples were analyzed by XPS – as received (non-functionalized) CNT, in-house functionalized CNT, pre-functionalized CNT (Nanothinx CNT) and Pt/CNT samples obtained by both precipitation method and colloidal/EG method. The XPS analysis of Pt/CNT samples was carried out to confirm the existence of Pt. The areas of the O 1s and Pt peaks in the XPS spectra were computed and the results are presented in Table 3 below.

Table 3: XPS Results for CNT and Pt/CNT

	Oxygen Peak Area	Platinum Peak Area
As-received CNT	30139	*N/A*
In-house Functionalized CNTs	82753	
Pre-functionalized CNT (Nanothinx CNT)	74405	
Pt/CNT Sample prepared by Precipitation Method	38011	37489
Pt/CNT Sample prepared by Colloidal/EG Method (pH 8.5)	70181	48990
Pt/CNT Sample prepared by Colloidal/EG Method (pH 10.5)	70713	42691

As seen in Table 3 above the CNTs which are functionalized in the laboratory have a higher oxygen peak area than the functionalized CNTs purchased from Nanothinx. This suggests that catalyst created with the Nanothinx CNTs may not achieve active areas as high as those created

with the CNTs functionalized in house because the Nanothinx sample provides fewer sites for platinum deposition.

It is also important to examine the amount of oxygen sites remaining on the CNT/Pt samples after the deposition reaction. A lower number of available oxygen sites would suggest that a larger number of sites would have been utilized during the deposition process leading to smaller platinum size. Thus, samples with the smallest platinum size would also be expected to have the lowest oxygen peak area after the platinum deposition.

4.2.1.2 Quantification of platinum loading on CNTs

As stated above, two methods of Pt deposition on functionalized CNT was attempted – precipitation method and colloidal/EG method. Both methods are liquid-phase methods wherein the Pt precursor is present in a solubilized form. It is important to ascertain that at the end of the deposition process, all the Pt in the solution was deposited on the substrate CNT. Several samples of the supernatant liquid at the end of deposition process were analyzed for platinum content by atomic absorption. No platinum was detected in the supernatant liquid. Thus, the average platinum loading (mass of Pt per mass of CNT) was calculated by dividing the Pt mass in the media for deposition by the mass of CNT in the media.

4.2.1.3 Electrochemically Active Surface Area (ECSA) of Pt/CNT Catalysts by Cyclic Voltammetry

The quantification of Pt ECSA for Pt/CNT required modification of the standard cyclic voltammetry methods based on hydrogen adsorption or desorption area in nitrogen saturated electrolytes. For pure platinum electrode, a double layer current nearly invariant with potential is

observed in the 0.35 to 0.5 V (vs standard hydrogen electrode) or 0.13 to 0.28 V (vs Ag/AgCl electrode) potential range. The peak area for hydrogen adsorption or desorption is calculated by subtracting the baseline defined by the double layer current region. For supported catalysts such as Pt on CNT, a complication arises in that a peak is observed rather than a flat double layer current response in the so called double layer region (see Figure 46 below) A previous study has suggested that this peak is associated with the pre-monolayer oxidation of platinum [64] however from Figure 46, it is apparent that this peak is present for functionalized CNTs where no platinum is present. It is also possible that this peak is associated with the adsorption of hydrogen onto un-reacted functionalized sites [65]. The C-O, C-OOH, C-N and C-S groups which form on the CNT surface should not be present at a significant level after deposition if the deposition has occurred in the desired manner. However, in this case it can be seen that the area under this peak is comparable to the area under the peak associated with adsorption of hydrogen onto platinum suggesting that many of the functionalized groups have not bonded to Pt. It can be safely stated that the origin of the peak observed for Pt/CNT CV in the classical double layer region is not fully understood.

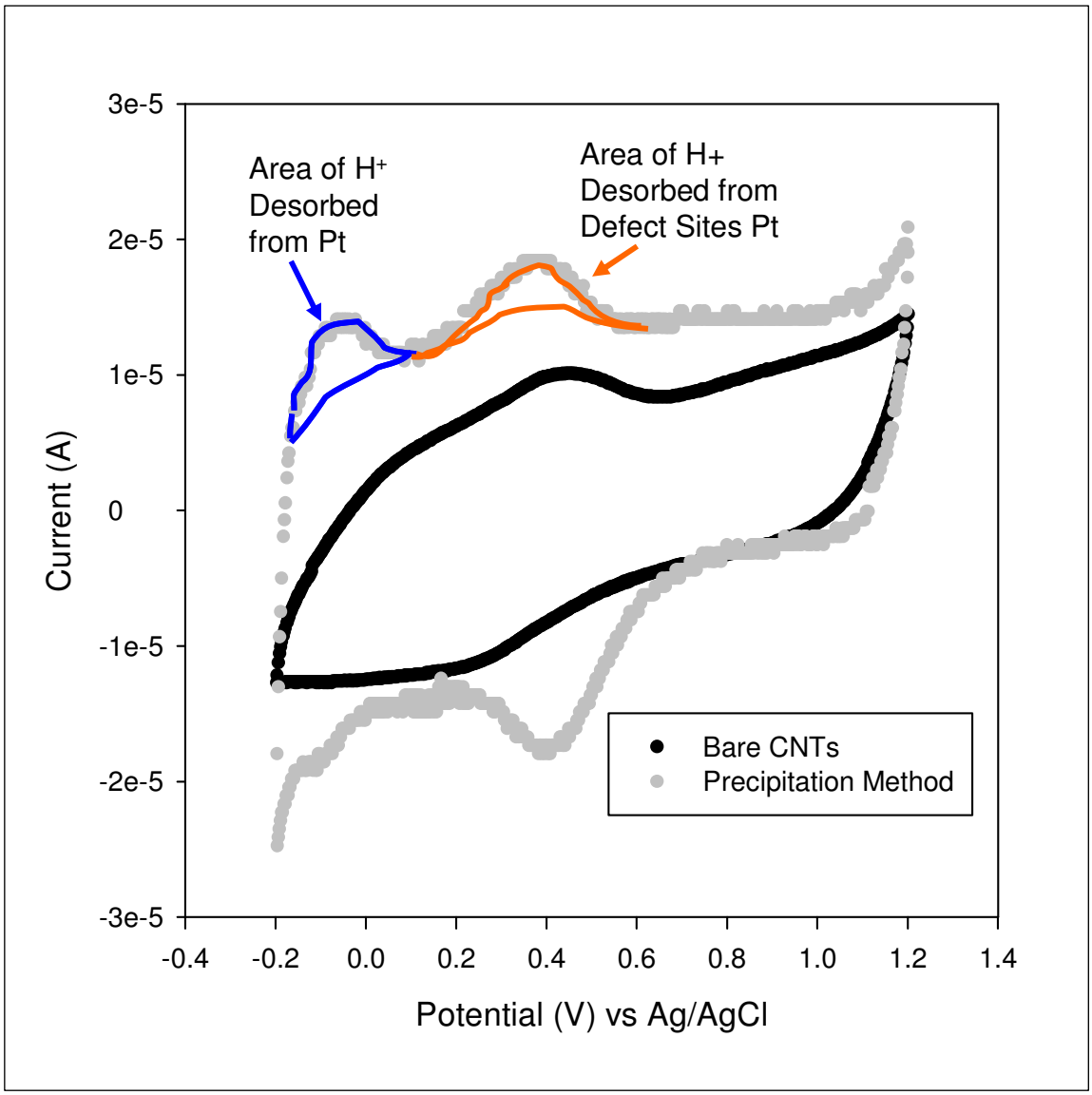

Figure 46: Cyclic voltammetry showing methodology for baseline correction

[Run at 25°C and 101.3 kPa in $HClO_4$ electrolyte saturated with Ar, 20 mV/s scan rate.]

To further complicate the analysis, it is possible that every batch of functionalized CNTs will have slightly different surface areas due to the amount of defect sites as well as the amount of CNTs being examined. However, in this study, it was observed that the CV shape of bare CNT is reproducible (see Figure 24) and that the current produced increases or decreases dependent

likely on the surface area and defect sites of the CNTs. Thus, to obtain a baseline, the CV for bare CNTs were scaled by multiplying the current response by a certain factor such that the scaled current was the same as the current for Pt/CNT CV in the classical double layer region (~0.1─0.15 V on a Ag/AgCl scale) for Pt in acid electrolytes. This method for correction of baseline is shown in Figure 46 above.

The surface area for hydrogen desorption was calculated to obtain the electrochemically active area of the platinum in Pt/CNT catalysts prepared by the two different methods.

Pt/CNT Catalyst Prepared by Precipitation Method

An example of the CV for Pt/CNT catalyst prepared by precipitation method is shown in Figure 47 below. However, the deposition of Pt on CNT by the precipitation method was not found to be reproducible. The Pt ECSA calculated from the CV for the best sample (maximum area) result the mean particle size is presented in Table 4 below.

Table 4: ECSA and Pt size for Pt/CNT Prepared by Precipitation Method

	Precipitation Method	Benchmark Values
Electrochemically Active Area (m^2/g_{Pt})	23.8 ± 2.4	70 [50]
Mean Particle Size D_p (nm)	~ 12	~ 4

For comparison, the benchmark values [50] reported for commercial platinum supported on carbon black (Pt/C) catalysts is also reported. It is apparent that the precipitation method yields significantly lower ECSA than the benchmark value.

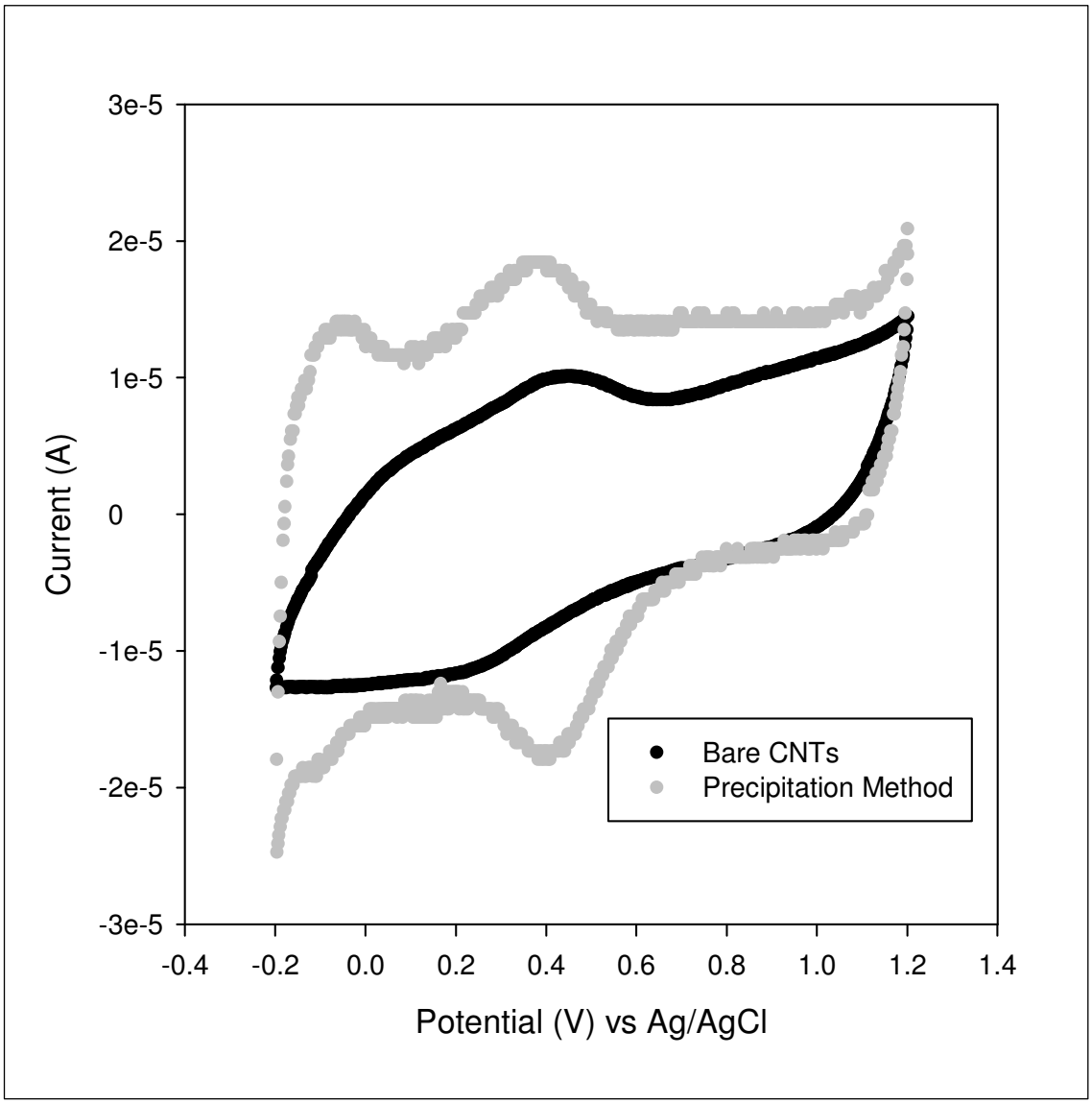

Figure 47: CV for Catalyst Prepared by Precipitation Method. Run at 25°C and 101.3 kPa in $HClO_4$ electrolyte saturated with Ar, 20 mV/s scan rate.

Pt/CNT Catalyst Prepared by Colloidal Method

The electrochemically active surface area of Pt/CNT synthesized by colloidal/EG method was determined in a manner similar to discussed above. One of the variables in the EG method is the

pH of the solution. The cyclic voltammograms of Pt/CNT catalysts synthesized at four different pH levels are presented below in Figure 48.

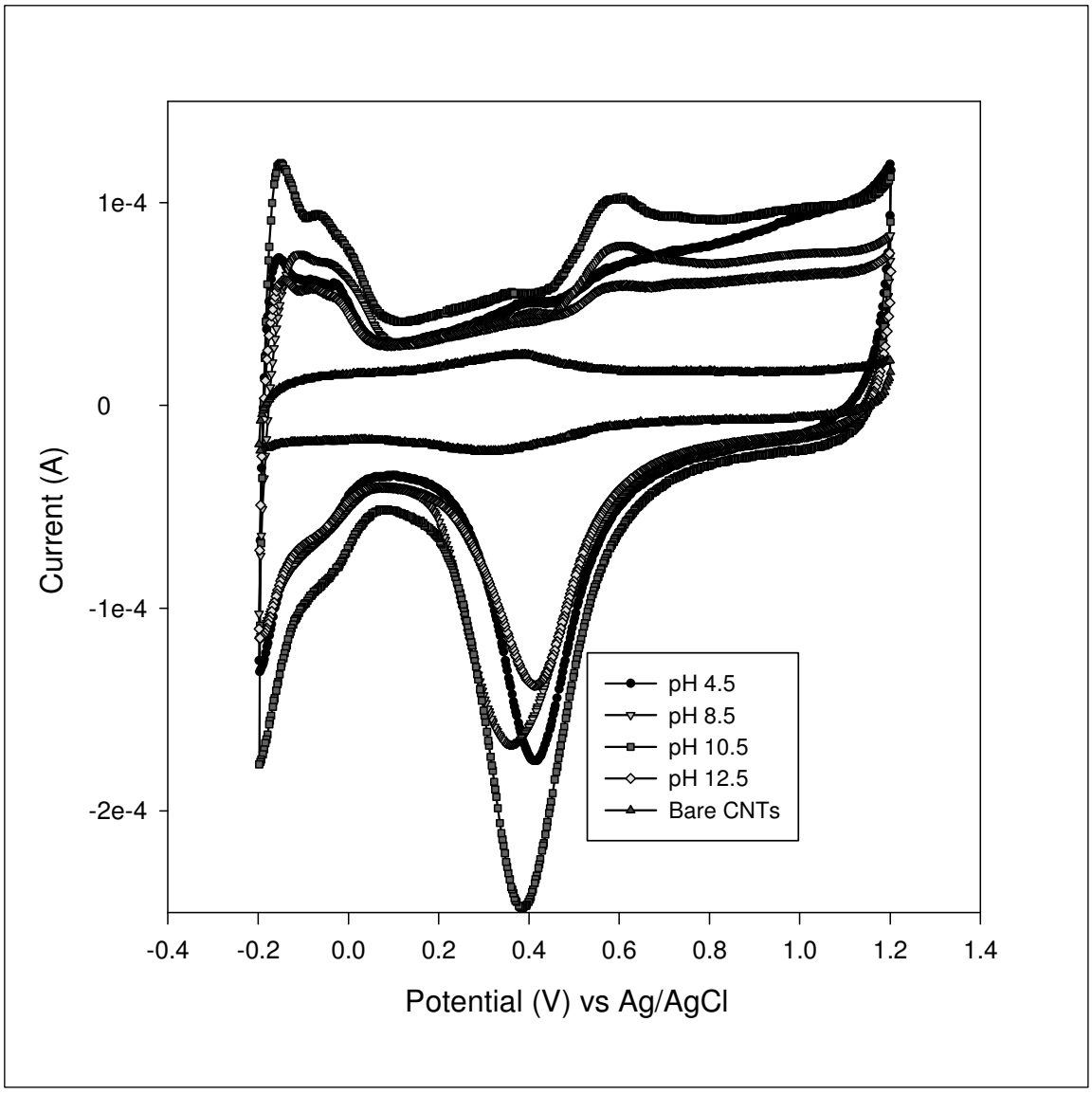

Figure 48: CV for Catalyst Created by EG Method. Run at 25°C and 101.3 kPa in $HClO_4$ electrolyte saturated with Ar, 20 mV/s scan rate

The bare CNTs were once again used as the baseline for the hydrogen adsorption onto platinum peak. In all cases for synthesis, the filtrate of the EG experiments yielded undetectable levels of

platinum as determined by atomic absorption method and, thus, all the platinum present in the experiment was assumed to be deposited onto the CNTs.

The mass specific electrochemically active surface areas (ECSAs) are presented in Table 5:

Table 5: ECSA and Pt size for Pt/CNT Prepared by Colloidal/EG Method

	pH 4.5	pH 8.5	pH 10.5	pH 12	Benchmark Values
Electrochemically Active Area (m^2/g_{Pt})	80	110	134	84	70 [50]
Estimated Mean Particle Size (nm)	~3.4	~2.5	~2	~3.3	~4

At least two key observations can be noted from the results presented in Table 5 above. The ECSAs for the synthesized Pt/CNT catalysts are higher than the benchmark values reported for Pt/C catalysts. The pH has a significant effect on the Pt particle size. Now, as mentioned earlier, the high viscosity of the EG is expected to slow the movement of platinum to the defect sites resulting in the lower platinum particle size as seen in these CV experiments. In a previous work [47] wherein a similar EG procedure as that carried out in this study but using carbon nanostructures rather than CNTs, an active area of 58.5 m^2/g_{Pt} was obtained. These experiments were carried out at a pH of greater than 12. Also, based on the experimental procedure outlined in the paper, it is not apparent whether the pH was maintained at the same value during the experiment. If the pH was not maintained it is possible that the pH dropped during the experiment leading to the lower active area obtained in these previous experiments. The carbon nanostructures also may not be as good of a support as the CNTs. It is possible that not as many defect sites are created leading to the lower active surface area.

Influence of pH: Referring to Table 5, for cases with pH <12, there also seems to be a general increase in attainable active area or a decrease in particle size as the pH increases. This trend has been observed in similar experiments carried out by microwave heating in EG [51]. This may be explained based on the following mechanism [51]: At high temperatures, EG decomposes into acetaldehyde as follows:

$$CH_2OHCH_2OH \rightarrow CH_3CHO + H_2O \quad \textbf{(4-15)}$$

The acetaldehyde acts as a reducing agent as follows:

$$2CH_3CHO + Pt(Cl_6)^{2-} + 6OH^- \rightarrow 2CH_3COO^- + Pt + 6Cl^- + 4H_2O \quad \textbf{(4-16)}$$

It has been theorized that the acetate ion is a good stabilizer for metal collides possibly by forming chelate-type complexes that are more stable than their non chelated counterparts [51]. By examining equation 4-3 it is apparent that as the pH increases the acetaldehyde will form more CH_3COO^- resulting in more stable Pt^- particles in solution and thus smaller Pt^- particles deposited at the defect sites.

Reproducibility of Pt/CNT catalyst synthesized by EG Method and the Influence of CNT Type: In order to determine reproducibility of Pt/CNT catalyst synthesized, 2 sets of experiments were carried out at a pH of 8.5. The first experiment was an exact replicate of the original whereas for the second experiment pre-functionalized CNTs purchased from Nanothinx was used. The details of functionalization of Nanothinx CNT were not available, however, from the XPS analysis it is known that the functionalized CNT has slightly lower amount of oxygen-containing species. The cyclic voltammograms of these Pt/CNT catalysts are shown in Figure 49 below.

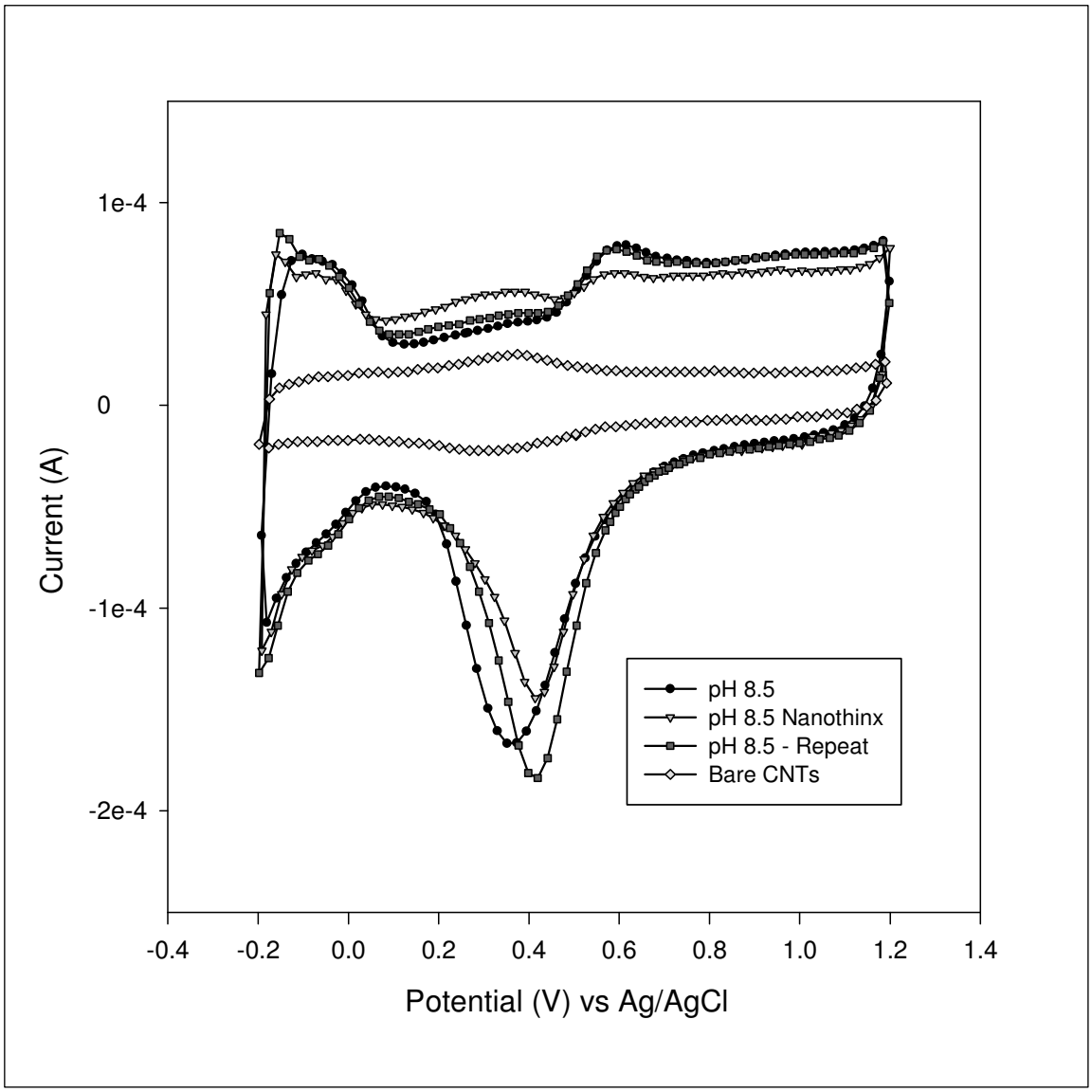

Figure 49: Cyclic Voltammograms for EG Method pH 8.5. Run at 25°C and 101.3 kPa in $HClO_4$ electrolyte saturated with Ar, 20 mV/s scan rate.

The peak areas are similar in the hydrogen desorption region although small differences can be noted. To quantify these differences, the ECSA was estimated and is reported in Table 6 below.

Table 6: ECSA and Pt particle size for Pt/CNT synthesized by EG Method at pH 8.5

	Original	Replicate	Nanothinx	Benchmark Values
ECSA (m^2/g_{Pt})	110	105	76	70 [50]
Mean Pt Particle Size (nm)	~2.5	~2.6	~3.6	~4

The replicates of Pt/CNT catalyst synthesized using in-house functionalized CNT produces yields ECSA similar to the each other with an average active area of 107.4 m^2/g_{Pt}. However, the sample synthesized with Nanothinx functionalized CNTs resulted in a lower active area. This may be attributed to smaller number of functional groups on the CNT which translates into a smaller number of sites available for the Pt^+ to bond. It can be readily deduced that for a given amount of Pt to be deposited, smaller number of nucleation/deposition sites would result in larger particles.

Other Observations: From Figure 48 and Figure 49 it is clear that there is still a slight peak at approximately 0.35 V (vs Ag/AgCl) however it is much less pronounced than the peak observed for the catalyst prepared by the precipitation method. It should be noted that this peak is different for the catalyst prepared with the CNTs which were pre-functionalized. Thus the method of functionalization appears to affect the size and shape of this peak which supports the hypothesis that it may be due to the adsorption of hydrogen to the functionalized groups. The fact that this peak is smaller for the EG method than the precipitation method is again attributed to lesser degree of functionalization (see Table 3) the Pt has bonded to the majority of the functionalized groups eliminating any effect they have on the CV obtained. The remaining small peak at 0.35 V may be due to the pre-monolayer oxidation of platinum.

4.2.1.4 Pt/CNT Characterization by XRD

In order to verify the platinum particle size estimated from the active area obtained by CV, *X-ray Diffraction* (XRD) was run on each catalyst sample. A typical XRD spectra obtained for a CNT/Pt catalyst was presented in Figure 22 in section 3.2.2.2. The average particle size can be computed from the Sherrer equation:

$$D_p(nm) = \frac{0.94\lambda}{\beta_{1/2}\cos\theta} \quad \textbf{(4-17)}$$

Where:

λ – Wavelength of the radiation

$\beta_{1/2}$ – FWHM (Full Width at Half Maximum)

θ – The position of the maximum of diffraction

The results of Pt crystal size estimated from XRD analysis is presented later in Table 7 (in section 4.2.1.6).

4.2.1.5 Pt/CNT Characterization by Transmission Electron Microscopy

The synthesized Pt/CNT catalysts were also examined by high resolution tunneling electron microscopy. The micrographs of various Pt/CNT samples are presented below in Figures 49 and 50 below.

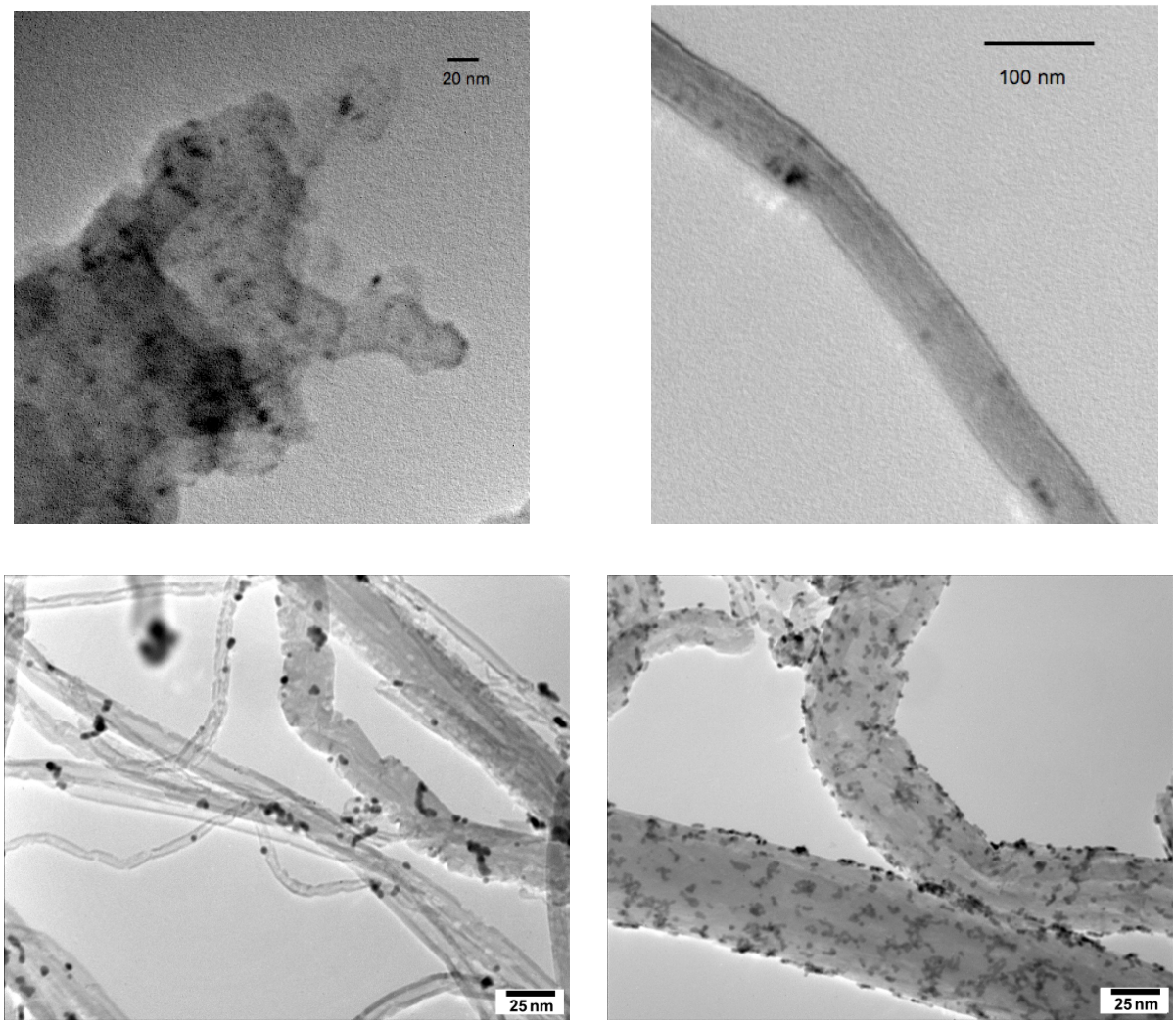

Figure 50 : TEM Images clockwise from top left: Commercial Catalyst 10% Pt on C, Pt/CNT -Precipitation Method, Pt/CNT - EG Method pH 4.5, pH 8.5

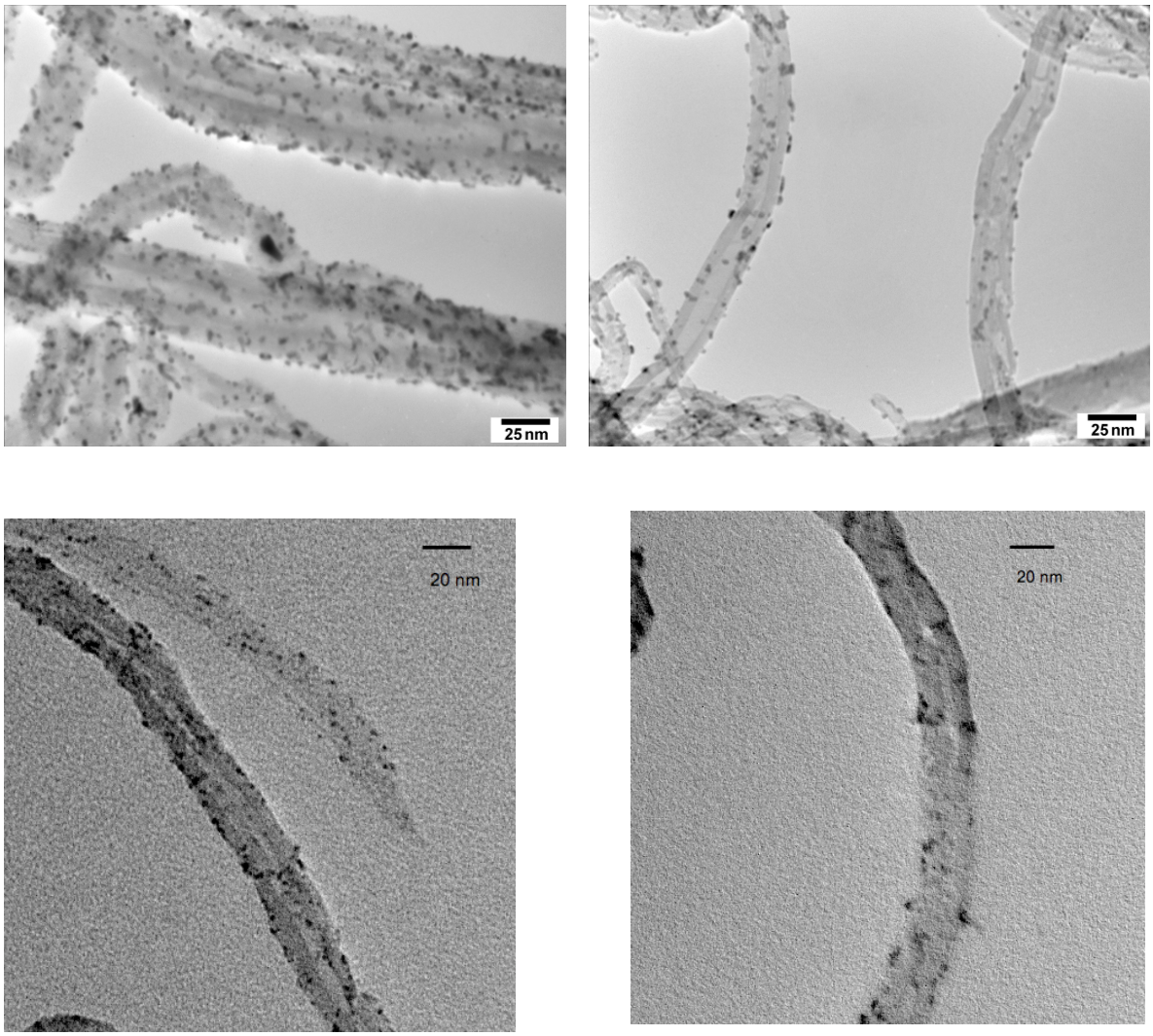

Figure 51: TEM images for Pt/CNT catalysts prepared by EG Method at different PHs. Clockwise from top left - pH 10.5, pH 12, pH 8.5 redone, pH 8.5 pre-functionalized

From Figure 50 and Figure 51 the particle size was calculated by enlarging the TEM images and measuring the particle size by using the scale indicated. It was found that the particle size of all catalyst created by the EG method were significantly lower than that of catalyst created by the precipitation method. Also a slight trend indicated that the particle size decreases with pH up to a

pH of 12 indicating again that there may be an optimum pH for catalyst preparation. The results of the particle size estimation are summarized below in Table 7.

4.2.1.6 Comparison of Pt size determined by different techniques

The Pt particle size was evaluated by the three methods - ECSA from CV, XRD and TEM - are summarized in Table 7 below.

Table 7: Pt particle size (of Pt/CNT catalysts) determined by three different methods

		Preparation Method						
		Ppt Method	EG Method					
	pH	NC	4.5	8.5	10.5	12	8.5	8.5
ECSA		12	3.4	2.5	2	3.3	2.6	3.6
XRD		6.4	2.5	0.84	0.84	1.2	1.3	2.3
TEM		6-12	3-6	1-2	1-2	1-3	1-2	1-3
	Carbon substrate	F-CNT	F-CNT	F-CNT	F-CNT	F-CNT	F-CNT	Nanothinx CNT

*F-CNT – Functionalized CNT

The particle size estimated by XRD is in all cases lower than that estimated by CV. There are several reasons for this. To begin with XRD is only able to detect crystal lattice structures. It is possible that some of the platinum present is deposited as larger particles with crystal imperfections making them not detectable by XRD and leading to a lower particle size than actually present. Also the XRD estimates the actual crystal size but it is possible that some of the crystals are agglomerated together forming bigger particles, which will manifest as large particle size both in electrochemical method and TEM observations. Secondly it is possible that not all the catalyst deposited onto the electrode was connected electronically to the electrode. The electrode is housed in a Teflon housing and the catalyst ink was deposited onto both the electrode and the

housing. If some platinum particles are not connected electronically to the electrode they will not contribute to the active area obtained.

From the TEM images it is apparent that more evenly dispersed smaller particles are obtained at a higher pH. Unfortunately, due to the very small particles obtained and the resolution which was attainable on the TEM, it is difficult to obtain estimations of actual particle size from these images. It is, however, visible that the particle size is smaller than the commercial catalyst which has a platinum particle size of 4 nm. This supports the higher surface areas obtained for the novel catalysts and suggests they may perform better in PEM applications.

4.2.2 Electrochemical Kinetic Characterization of Pt/CNT Catalysts for Oxygen Reduction Reaction in a Liquid Electrolyte Medium

The high mass-specific Pt surface area of the Pt/CNT catalysts indicates that Pt/CNT catalyst is suitable for application in polymer electrolyte fuel cells. Since the oxygen reduction reaction (cathode reaction) is significantly more sluggish than the hydrogen oxidation reaction (anode reaction). It was of interest to further characterize the behavior of the Pt/CNT catalyst for ORR. Fundamentally, the ORR electrochemical kinetics for Pt/CNT catalysts should be no different than Pt/C catalysts. As discussed in section 3.2.3, the two parameters of interest are exchange current density (i_o) and Tafel slope ($b=RT/\alpha F$). The kinetic parameters of the Pt/CNT catalyst have been evaluated by running RDE experiments and analyzing the data as per method described in section 3.2.4. An example of the plot obtained from such experiments for the Pt/CNT catalysts synthesized by colloidal/EG method (pH of 8.5) is presented in Figure 52 below.

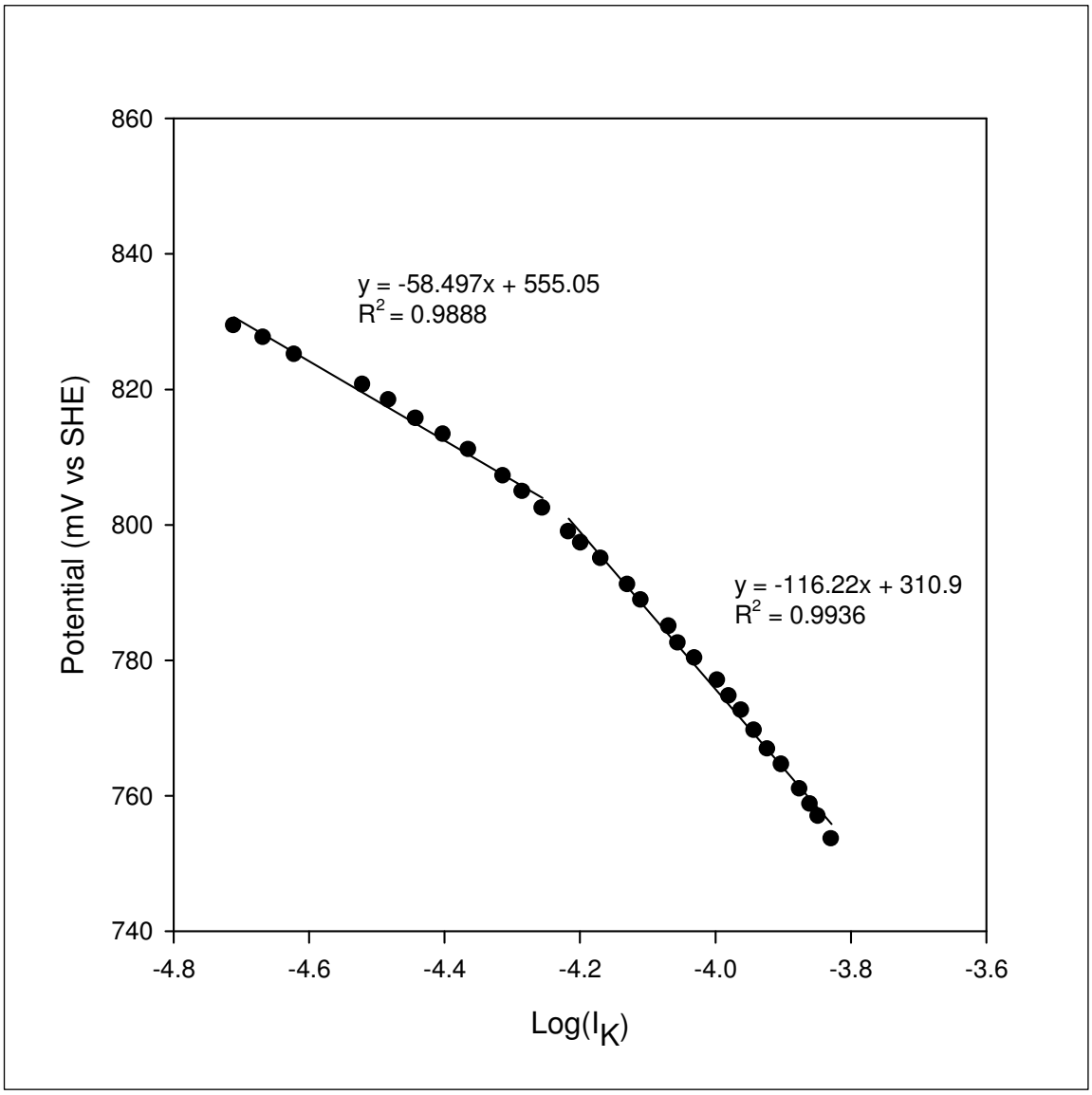

Figure 52: Tafel plot for Pt/CNT catalyst synthesized by EG method at pH 8.5. Experimental Conditions: 25°C and 101.3 kPa in $HClO_4$ electrolyte saturated with O_2, 20 mV/s scan rate.

Two Tafel slopes ($b=\partial V/\partial i$) can be observed in Figure 52 above. In the low current density region, the Tafel slope of ~60 mV is observed whereas nearly a double that slope is observed for the higher current density region.

The Tafel slopes for both the high current density and low current density regions for each catalyst is presented in Table 8 below. The commercial catalyst was a 10% Pt/C E-TEK catalyst which has Pt loading lower than the 15% Pt/CNT catalysts synthesized in this study.

Table 8: ORR Electrochemical Kinetic Parameters for Pt/CNT and Pt/C Catalysts

Experiment ID	Tafel Slope (mV/dec)	i_o(A/cm^2 $_{Pt}$)×10^5	-log(i_o) (mA/cm^2)
Commercial Pt/C Catalyst	56.1 122.0	5.0	6.9
Pt/CNT - EG pH 4.5	59.9 121.5	6.6	6.6
Pt/CNT - EG pH 8.5	60.2 121	7.6	6.5
Pt/CNT - EG pH 10.5	60.7 120.2	18.9	5.6
Pt/CNT - EG pH 12	58.5 116.2	6.8	6.5
Pt/CNT - EG pH 8.5 replica	59.8 122.1	7.0	6.6
Pt on Nanothinx CNT (EG pH 8.5)	58.1 121.5	7.3±0.6*	6.6

*Variability refers to average of 4 samples

Kinetic parameters extracted from a fuel cell polarization data has been reported in the literature; an exchange current densities of 1.5×10^{-7} A/cm^2 [57] was reported, which is significantly lower than the values reported in this study. As discussed earlier a high exchange current density results in a faster reaction kinetics. Previous liquid electrochemistry studies of PEMFC catalysts [56] have found log(i_o) values of -6.19 mA/cm^2 in 0.1M H_2SO_4 electrolyte. However, a direct

comparison cannot be made because the differences in the concentration and type of electrolyte affects the kinetic parameters obtained. Although this difficulty in comparison is present, it is apparent that the kinetic parameters obtained in these experiments are in the expected range for PEMFCs.

It is useful to point out that the kinetic region used in the determination of Tafel slopes above was not constant for all data sets. The lower potential ranges from 723 mV vs SHE to 752 mV vs SHE and the higher end ranging from 821 mV vs SHE up to 852 mV vs SHE. This range should be constant for each catalyst and this variability may be the result of experimental error. The Tafel slopes for each catalyst are comparable to those typical of Pt/C catalysts [57] as expected since the reaction mechanism is expected to be the same. The exchange current densities for all Pt/CNT catalysts, except that prepared at pH of 10.5, are within +/- 0.5×10^{-5} A/cm^2_{Pt} of the average i_o value of 7.1 A/cm^2_{Pt}. The exchange current density for Pt/CNT (pH=10.5) catalyst is more than double the average value. This is surprising because the exchange current density has already been normalized for the electrochemically active area. However, some researchers have argued that even after allowing for the surface area factor, there is a particle size effect on ORR kinetics.

4.2.2.1 Effect of Pt Size on Pt Oxidation

If the ORR mechanism is considered, the first step would involve oxygen adsorption onto the surface of the platinum. The oxygen can dissociate into oxygen atoms followed by electron transfer reaction. On the other hand, electron transfer can occur with the adsorbed molecular oxygen. Irrespective of the preceding steps, the final step of the ORR mechanism is the formation of water. The water formed must leave the surface of the platinum. Thus, a fine balance is required for the strength of the bond of oxygen to the platinum surface. If the bond is too weak

the oxygen will not adsorb to begin with and, if it is too strong the water produced will not leave the surface after the reaction. In the latter case, the oxygen acts as a poisoning agent for the platinum since it blocks the site for further reaction. It is believed that the size of the platinum particle may affect this oxygen bond strength [66,67,68]. In order to examine this effect, the oxidation peak location for the experiments run from Figure 48 and Figure 49 is compared to the platinum crystal size obtained as seen below in Figure 54. This relationship is observed based on the peak points, 0.351 V in Figure 53.

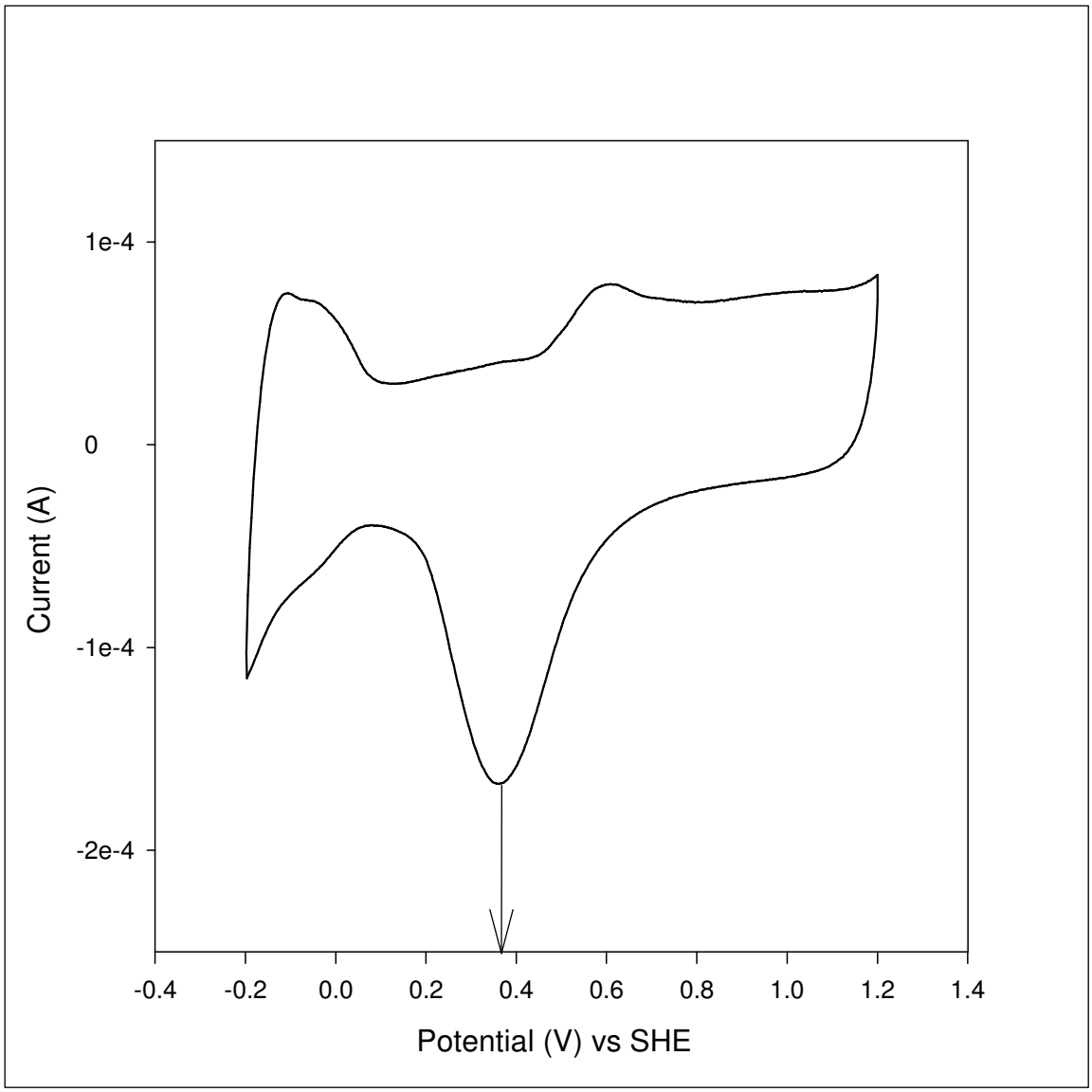

Figure 53: Cyclic voltammogram for Pt/CNT catalyst in $HClO_4$ acid saturated with Ar showing Pt oxidation peak, run at T=25°C, P=1 atm, Scan rate=20mV/s

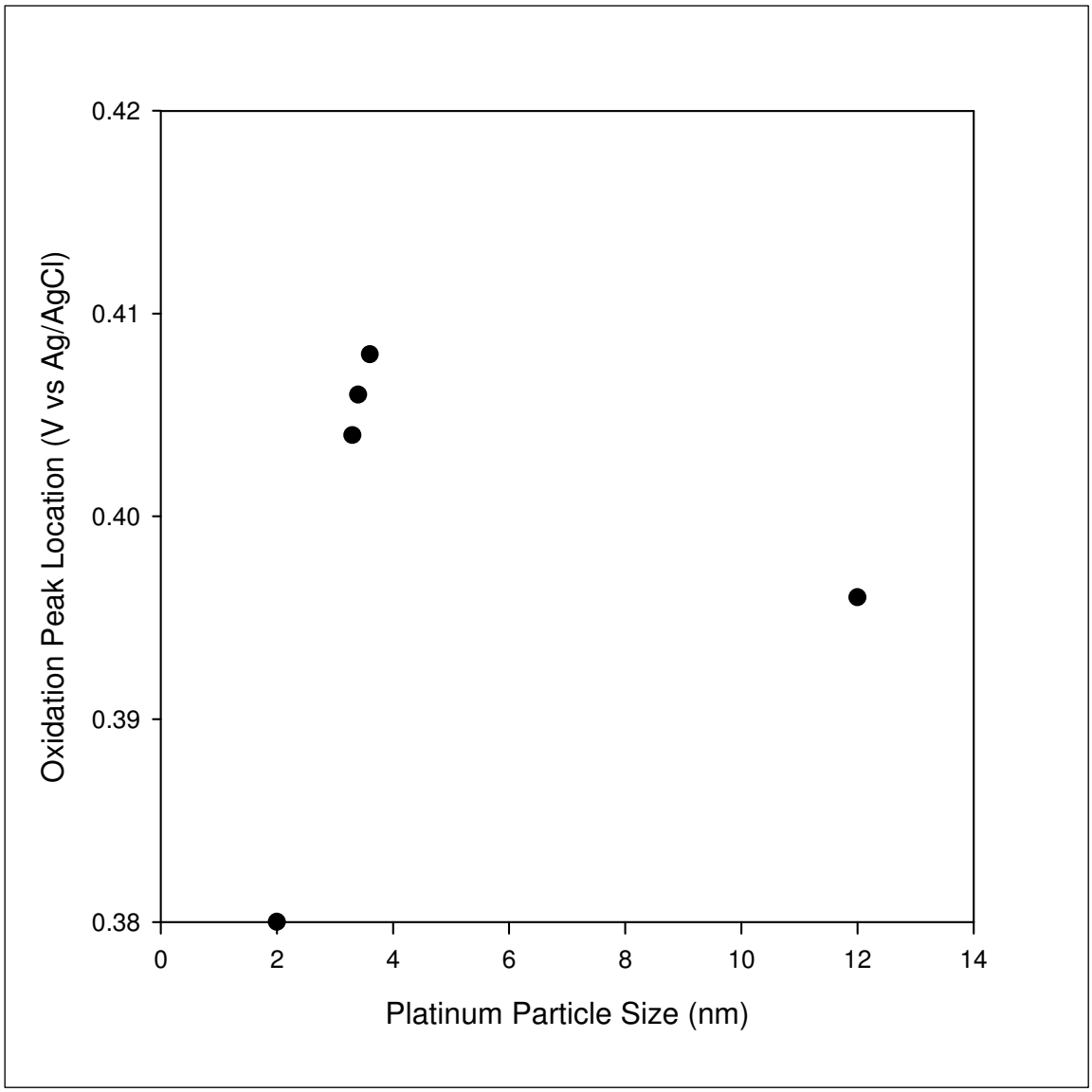

Figure 54: Estimated Oxygen Adsorption On-set Point For Catalyst Created by EG Method Under Varying pHs

From Figure 54 it appears that the oxygen adsorption strength increases with particle size up to a certain maxima at which point it begins to decrease again. Recall that the strength of this bond must attain a certain balance between adsorption and desorption in order for the ORR kinetics to be optimized. It would therefore appear that an optimum platinum particle size may be required in order to optimize this reaction.

4.2.3 Testing of Pt/CNT in a Fuel Cell Environment

PEMFC electrodes were fabricated using the synthesized Pt/CNT catalysts and electrochemical performance was evaluated as per methods described in section 3.2.5. Electrodes made of commercial Pt/C catalyst was also fabricated and evaluated for comparison.

4.2.3.1 Polarization Behavior

The steady-state polarization behavior and the power densities of the prepared electrodes are presented in Figure 55 (a) and (b), respectively. It is useful to point out that the two cells differed only on the cathode side depending on whether the electrode was made of synthesized Pt/CNT or commercial Pt/C catalysts. From Figure 55 it should be noted that the OCV for typical catalysts is expected to be in the 1.0-1.1 V range [5] for commercial PEMFC. For both cases (Pt/CNT and Pt/C), the OCV is significantly lower than the expected value but similar to each other. Since it is of interest to compare the performance of commercial Pt/C catalyst and the Pt/CNT catalyst, OCV baseline is considered to be less important than having similar OCVs. From Figure 55, it can be noted that the cell made of Pt/CNT cathode exhibits higher performance although both electrodes have similar Pt loading (0.2 mg Pt per cm^2 of electrode area). At a fixed cell voltage of 0.6 V, the current density of Pt/CNTs based MEA is nearly 740 mA/cm^2 which is higher than ~ 550 mA/cm^2 for the Pt/C based MEA. The polarization behavior also demonstrates that Pt/CNT electrode has a higher limiting current density than the Pt/C electrode indicating that the mass transport properties of the Pt/CNT electrodes are better than that of Pt/C electrodes. The exact reason for the enhanced mass transport property cannot be ascertained without having a more detailed knowledge of the catalyst layer microstructure.

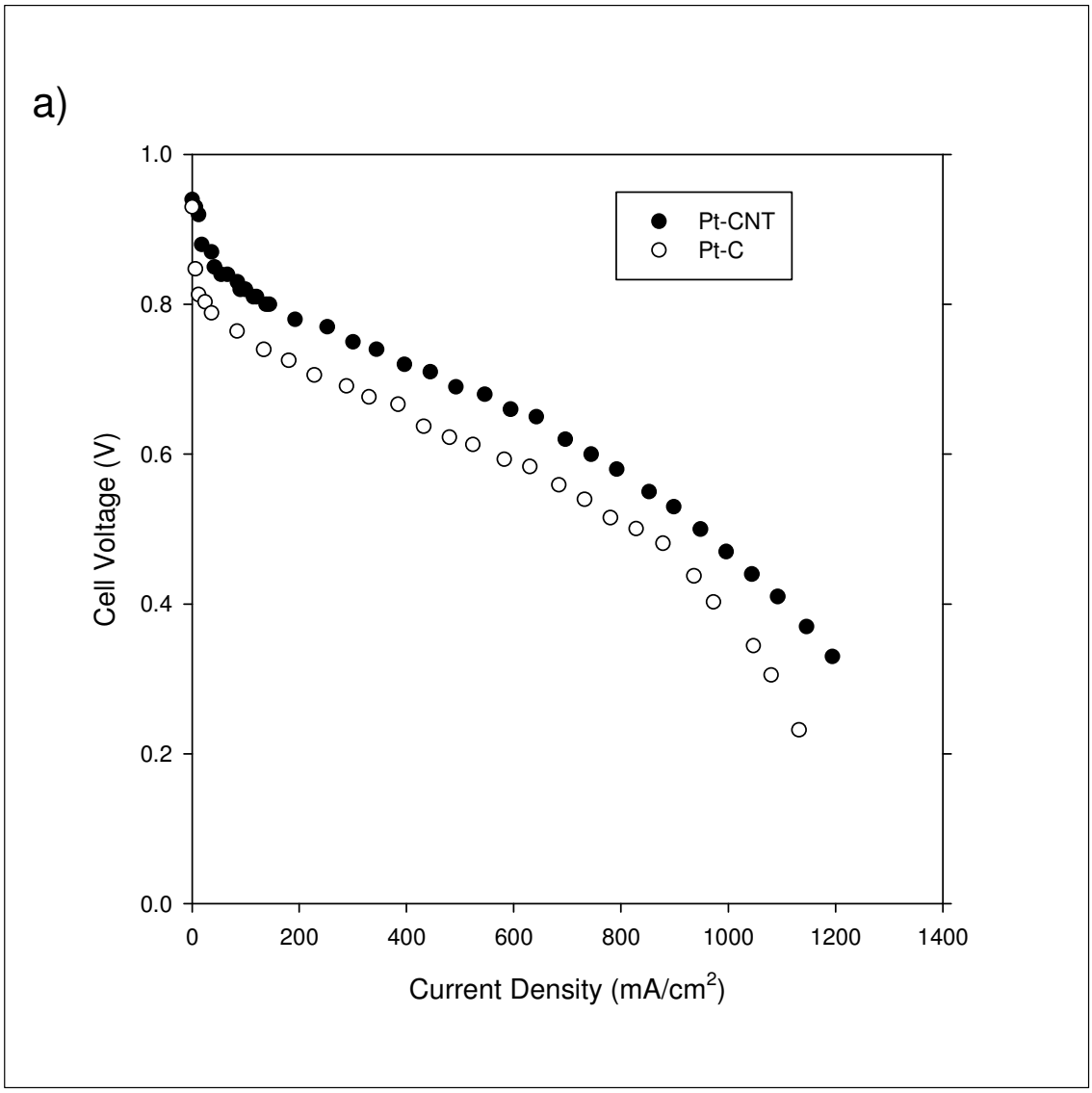
a)
1.0
0.8
0.6
0.4
0.2
0.0
Cell Voltage (V)
0
200
400
600
800
1000
1200
1400
Current Density (mA/cm2)
Pt-CNT
Pt-C

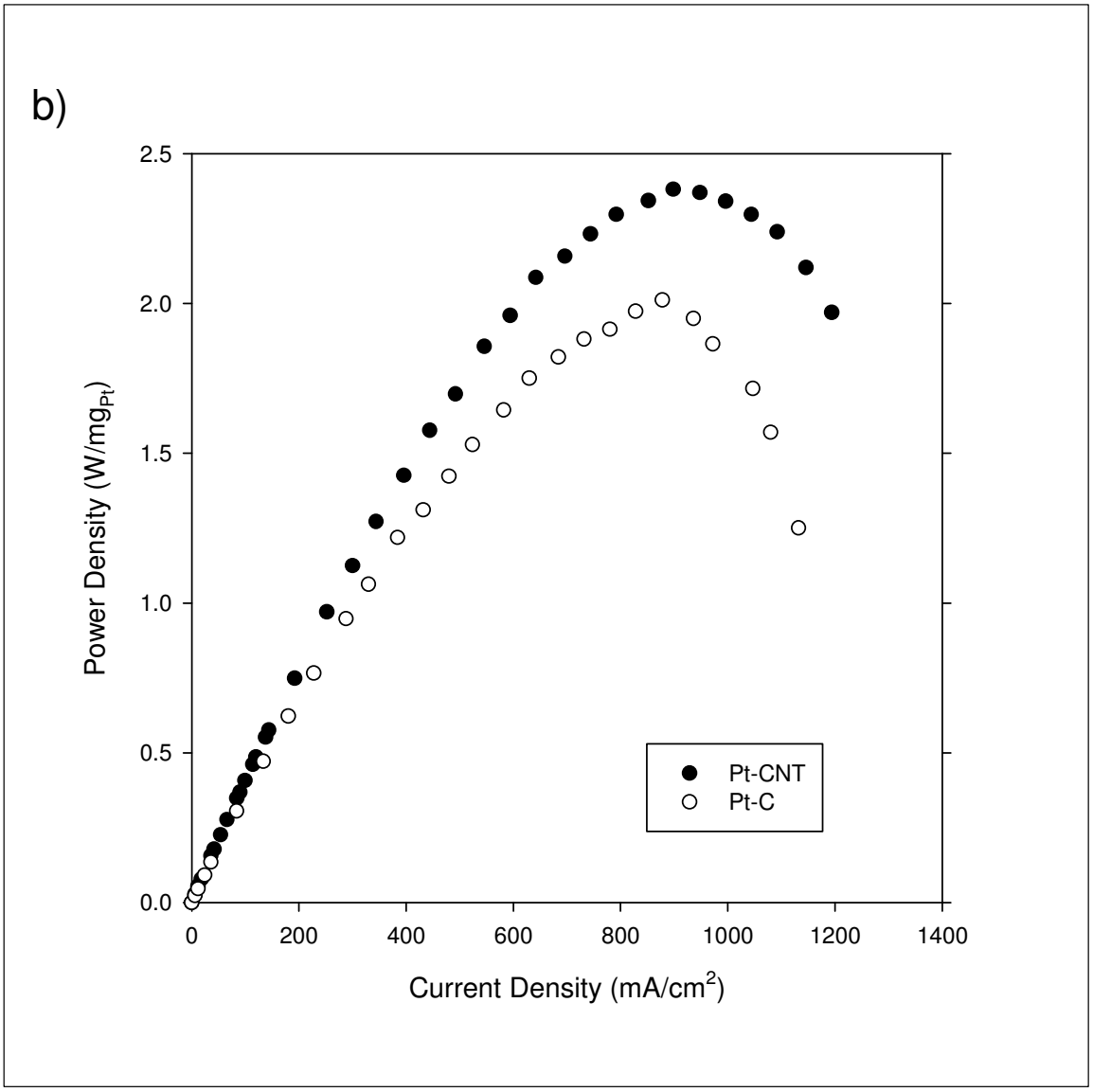

Figure 55: a)Single cell performance polarization curve b)Power Density Curve. Cell run with H_2/air at 60 °C, 35/35 kPa anode and cathode back pressure. Stoichiometric ratio H_2/air: 1.4/3.5. Pt/CNTs and Pt/C electrode (0.2 mg_{Pt}/cm^2) used as cathode and Ion Power one-sided CCM used as anode (0.3 mg_{Pt}/cm^2). Cell size 6.25 cm^2 active area.

4.2.3.2 Electrochemically Active Area

From the polarization measurements, it was noted that despite the same Pt loading for both Pt/CNT and Pt/C electrodes, Pt/CNT electrodes showed higher performance. To determine the reason for the lower performance, the two electrodes were subjected to in-situ electrochemically active area measurements. Figure 56 shows the in situ CVs of the Pt/CNTs and Pt/C catalysts at a scan rate of 50 mV/s.

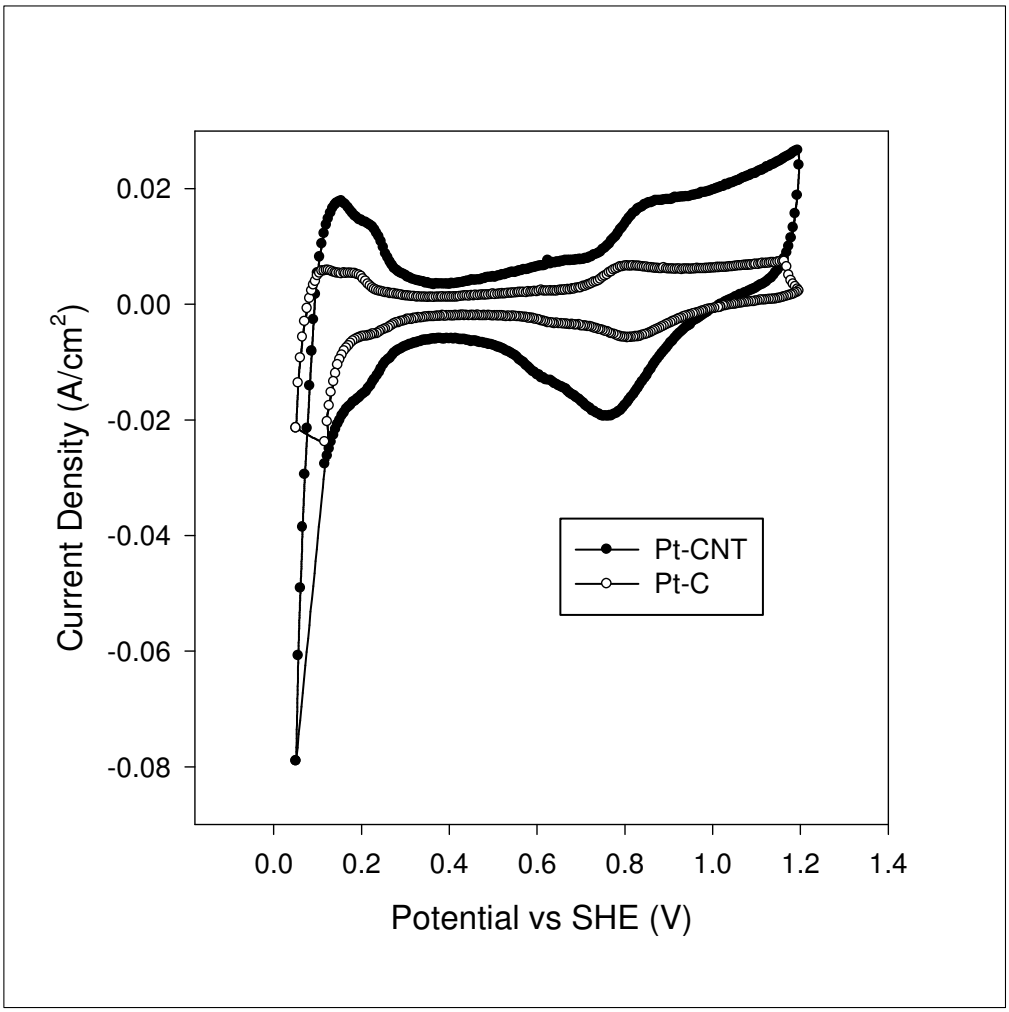

Figure 56: In-situ cyclic voltammogram of Pt/CNT and Pt/C PEMFC cathodes at 60 °C. air in the original FC cathode was replaced with N_2. Potential scan rate: 50 mV/s.

The electrochemical area of the Pt/CNTs electrode was 77 m^2/g_{Pt}, which is about 3 times higher than that of commercial Pt/C electrode (25 m^2/g_{Pt}). This higher active area suggests more platinum sites available for the ORR which leads to the improved fuel cell performance seen in the polarization curve. Clearly the mass specific power density for Pt/C is lower than that of Pt/CNT catalyst. However, the performance of the Pt/C catalyst is better than Pt/CNT catalyst on the electrochemically active area basis. Because of the complex interplay between transport and kinetic processes, which are influenced by the microstructure, it would be beneficial to compare the performance of two electrodes with similar Pt loading and electrochemically active area.

Table 9: In-Situ Fuel Cell Polarization and CV Results

Electrodes	Current density at 0.6V (mA/cm^2)	Power density at 0.6V (W/mg_{Pt})	Electrochemical area (m^2/g_{Pt})
15 wt% Pt/CNTs	744	2.23	77
20 wt% Pt/C	552	1.57	25

Chapter 5
Conclusions and Recommendations

The thesis set out to achieve two different objectives – one to explore an experimental method for the determination of oxygen permeability in thin carbon-ionomer films representing the catalyst layer, and second to synthesize and characterize Pt/CNT catalysts.

5.1 Conclusions

Oxygen Permeability Measurement Study

An electrochemical method for determination of oxygen permeability in Nafion and Nafion-carbon composite films was explored. The experimental component of the method is based on determination of the limiting current density of the inomer/ionomer-composite film-covered electrode via the standard rotating disk electrode technique. A mathematical model is required to relate the limiting current density to the oxygen permeation property of the film. It is concluded that the method can allow determination of oxygen permeability in *dense* ionomer and ionomer composite films.

However, it was found that the films prepared in this study were porous in nature which did not affect the experimental measurements but complicated the data analysis. The porous nature of the film meant that two parallel pathways for oxygen permeation (transport) were available – one through the liquid electrolyte filled pores and other through the polymeric ionomer. A modification to the mathematical model to account for the pores was proposed for data analysis. Applying the modified model to the porous Nafion film, the oxygen permeation in the Nafion phase was found to agree with the literature data for oxygen permeation in Nafion membranes.

For the Nafion-carbon composite films, it was found that the porosity of films decreases with an increase in the carbon volume fraction in the films containing up to 11.7 vol% carbon (pore-free basis). The overall oxygen permeability of the porous composite films decreased with an increasing amount of carbon in films. This trend is understood by recognizing that the carbon blocks the oxygen diffusion path in the Nafion®. However, analysis of the data to account for pores such that effective oxygen permeability in the Nafion phase of the ionomer-carbon composite was calculated, no relationship between the effective permeability and ionomer content was found. This is attributed to the errors in experimental measurements arising primarily from the porosity determination, roughness of the film and to the inhomogeneity in the films.

Pt/CNT Catalyst Synthesis

Pt/CNT catalysts were successfully synthesized using the colloidal/ethylene glycol method. Another method explored – precipitation method – did not yield reproducible results. Functionalization of CNTs was found to be critical to obtaining any significant amount of Pt deposition on CNT. The colloidal/EG method synthesized catalyst had desirable physical and electrocatalytic properties. The influence of an experimental parameter for synthesis, the pH of the solution during the deposition process, was explored. It was found that a high pH of 8.5 to 10.5 resulted in smallest Pt particle size. The Pt particles size were determined from three different techniques and found to be comparable to each other. The Pt size ranged from 2-4 nanometers. It is concluded that the pH and ethylene glycol viscosity are key parameters for controlling the Pt particle size. Whereas the effect of EG viscosity was not explored, it is thought that Pt size is stabilized by the presence of acetate ions whose content is affected by the pH.

Electrochemical characterization of the synthesized Pt/CNT catalysts was carried out in a liquid electrolyte system using rotating disk electrode setup. The electrochemical parameters – the Tafel slope and exchange current densities for oxygen reduction reaction in perchloric acid were determined. Two Tafel slope regions were observed 60 mV per decade in the low current density region and 120 mV per decade in the high current density; this is comparable to literature reported values. An interesting observation for exchange current density was made in that the exchange current density for the Pt/CNT catalysts with smallest Pt size showed largest exchange current density even after normalizing for the electrochemically active area. It is possible that there is a Pt particle size effect on the ORR kinetics as observed by the shift in the oxidative peak.

As a final assessment, the synthesized Pt/CNT catalysts were tested in a fuel cell environment. Electrodes prepared by spraying carbon-paper with Pt/CNT-Nafion ink served as the cathode. Steady state polarization curves in humidified H_2/Air system were obtained that demonstrated performance comparable to commercial electrodes in that cell potential of greater than 0.6 V at current density of 800 mA/cm^2 electrode area and a limiting current density of 1200 mA/cm^2 electrode area were observed. The electrochemical performance of electrodes prepared with Pt/C catalyst by similar method was found to be lower than that for the Pt/CNT catalysts.

In summary, the Pt/CNT catalyst synthesized has been extensively characterized for relevant physical and electrochemical properties such that it can be employed for fabrication of vertically aligned electrodes by other research members of the polymer electrolyte fuel cell research group at the Fuel Cell Research Centre.

5.2 Recommendations

Oxygen Permeability Studies

Significant difficulties were faced in trying to obtain a smooth carbon-Nafion® film of homogeneous composition on the platinum electrode. Moreover, the porosity of the film also caused complications in data analysis. New film preparation methods should be examined in order to obtain a smooth, homogeneous composition film. The preparation of a smooth film would ensure that the velocity profile used to develop the Levich model is applicable. If a smooth film is created, further studies should be carried out to determine if a trend can be found between the Nafion® content in catalyst layers and the permeability of oxygen. This type of relationship would allow for studies into the optimal amount of Nafion® for both transport and kinetic properties of the cathode catalyst layer.

It would also be beneficial to look into studies carried out on a different electrode. An electrode with a smooth surface would allow for determination of the film thickness and porosity directly on the electrode eliminating any changes in film properties that may occur when the film is deposited onto a glass slide.

It would also be interesting to examine the effect of aligned versus unaligned CNTs on the oxygen transport.

Pt/CNT Synthesis

It would be useful to run experiments at intermediate pHs within the range 8-12 to determine if 10.5 is indeed the optimal. It would also be useful to obtain durability testing in a PEMFC to

determine if the very small platinum particles obtained are stable during operation or if they agglomerate leading to worse performance with time.

Further investigation should be carried out to determine what parameters affect the precipitation deposition method and to determine if it is possible to obtain high performance catalyst.

Catalyst coated membranes (CCM) should be fabricated with Pt/CNT catalysts and its performance be compared with commercial CCMs which exhibit higher performance than electrodes made by coating catalysts on carbon paper. It would also be useful to run long durability tests on the MEAs created to determine if the CNT are in fact a more durable support than the carbon black.

Bibliography

1 J.D.Power and Associates, *"J.D.Power Asia Pacific Reports: Asia Pacific Projected to Surpass Europe as World's Regional Automotive Market by 2009"*, August 2007.

2 Toyota Motor Corp, S.Aso, M.Kizaki, Y.Nonobe, *"Development of Fuel Cell Hybrid Vehicles in Toyota"*, Fourth Power Conversion Conference, Nagoya Japan, 2007.

3 F.Plauche, *"Fuel Cells Power the Space Shuttle Orbiter"*, Electrical Review, Vol 202, May 1978.

4 R.O'Hayre, S-W.Cha, W.Colella, F.B.Prinz, *"Fuel Cell Fundamentals"*, John Wiley & Sons Inc., New Jersey 2006.

5 *"Fuel Cell Handbook"*, EG&G Technical Services, Inc, U.S. Department of Energy Office of Fossil Energy, National Energy Technology Laboratory

6 J.Larminie, A.Dicks, *"Fuel Cell Systems Explained"*, John Wiley & Sons Inc., West Sussex England, 2003.

7 J.Stumper, C.Stone, "*Recent Advances in Fuel Cell Technology at Ballard"*, Journal of Power Sources, 176, 468-476, 2008.

8 R.Ahluwalia, X.Wang, *"Fuel Cell Systems for Transportation: Status and Trends"*, Journal of Power Sources, Vol 177, 167-176, 2008.

9 Y.Zhang, H.Zhang, X.Zhu, L.Gang, C.Bi, Y.Liang, *"Fabrication and Characterization of a PTFE-Reinforced Integral Composite Membrane for Self-Humidifying PEMFC"*, Journal of Power Sources, Vol 165, 786-792, 2007.

10 B.Smitha, S.Sridhar, A.Khan, *"Solid Polymer Electrolyte Membranes for Fuel Cell Applications – A Review",* Journal of Membrane Science, Vol 259, 10-26, 2005.

11 W.Sun, B.Peppley, K.Karan, *"An Improved Two-Dimensional Agglomerate Cathode Model to Study The Influence of Catalyst Layer Structural Properties",* Electrochimica Acta, Vol 50, 3359-3374, 2005.

12 P.Costamagna, S.Srinivasan, *"Quantum Jumps in the PEMFC Science and Technology From the 1960s to the Year 2000",* Journal of Power Sources, Vol 102, 242-252, 2002.

13 S.Litster, G.McLean, *"PEM Fuel Cell Electrodes"*, Journal of Power Sources, Vol 130, 61-76, 2004.

14 M. Secanell, K. Karan, A. Suleman and N. Djilali, *"Optimal Design of Ultra-Low Platinum PEMFC Anode Electrodes",* Journal of the Electrochemical Society, 155, 125-134, 2008.

15 K.Broka, P.Ekdunge, *"Modelling The PEM Fuel Cell Cathode"*, Journal of Applied Electrochemistry, Vol 27, 281-289, 1997.

16 Q.Wang, D.Song, T.Navessin, S.Holdcroft, and Z.Liu, *"A Mathematical Model and Optomization of the Cathode Catalyst Layer Structure in PEM Fuel Cells"*, Electrochimica Acta, Vol 50, 725-730, 2004.

17 L.Li, Y.Xing, *"Electrochemical Durability of Carbon Nanotubes at 80 C"*, Journal of Power Sources, Vol 178, 75-79, 2007.

18 W.Vielstich, A.Lamm, H.Gasteiger, *"Handbook of Fuel Cells: Fundamentals, Technology, Application – Volumes 3&4: Fuel Cell Technology and Applications"*, John Wiley&Sons Canada Ltd., 2003.

19 B.Du, Q.Guo, R.Pollard, D.Rodriguez, C.Smith, J.Elter, *"PEM fuel cells: Status and Challenges for Commercial Stationary Power Applications"*, JOM, 45-49, 2006.

20 B.Wang, *"Recent Development of Non-Platinum Catalysts for Oxygen Reduction Reaction"*, Journal of Power Sources, Vol 152, 1-15, 2005.

21 J.Lee, B.Popov, *"Ruthenium-Based Electrocatalysts for Oxygen Reduction Reaction - A Review"*, Journal of Solid Sate Electrochemistry, Vol 11, 1355-1364, 2007.

22 J.Ma, B.Yi, H.Yu, Z.Hou, H.Zhang, *"Review on Preparation Method of Membrane Electrode Assembly (MEA) for PEMFC"*, Progress in Chemistry, Vol 16, 804-812, 2004.

23 H.Tawfik, Y.Hung, D.Mahajan, *"Metal Bipolar Plates for PEM Fuel Cell - A Review"*, Journal of Power Sources, Vol 163, 755-767, 2007.

24 X.Yuan, H.Wang, J.Zhang, D.Wilkinson,*"Bipolar Plates for PEM Fuel Cells - From Materials to Processing"*, Journal of New Materials for Electrochemical Systems, Vol 8, 257-267, 2005.

25 A.Hermann, T.Chaudhuri, P.Spanol, *"Bipolar Plates for PEM Fuel Cells: A Review"*, International Journal of Hydrogen Energy, Vol 30, 1297-1302, 2005.

26 X.Cheng, Z.Shi, N.Glass, L.Zhang, J.Zhang, D.Song, Z.Liu, H.Wang, J.Shen, *"A Review of PEM Hydrogen Fuel Cell Contamination: Impacts, Mechanisms, and Mitigation"*, Journal of Power Sources, Vol 165, 739-756, 2007.

27 N.Yousfi-Steiner, P.Mocoteguy, D.Candusso, D.Hissel, A.Hernandez, A.Aslanides, *"A Review on PEM Voltage Degradation Associated with Water Management: Impacts, Influent Factors and Characterization"*, Journal of Power Sources, Vol 183, 260-274, 2008.

28 C.Siegel, *"Review of Computational Heat and Mass Transfer Modeling in Polymer-Electrolyte-Membrane (PEM) Fuel Cells"*, Energy, Vol 33, 1331-1352, 2008.

29 N.Djilali, *"Computational Modelling of Polymer Electrolyte Membrane (PEM) Fuel Cells: Challenges and Opportunities"*, Energy, Vol 32, 269-280, 2007.

30 K.Lee, J.Zhang, H.Wang, D.Wilkinson, *"Progress in the Synthesis of Carbon Nanotube- And Nanofiber-Supported Pt Electrocatalysts for PEM Fuel Cell Catalysis",* Journal of Applied Electrochemistry, Vol 36, 507-522, 2006.

31 M.Uchida, Y.Aoyama, N.Eda, A.Ohta, *"Investigation of the microstructure in the catalyst layer and effects of both perfluorosulfonate lonomer and PTFE-loaded carbon on the catalyst layer of polymer electrolyte fuel cells"*, Journal of the Electrochemical Society, Vol 142, 4143-4149, 1995.

32 K.More, R.Borup, K.Reeves, *"Identifying Contributing Degradation Phenomena in PEM Fuel Cell Membrane Electrode Assemblies Via Electron Microscopy",* ECS Transactions, Vol 3, 717-733, 2006.

33 E.Antolini, *"Review Formation, Microstructural Characteristics and Stability of Carbon Supported Platinum Catalysts for Low Temperature Fuel Cells"*, Journal of Material Science, Vol 38, 2995-3005, 2003.

34 *Understanding Carbon Nanotubes*, Volume 677, Springer Berlin, 2006.

35 A.Fujiwara, R.Iijima, H.Suematsu, H.Kataura, Y.Maniwa, S.Suzuki, Y.Achiba, *"Local Electronic Transport Through a Junction of SWNT Bundles",* Physica B: Condensed Matter, Vol 323, 227-229, 2002.

36 P.Serp, M.Corrias, P.Kalck, *"Carbon Nanotubes and Nanofibers in Catalysis"*, Applied Catalysis A, Vol 253, 337-358, 2003.

37 W.Li, C.Liang,W.Zhou, J.Qiu, Z.Zhou, G.Sun, Q.Xin, *"Preparation and Characterization of Multiwalled Carbon Nanotube-Supported Platinum for Cathode Catalysts of Direct Methanol Fuel Cells"*, Journal of Physical Chemistry B, Vol 107, 6292-6299, 2003.

38 A.Thess, R.Lee, P.Nikolaev, H.Dai, P.Petit, J.Robert, C.Xu, Y.Lee, S.Kim, A.Rinzler, D.Colbert, G.Scuseria, D.Tomanek, J.Fischer, R.Smalley, *"Crystalline Ropes of Metallic Carbon Nanotubes"*, Science, Vol 273, 483-487, 1996.

39 J.Kim, M.Sham, *"Functionalization of Carbon Nanotube Surface via UV/O_3 Treatment"*, Nanoscience and Technology, Vol 121-123, 1407-1410, 2007.

40 C.Lau, R.Cervini, S.Clarke, M.Markovic, J.Matisons, S.Hawkins, C.Huynh, G.Simon, *"The Effect of Functionalization on Structure and Electrical Conductivity of Multi-Walled Carbon Nanotubes"*, Journal of Nanoparticle Research, Vol.10, 77-88, 2008.

41 N,Zhang, J.Xie, V.Varadan, "*Functionalization of carbon nanotubes by potassium permanganate assisted with phase transfer catalyst"*, Smart Materials and Structures, Vol.11, 962-965, 2002.

42 T.Aitchison, M.Ginic-Markovic, J.Matisons, G.Simon, P.Fredericks, "*Purification, cutting, and sidewall functionalization of multiwalled carbon nanotubes using potassium permanganate solutions"*, Journal of Physical Chemistry C, Vol.111, 2440-2446, 2007.

43 X.Li, I.M.Hsing, *"The Effect of the Pt Deposition Method and the Support on Pt Dispersion on Carbon Nanotubes",* Electrochimica Acta, 51, 5250-5258, 2006.

44 R.Yu, L.Chen, Q.Liu, J.Lin, K-L.Tan, S.Ng, H.Chan, G-Q.Xu, T. S.Hor, *"Platinum Deposition on Carbon Nanotubes via Chemical Modification"*, Chemistry of Materials, Vol 10, 718-722, 1998.

45 W.Chen, Y.Lee, Z.Liu, *"Microwave-Assited Synthesis of Carbon Supported Pt Nanoparticles for Fuel Cell Application*", Chemical Communications, Vol 21, 2588-2589, 2002.

46 N.Rajalakshmi, H.Ryu, M.M.Shaijumon, S.Ramaprabhu, *"Performance of Polymer Electrolyte Membrane Fuel Cells with Carbo Nanotubes as Oxygen Reduction Catalyst Support Material"*, Journal of Power Sources, 140, 250-257, 2005.

47 S.K.Natarajan, D.Cossement and J.Hamelin, "*Synthesis and Characterization of Carbon Nanostructures as Catalyst Supports for PEMFCs"*, Journal of the Electrochemical Society, 154, B310-B315, 2007.

48 V.Selvaraj, M.Vinoba, M.Alagar ,"*Electrocatalytic Oxidation of Ethylene Glycol on Pt and Pt–Ru Nanoparticles Modified Multi-Walled Carbon Nanotubes*", Journal of Colloid and Interface Science, Vol 322, 537-544, 2008.

49 H.Du, C.Wang, H.Hsu, S.Chang, U.Chen, S.Yen, L.Chen, H.Shih, K.Chen, *"Controlled Platinum Nanoparticles Uniformly Dispersed on Nitrogen-Doped Carbon Nanotubes for Methanol Oxidation"*, Diamond and Related Materials, Volume 17, 535-541, 2008.

50 Gasteiger H.A, Kocha S.S, Sompalli B, Wagner F.T, *"Activity Benchmarks and requirements for Pt, Pt-alloy, and non-Pt oxygen reduction catalysts for PEMFCs",* Applied Catalysis B: Environmental 56 9-35, 2005.

51 X.Li, W.X.Chen, J.Zhao, W.Xing, Z.D.Xu, *"Microwave Polyol Sunthesis of Pt/CNTs Catalysts: Effects of pH on Partice Size and Electrocatalytic Activity for Methanol Electrooxidization"*, Carbon, 43, 2168-2174, 2005.

52 S.Knupp, W.Li, O.Paschos, T.Murray, J.Snyder, P.Haldar "*The Effect of Experimental Parameters on the Synthesis of Carbon Nanotube/Nanofiber Supported Platinum by Polyol Processing Techniques*", Carbon, Vol 46, 1276-1284, 2008.

53 J. Wang, N.Markovic, R.Adzic, *"Simulation of O_2 reduction on Pt(111) in Acid Solutions: Intrinsic Kinetic Parameters and anion adsorption effects.",* Journal of Physical Chemistry B, Vol 108, 4127, 2004.

54 A.Parthasarathy, S.Srinivasan, A.J.Appleby, *"Pressure Dependence of the Oxygen Reduction Reaction at the Platinum Microelectrode/Nafion Interface: Electrode Kinetics and Mass Transport"*, Journal of Electrochemical Society, vol 139, 2856-2862, 1992.

55 P.Beattie, V.Basura, S.Holdcroft, *"Temperature and Pressure Dependence of O_2 Reduction at Pt\|Nafion 117 and Pt\|BAM 407 Interfaces",* Journal of Electroanalytical Chemistry, Vol 468, 180-192, 1999.

56 V.S.Murthi, R.C.Urian, S.Mukerjee, *"Oxygen Reduction Kinetics in Low and Medium Temperature Acid Environment: Correlation of Water Activation and Surface Properties in Supported Pt and Pt Alloy Electrocatalysts"*, Journal of Physcial Chemistry, 108, 11011-11023, 2004.

57 S.Mukerjee, S.Srinivasan, A.Appleby, "*Effect of Sputtered Film of Platinum on Low Platinum Loading Electrodes on Electrode Kinetics of Oxygen Reduction in Proton Exchange Membrane Fuel Cells"*, Electrochimica Acta, 38, 1661-1669, 1993.

58 L.Zhang, C.Ma, S.Mukerjee, *"Oxygen Reduction and Transport Characteristics at a Platinum and Alternative Proton Conducting Membrane Interface"*, Journal of Electroanalytical Chemistry, 568, 273-291, 2004.

59 K.Broka, P.Ekdunge, *"Oxygen and Hydrogen Permeation Properties and Water Uptake of Nafion® 117 Membrane and Recast Film for PEM Fuel Cell"*, Journal of Applied Electrochemistry, 27, 117-123, 1997.

60 S.Gottesfeld, I.Raistrick, S.Srinivasan, *"Oxygen Reduction Kinetics on a Platinum RDE Coated with a Recast Nafion Film"*, Journal of the Electrochemical Society, 134, 1455-1462, 1987.

61 M.Wilson, J.Valerio, S.Gottesfeld, *"Low Platinum Loading Electrodes for Polymer Electrolyte Fuel Cells Fabricated Using Thermoplatic Ionomers",* Electrochimica Acta, Vol 40, 355-363, 1995.

62 M.Watt-Smith, J.Friedrich, S.Rigby, T.Ralph, F.Walsh, *"Determination of Electrochemically Active Surface Area of Pt/C PEM Fuel Cell Electrodes Using Different Adsorbates"*, Journal of Physics D: Applied Physics, Vol 41, 174004, 2008.

63 A.Sarapuu, A.Kasikov, T.Laaksonen, K.Kontturi, K.Tammeveski, *"Electrochemical Reduction of Oxygen on Thin-Film Pt Electrodes in Acid Solutions"*, Electrochimica Acta, 53, 5873-5880, 2008.

64 L.Burke, J.Morrissey, *"A Survey of Platinum Hydrous Oxide Electrochemistry at Elecvated Temperature: Evidence for a New Component in the β-deposit"* Journal of Applied Electrochemistry, 26, 593-601, 1996.

65 A.Holloway, G.Wildgoose, R.Compton, L.Shao, M.Green, *"The Influence of Edge-Plane Defects and Oxygen-Containing Surface Groups on the Voltammetry of Acid-Treated. Annealed and "Super-Annealed" Multiwalled Carbon Nanotubes",* Journal of Solid State Electrochemistry, Vol 12, 1337-1348, 2008.

66 Y.Takasu, Y.Fujii, K.Yasuda, Y.Iwanaga, Y.Matsuda, *"Electrocatalytic Properties of Ultrafine Platinum Particles for Hydrogen Electrode Reaction in an Aqueous Solution of Sulfuric Acid"*, Electrochimica Acta, Vol 34, 3, 453-458, 1989.

67 P.Briot, A.Auroux, D.Jones, M.Primet, *"Effect of Particle Size on the Reactivity of Oxygen-Adsorbed Platinum Supported on Alumina"*, Applied Catalysis, Vol 59, 141-152, 1990.

68 C.Wang, C.Yeh, *"Effects of Particle Size on the Progressive Oxidation of Nanometer Platinum by Dioxygen",* Journal of Catalysis, Vol 178, 450-456, 1998.

69 V.B.Levich, *Physiochemical Hydrodynamics*, Prentice Hall, N.J, 1962.

70 W.G.Cochran, *The Flow Due to a Rotating Disk*, Proc.Camb.Phil.Soc, Issue 30, 1934.

Appendix A
Development of Levich Equation

A.1 Velocity Profile Within Hydrodynamic Boundary Layer of RDE

A rotating disk electrode provides a velocity profile, which can easily be developed in cylindrical co-ordinates. The fluid is dragged to the electrode surface by spinning of the disk and is ejected radially as seen above in Figure 15. The desired outcome is to describe the permeability of oxygen in the film on the electrode from the current/potential data obtained in the RDE experiments. Due to the flow pattern developed in RDEs cylindrical co-ordinates, r, y and ϕ will be used to develop the velocity profile.

Before developing the Levich model, a velocity profile in the boundary layer near the electrode must be developed. In order to describe the flow of a liquid the Navier-Stokes equations are applied. These equations are developed by observing the rates of change of a quantity through a specific location. For the rotating disk system the momentum conservation equations in cylindrical components take the form[69]:

$$\frac{v_\phi}{r}\frac{\partial v_r}{\partial \phi} + v_r\frac{\partial v_r}{\partial r} - \frac{v_\phi^2}{r} + v_y\frac{\partial v_r}{\partial y} = -\frac{1}{\rho}\frac{\partial P}{\partial r} + \nu\left(\Delta v_r - \frac{v_r}{r^2} - \frac{2}{r^2}\frac{\partial v_\phi}{\partial \phi}\right) \qquad \textbf{(A-5-1)}$$

$$\frac{v_\phi}{r}\frac{\partial v_\phi}{\partial \phi} + v_r\frac{\partial v_\phi}{\partial r} + \frac{v_r v_\phi}{r} + v_y\frac{\partial v_\phi}{\partial y} = -\frac{1}{\rho r}\frac{\partial P}{\partial \phi} + \nu\left(\Delta v_\phi + \frac{2}{r^2}\frac{\partial v_r}{\partial \phi} - \frac{v_\phi}{r^2}\right) \qquad \textbf{(A-5-2)}$$

$$\frac{v_\phi}{r}\frac{\partial v_y}{\partial \phi} + v_r\frac{\partial v_y}{\partial r} + v_y\frac{\partial v_y}{\partial y} = -\frac{1}{\rho}\frac{\partial P}{\partial y} + \nu\Delta v_y \qquad \textbf{(A-5-3)}$$

The conservation of mass expression in cylindrical co-ordinates at steady state takes the form:

$$\frac{1}{r}\frac{\partial v_\phi}{\partial \phi}+\frac{\partial v_r}{\partial r}+\frac{v_r}{r}+\frac{\partial v_y}{\partial y}=0 \qquad \textbf{(A-5-4)}$$

In order to determine exact solutions for the velocities, boundary conditions must be specified. At the disk surface, i.e. y=0, the following conditions must hold true:

$v_r=0$, $v_\phi=\omega r$ and $v_y=0$, where ω is the angular velocity of the rotating disk.

These boundary conditions imply that the fluid near the disk sticks to it during rotation, this is commonly known as the no slip condition. The boundary conditions in the bulk solution are based on the fact that the fluid is continuously supplied to the electrode perpendicularly, from the y-direction, with some fluid velocity U_o. Thus the boundary conditions at $y\rightarrow\infty$ are as follows:

$v_r=0$, $v_\phi=0$ and $v_y=-U_o$.

The equations can be simplified based on the fact that there is symmetry in the ϕ direction. Thus, any derivatives with respect to ϕ can be eliminated. Also the pressure can be considered constant in the radial direction. Thus equations A.1, A.2, A.3 and A.4 can be simplified as follows:

$$v_r\frac{\partial v_r}{\partial r}-\frac{v_\phi^2}{r}+v_y\frac{\partial v_r}{\partial y}=\nu\left(\frac{\partial^2 v_r}{\partial y^2}+\frac{\partial^2 v_r}{\partial r^2}+\frac{1}{r}\frac{\partial v_r}{\partial r}-\frac{v_r}{r^2}\right) \qquad \textbf{(A-5-5)}$$

$$v_r \frac{\partial v_\phi}{\partial r} + \frac{v_r v_\phi}{r} + v_y \frac{\partial v_\phi}{\partial y} = \nu \left(\frac{\partial^2 v_\phi}{\partial y^2} + \frac{\partial^2 v_\phi}{\partial r^2} + \frac{1}{r}\frac{\partial v_\phi}{\partial r} - \frac{v_\phi}{r^2} \right) \quad \textbf{(A-5-6)}$$

$$v_r \frac{\partial v_y}{\partial r} + v_y \frac{\partial v_y}{\partial y} = -\frac{1}{\rho}\frac{\partial P}{\partial y} + \nu \left(\frac{\partial^2 v_y}{\partial y^2} + \frac{\partial^2 v_y}{\partial r^2} + \frac{1}{r}\frac{\partial v_y}{\partial r} \right) \quad \textbf{(A-5-7)}$$

A solution to these equations with the given boundary conditions has been obtained by Cochran [70]. In order to obtain the solution a dimensionless quantity is described as follows:

$$\gamma = (\omega/\nu)^{1/2} y \quad \text{(A-5-8)}$$

The series solutions are given as follows [72]:

$$\begin{aligned} v_r &= r\omega(a\gamma - \frac{\gamma^2}{2} - \frac{1}{3}b\gamma^3 + ...) \\ v_\phi &= r\omega(1 + b\gamma + \frac{1}{3}a\gamma^3 + ...) \\ v_y &= (\omega\nu)^{1/2}(-a\gamma^2 + \frac{\gamma^3}{3} + \frac{b\gamma^4}{6} + ...) \end{aligned} \quad \textbf{(A-5-9)}$$

In this solution a=0.51023 and b=-0.6159. Near the surface of the rotating disk, at y→0, the following solutions are obtained [71]:

$$\begin{aligned} v_r &= -0.51\omega^{3/2}\nu^{-1/2}y^2 \\ v_y &= 0.51\omega^{3/2}\nu^{-1/2}ry \end{aligned} \quad \textbf{(A-5-10)}$$

The limiting velocity, U_o, can be determined by taking the limit of v_y as $y \rightarrow \infty$:

$$U_o = -0.88447(\omega\nu)^{1/2} \qquad \textbf{(A-5-11)}$$

This velocity profile is valid for distances very close to the electrode. Typically the thickness of this hydrodynamic boundary layer is 0.0036 cm [71].

A.2 Development of Levich Equation for Bare Electrode

Now that we have a velocity profile for the RDE we are able to determine the diffusion coefficient by writing the convective-diffusion equation, i.e. the general transport equation, for the component of interest. This equation expresses the driving force for the diffusion of a species to the electrode, which is a concentration gradient.

$$v_r\left(\frac{\partial C_o}{\partial r}\right) + v_\phi\left(\frac{\partial C_o}{\partial \phi}\right) + v_y\left(\frac{\partial C_o}{\partial y}\right) = D_o\left[\frac{\partial^2 C_o}{\partial y^2} + \frac{\partial^2 C_o}{\partial r^2} + \frac{1}{r}\frac{\partial C_o}{\partial r} + \frac{1}{r^2}\left(\frac{\partial^2 C_o}{\partial \phi^2}\right)\right] \qquad \textbf{(A-5-12)}$$

The equation under steady state limiting current conditions can be simplified. For the limiting current condition at y=0, C_o=0 which is equivalent to saying that the reaction occurs so quickly that no oxygen is left at the surface of the electrode. Also, the limit as $y \rightarrow \infty$ of C_o is C_o^*, this is equivalent to saying the bulk concentration is C_o^*. Due to symmetry C_o does not depend on ϕ. Also v_y does not depend on r, as seen in equation A-3 and very close to the electrode, at y=0, $(\partial C_o/\partial r)$=0. Thus equation A-12 can be simplified to obtain:

$$v_y\left(\frac{\partial C_o}{\partial y}\right) = D_o \frac{\partial^2 C_o}{\partial y^2} \qquad \textbf{(A-5-13)}$$

In order to solve this equation, the expression for v_y from equation A.10 is substituted in and the constant $B=D_o\omega^{-3/2}\nu^{1/2}/0.51$ is introduced to obtain the following:

$$\frac{\partial^2 C_o}{\partial y^2} = \frac{-y^2}{B}\left(\frac{\partial C_o}{\partial y}\right) \qquad \textbf{(A-5-14)}$$

Also to solve more easily let $X=\partial C_o/\partial y$ so that $\partial X/\partial y = \partial C_o^2/\partial y^2$. Using the boundary conditions at y=0, $X=X_0=(\partial C_o/\partial y)_{y=0}$ the equation becomes:

$$\frac{\partial X}{\partial y} = \left(\frac{-y^2}{B}\right)X \qquad \textbf{(A-5-15)}$$

Which becomes:

$$\int_{X_o}^{X}\left(\frac{dX}{X}\right) = \left(\frac{-1}{B}\right)\int_0^y y^2 dy \qquad \textbf{(A-5-16)}$$

By integration:

$$\frac{X}{X_0} = \exp\left(\frac{y^3}{3B}\right) \qquad \textbf{(A-5-17)}$$

Replacing X with $\partial C_o/\partial y$, B with $D_o\omega^{-3/2}\nu^{1/2}/0.51$ and by using the limits for the concentration profile, and the boundary condition C_o at y=0 is 0, the solution of the integral becomes:

$$C_o^* = \left(\frac{\partial C_o}{\partial y}\right)_{y=0} 0.8934\left(\frac{3D_o\omega^{-3/2}\nu^{1/2}}{0.51}\right)^{1/3} \quad \textbf{(A-5-18)}$$

The goal is to determine the relationship between the limiting current and the diffusion coefficient, D_o. The current is the flux at the electrode surface, that is:

$$i = nFAD_o\left(\frac{\partial C_o}{\partial y}\right)_{y=0} \quad \textbf{(A-5-19)}$$

Equation A.18 can be substituted into equation A.19 and at limiting current conditions, $i=i_{lc}$ we obtain the Levich equation:

$$i_{lc} = 0.62nFAD_o^{2/3}\omega^{1/2}\nu^{-1/6}C_o^* \quad \textbf{(A-5-20)}$$

It can be seen that the limiting current is dependent on the rotational speed such that a plot of $1/i_{lc}$ vs. $\omega^{1/2}$ will have a slope of $0.62nFAD_o^{2/3}\nu^{-1/6}C_o^*$. As a result the diffusion coefficient through the bulk solution to the electrode can be obtained by running the electrode at varying rotational speeds, creating the plot and solving the Levich equation using the slope.